Přírodovědecká fakulta
Univerzita Palackého v Olomouci

Katedra experimentální fyziky

Diplomová práce

Syntéza a fyzikálně-chemická charakterizace hybridních nanomateriálů na bázi grafenu a oxidů železa pro konstrukci zařízení uchovávajících elektrickou energii.

Autor	Bc. Jan Wyzula
Vedoucí práce	doc. Mgr. Jiří Tuček, Ph.D.
Konzultant	Juri Ugolotti, Ph.D.
Studijní obor	Nanotechnologie
Forma studia	Prezenční
Rok	2018

Bibliografická identifikace

Jméno a příjmení autora	Bc. Jan Wyzula
Název práce	Syntéza a fyzikálně-chemická charakterizace hybridních nanomateriálů na bázi grafenu a oxidů železa pro konstrukci zařízení uchovávajících elektrickou energii.
Typ práce	diplomová
Pracoviště	Katedra experimentální fyziky
Vedoucí práce	doc. Mgr. Jiří Tuček, Ph.D.
Konzultant	Juri Ugolotti, Ph.D.
Rok obhajoby práce	2018
Počet stran	81
Počet příloh	3
Jazyk	anglický
Abstrakt	Baterie založené na proudu lithiových iontů jsou momentálně jeden z nejvíce používaných zdrojů pro dnešní elektroniku. Hybridní materiály připravené kombinací vysoce vodivého grafenu a rozličných fází oxidů železa jako hematitu, maghemitu a magnetitu by mohly být dalším technologickým průlomem na poli zařízení uchovávajících elektrickou energii. Diplomová práce je zaměřena na přípravu a fyzikálně chemickou charakterizaci těchto hybridních materiálů.
Klíčová slova	grafen, grafen oxid, oxidy železa, lithium iontové baterie, katodový materiál

Bibliographical identification

Author's first name and surname	Bc. Jan Wyzula
Title	Synthesis and physicochemical characterization of hybrid nanomaterials based on graphene and iron oxides for construction of devices for energy storage.
Type of thesis	master
Department	Department of Experimental Physics
Supervisor	doc. Mgr. Jiří Tuček, Ph.D.
Consultant	Juri Ugolotti, Ph.D.
Year of presentation	2018
Number of pages	81
Number of appendices	3
Language	english
Abstract	Batteries based on the flow of the lithium ion current are the most used electrical power sources for today electronics. Hybrid materials prepared by the combination of high conductive graphene and various iron oxide phases, such as hematite, maghemite, and magnetite could be the next technological breakthrough in the field of energy storing devices. The Master thesis focusses on the preparation and characterization on the physical and the chemical properties of these hybrid systems.
Keywords	graphene, graphene oxide, iron oxide, Li-ion battery, cathode material

Prohlášení

Prohlašuji, že jsem předloženou diplomovou práci vypracoval samostatně pod vedením doc. Mgr. Jiřího Tučka, Ph.D. a Juriho Ugolottiho, Ph.D. a že jsem použil zdrojů, které cituji a uvádím v seznamu použitých zdrojů.

I declare that I have carried out the submitted Master thesis independently under the supervision of doc. Mgr. Jiří Tuček, Ph.D. and Juri Ugolotti, Ph.D. and I have used the literature included in reference section.

V Olomouci dne .....

.....
podpis

Chtěl bych poděkovat především dr. Jurimu Ugolottimu a doc. Jiřímu Tučkovi za odborné konzultace a vedení mé diplomové práce. Dále bych chtěl poděkovat vědeckým pracovníkům RCPTM dr. Ondřeji Malinovi, Mgr. Martinu Petrovi, dr. Arianě Opletalové, Mgr. Zuzaně Chaloupkové, Mgr. Josefu Kašlíkovi a Mgr. Ivovi Medříkovi za odborné konzultace a pomoc při charakterizaci a výrobě vzorků. Speciální poděkování patří Heleně Sedláčkové za konzultace o psaní v anglickém jazyce pro vědecké účely. Chtěl bych také poděkovat své rodině a přítelkyni za podporu při studiu a psaní této práce.

I would like to thank especially to dr. Juri Ugolotti and doc. Jiří Tuček for consultations and supervising of my Master thesis. I would like to also thank to researchers of RCPTM dr. Ondřej Malina, Mgr. Martin Petr, dr. Ariana Opletalova, Mgr. Zuzana Chaloupkova, Mgr. Josef Kašlík, and Mgr. Ivo Medřík for consultation and help during sample preparation and characterization. Special thanks belong to Helena Sedlačková for consultations about academic writing. My deepest gratitude belongs to my family and girlfriend who have been my support in studying and writing this work.

Contents

Introduction **8**

1. Theoretical Part **9**
1.1. Graphene . . . 9
1.1.1. Properties and characteristics . . . 9
1.1.2. Physical phenomena in graphene . . . 9
1.1.3. Preparation of graphene . . . 10
1.2. Graphene oxide . . . 11
1.2.1. Structure and properties of GO . . . 11
1.2.2. Preparation of GO . . . 12
1.2.3. Staudenmaier method . . . 12
1.2.4. Hofmann method . . . 12
1.2.5. Hummers method . . . 12
1.2.6. Tour method . . . 13
1.3. Reduced graphene oxide . . . 13
1.4. Other carbon derivatives . . . 14
1.4.1. 0D Carbon allotropes – Fullerenes and quantum dots . . . 14
1.4.2. 1D Carbon allotropes – Carbon nanotubes . . . 15
1.4.3. 3D Carbon allotropes – Graphite and diamond . . . 15
1.5. Iron oxides . . . 16
1.5.1. Magnetic properties of iron oxides . . . 16
1.5.2. Fe_3O_4 – Magnetite . . . 17
1.5.3. α-Fe_2O_3 – Hematite . . . 18
1.5.4. β-Fe_2O_3 . . . 18
1.5.5. γ-Fe_2O_3 – Maghemite . . . 18
1.5.6. ϵ-Fe_2O_3 . . . 19
1.5.7. Methods for the preparation of iron oxide nanoparticles . . . 20
1.6. GO-iron oxide hybrid materials for energy storage devices . . . 20
1.6.1. Li-ion batteries . . . 20
1.6.2. Lithium intercalation processes . . . 21
1.6.3. Metal oxides and GO hybrid compounds . . . 22
1.6.4. Fabrication of iron oxide and GO hybrid system . . . 22

2. Techniques for samples characterization **24**
2.1. Raman spectroscopy . . . 24
2.2. FT-IR – Fourier transform infrared spectroscopy . . . 25
2.3. XPS – X-ray photo-electron spectroscopy . . . 27
2.4. XRD – X-ray powder diffraction . . . 27
2.5. TEM – Transmission electron microscopy . . . 28
2.6. STA-MS – Simultaneous Thermal Analysis and Mass Spectroscopy . . . 29
2.7. Mössbauer spectroscopy . . . 30

3. Synthesis and sample characterization **31**
3.1. Graphene oxide prepared by the modified Hummers Method . . . 32
3.2. Graphene oxide prepared by the Tour Method . . . 35
3.3. Single-step hybrid preparation . . . 38
3.4. Multi-step hybrid preparation . . . 39
3.4.1. Iron(II) and iron(III) salts decomposition . . . 39
3.4.2. Hydrothermal method . . . 45
3.4.3. Magnetite and sulphonated graphene oxide hybrid system . . . 57

4. Conclusion **65**

References **66**

List of Abbreviations **73**

Physical Constants **74**

List of Symbols 75

Appendix A – EDS 76

Appendix B – XRD Rietveld analysis 79

Appendix C – Unprocessed FT-IR spectra of GO-iron oxide compounds prepared by hydrothermal method 81

Introduction

In the age of portable electronic devices and electric cars, it is essential to have a reliable power supply, which will offer the highest ratio between the amount of stored energy and battery size. The batteries based on Li-ion current are currently one the most used power sources for electronic devices. Several technological companies and science centres across the globe focus their research on the performance improvement of these batteries. The hybrid nanomaterials based on graphene oxide (GO) and iron oxides could be the next step to increase the energy density when used as a cathode material for batteries.

This work focuses on hybrid systems of GO or reduced GO (rGO) and iron oxides such as hematite (α-Fe_2O_3), maghemite (γ-Fe_2O_3) and magnetite (Fe_3O_4). The GO was prepared by modified Hummers method and Tour method. The GO-iron oxide hybrid composites were synthesised by one-step method involving thermal decomposition of ferric acetylacetonate, and multi-step methods including hydrothermal method with subsequent thermal reduction under nitrogen atmosphere, iron(II) and iron(III) salts decomposition in the presence of GO, and mixing the magnetite nanoparticles pre-synthesized by solvothermal method with sulphonated GO.

The theoretical aspects and the most common preparation methods of the materials involved in this work, such as graphene, GO, and different morphologies of iron oxide are introduced in the beginning of the theoretical part. The last part of the theoretical part is dedicated to the principles of Li-ion batteries and the preparation of the GO-iron oxide hybrid compounds.

Techniques used for the samples characterization are discussed in the second chapter. Most of the materials prepared were fully characterised by transmission electron microscopy with energy dispersive X-ray spectroscopy, Fourier transformed infrared spectroscopy, Raman spectroscopy, X-ray photoelectron spectroscopy, powder X-ray diffraction, simultaneous thermal analysis, mass spectroscopy, and room temperature ^{57}Fe zero-field Mössbauer spectroscopy. Descriptions of our procedures and the results are presented in the third chapter.

1. Theoretical Part

1.1. Graphene

1.1.1. Properties and characteristics

Graphene is currently one of the most promising material. With thickness of only one atom, graphene is one of the strongest, stiffest and toughest materials also possessing superior thermal and electric conductivity. Graphene carbon atoms are arranged in a hexagonal lattice with sp^2 hybridization. The combination of one s orbital and two p orbitals leads to the formation of three bonds between neighboring atoms of length 0.142 nm with the unhybridised p_z orbital perpendicular to the surface forming the π-bonds. Being delocalized over the whole sheet the π-bonds are responsible for the graphene unusual properties, which are [1][2][3][4]:

- High electron mobility (up to $2 \times 10^5\,\mathrm{cm^2\,V^{-1}\,s^{-1}}$) .
- Thermal conductivity ($5300\,\mathrm{W\,m^{-1}\,K^{-1}}$).
- Optical absorption (2.3 %).
- Young's modulus (1 TPa).
- Specific surface area ($2630\,\mathrm{m^2\,g^{-1}}$).

Graphene was firstly isolated by Geim and Novoselov in 2004 by exfoliation technique [5]. For this discovery they were awarded the Nobel Prize in Physics in 2010 [6].

1.1.2. Physical phenomena in graphene

Due to the unique structure of graphene, the behaviour of its electrons is very uncommon. In graphene we can observe the following quantum mechanics phenomenon:

- **Dirac fermions.** Graphene electrons excited at low energies have zero effective mass and are called Dirac fermions [7]. The mimic relativistic particles and their behaviour is better described with Dirac equation than with Schrödinger one [8]. Their velocity is constant and approximately 300 times lower than the speed of light ($v_f \cong 10^6\ \mathrm{m\,s^{-1}}$)[9]. The energy of Dirac fermions is independent on their velocity and is inversely proportional to their wavelength.
- **Linear dispersion relations – a zero bandgap semimetal.** The carbon atoms p_z orbitals hybridize to create π and π^* bands. These bands cross at the K and K' points of the Brillouin zone (Fig. 1A). The conductive and the valence bands touch at the point called Dirac point forming the so called "Dirac cone" (Fig. 1B). Due to that, graphene is considered being a semimetal, whose energy spectrum is gapless with linear dispersion relation [9][10].
- **Klein paradox.** This phenomenon describes an increased probability of tunnelling for relativistic particles. For a potential barrier of a height of $2m_0c^2$ (where m_0 is the invariant mass of a particle and c is the speed of light), the probability of tunnelling is equal to one [11]. This phenomenon is usually observed on a p-n junction of the material. The consequence of Klein paradox is a direct conversion of electrons to holes. Because of that, graphene always has a finite minimal conductivity.
- **Quantum Hall effect.** The conductivity of the material at a very low temperatures and in presence of a high magnetic field only occurs at discrete values, which can be very precisely defined as an integer or fraction multiple of von Klitzing constant $R_K = \frac{h}{e^2}$ (where e is elementary charge and h is Planck constant) [12]. In this case, the conductivity is independent of any material parameter. A room temperature quantum Hall effect in the presence of high magnetic field of 45 T was observed for the first time in graphene by Novoselov et al [13].

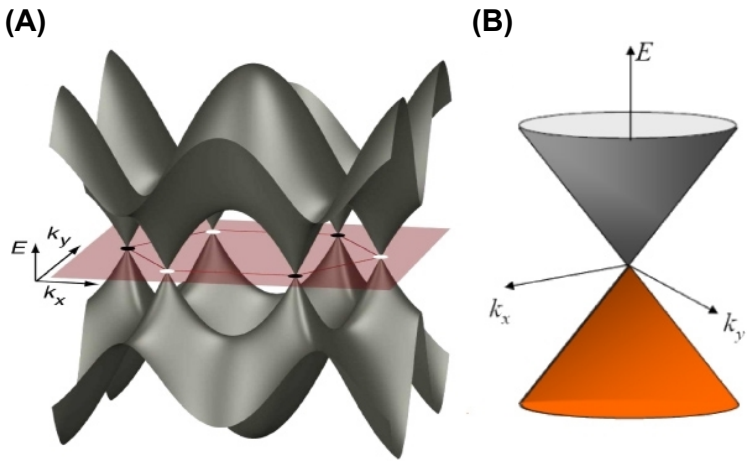

Figure 1 **(A)**: Energy spectrum of valence and conductive bands in reciprocal space with Dirac points. **(B)**: Dirac cone with linear dispersion relation (reprinted with permission from [10]).

1.1.3. Preparation of graphene

In spite of the many advantages of this material, methods of large-scale production for high quality graphene have not yet been discovered and finding efficient ways for graphene mass production is considered a major challenge. The properties of the product are very sensitive to differences in sheet size, number of layers and amount of defects. Every method offers different ratios between quality and quantity of the obtained graphene, thus affecting its cost.

Overview of the most popular method for graphene preparation:

- **Exfoliation of bulk graphite.** The first method for preparing graphene was introduced in 2004 by A.K Geim and K.S. Novoselov. According to this method, the first few layers of graphene were removed from the top of graphite by adhesive tape [9]. The flake was then transferred from the tape to a silicon substrate. This method allows to obtain samples of a very high quality with the diameter of several tens of microns. The main disadvantage is that the process is very difficult to control, as every flake has to be found using optical microscopy, which is very time consuming. Nevertheless, the samples obtained by this method are usually used for the fundamental research of graphene properties.

- **Chemical Vapour Deposition (CVD).** The first use of CVD for graphene production was reported in 2008 and 2009 on Ni and Cu substrates. This method provides a relatively large amount of high quality material for suitable prices. In general, Ni (a polycrystalline Ni or Ni(111) film) or a polycrystalline Cu film is annealed in H_2 at 1000 °C. After that, the substrate is exposed to a carbon-containing gas (usually mixture of H_2 and CH_4). In case of Cu substrates, carbon atoms of the decomposed hydrocarbon gas start to form a continuous graphene layer. Then the system is cooled down to room temperature. Graphene fabricated in this way can grow up to 1×1 cm^2 and be easily transferred onto other substrate for further research [14][15].

- **Epitaxial growth on SiC.** Epitaxial growth is a common technique, which has been used in semiconductor industry for years. In general, SiC is annealed at temperatures higher than 1400 °C in vacuum or under atmospheric pressure.The silicon atoms are evaporated leaving carbon atoms on the surface. The single layer or bilayer graphene grows on the Si face of the crystal, while few layers graphene is deposited on the C face. Due to the commercial availability of SiC, this method is very promising for obtaining a sizeable amount of graphene, which can be used for high frequency electronics [16].

- **Reduction of graphene oxide (GO).** The reduction of graphene oxide (GO) is considered the most common method for obtaining a large amount of graphene. The pathways involves oxidation of graphite to obtain GO, and subsequent reduction of GO (more in Chapter 1.2.2).

Every method provides different extent of oxidation. GO than can be reduced (chemically or thermally) to get a material with ideal consist of residual oxidation groups for desired application.

1.2. Graphene oxide

Being difficult to disperse in any solvent, pristine graphene is not suitable for chemical derivation. While the hybridization of carbon atoms in graphene is sp^2 only, GO consists mainly of sp^3 carbon bonded to various oxygen-containing functional groups [17]. Because of that, GO can be easily dispersed in water and polar solvents, which is a great advantage since allows using graphene oxide in liquid phase synthesis.

The properties of GO are primarily dependent on the synthetic method and work up and they can drastically differ from its graphene counterpart. For instance, graphene exhibits a superior conductivity, whereas the GO is an insulator. On the other hand, GO has lower tonsil strength than pristine graphene.

GO was first prepared by Brodie from Oxford University in 1859. The original purpose of seminal experiment was to measure the molar weight of graphite. Graphite and fuming nitric acid were mixed together in the presence of potassium chloride. The solution was heated up to 60 °C and maintained at this temperature for three to four days. After that, the material was washed under the same conditions and re-oxidized four times. The final product was a light yellow substance, which was dried at 100 °C. The carbon/hydrogen/oxygen ratio was found to be 61.04:1.85:37.11 [18]. Due to its dispersibility in water, it was named *Graphitic Acid*.

1.2.1. Structure and properties of GO

In spite of being known for more than 150 years, the precise chemical structure of GO is still not clear. The last few years, a large number of models describing GO have been proposed. Nowadays the most accepted model is the Lerf-Klinowski model, but other models including Hofmann, Ruess, Scholz-Boehm, Nakajima-Matsuo, and Dékány also exist [17] (Fig. 2).

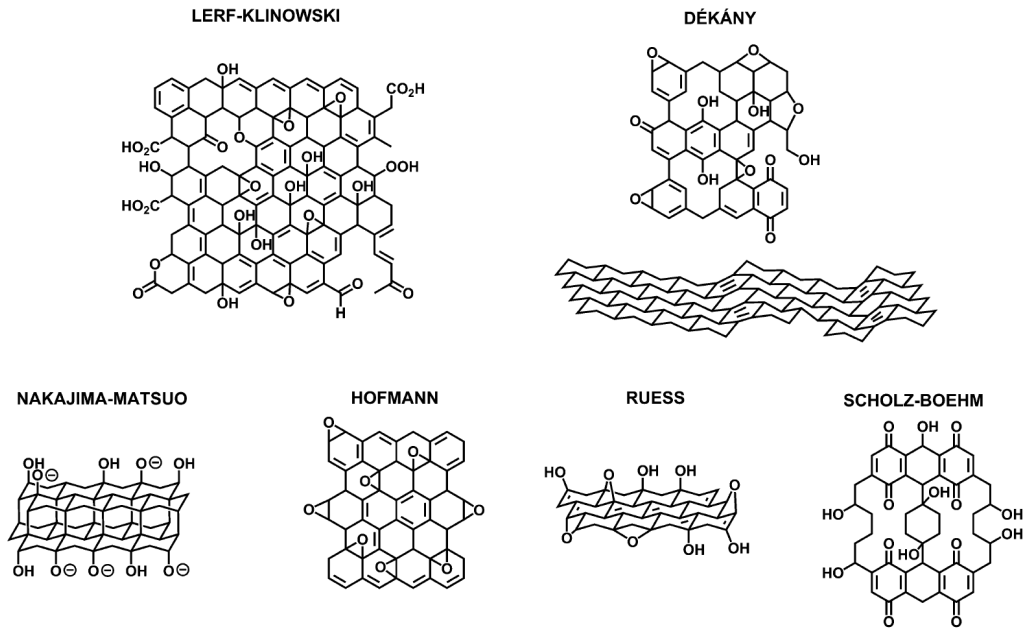

Figure 2 | Different GO models (reprinted with permission from [17]).

The older models assumed the presence of periodically repeated crystal lattice [19]. Hofmann model was composed of epoxy bridges on the basal plane with molecular formula C_2O. In 1946

Ruess changed this model by adding hydrogen groups on the basal plane. It was also pointed out that the sp^3-hybridized carbon atoms are present on the basal plane in place of sp^2 carbon. In 1969 Scholz and Boehm completely removed epoxy and ether groups.

In 1996 Lerf and Klinowski redesigned the whole model according to their observation of the elementary structure, reactivity, x-ray diffraction (XRD) and nuclear magnetic resonance (NMR) spectroscopy. Lerf-Klinowski approach distinguishes the GO into a highly functionalized sp^3 part and a less functionalized sp^2 part with the 1,3 epoxy bridges and the hydroxy groups attached on the basal plane and the carboxylic acid groups located at the edges [20].

1.2.2. Preparation of GO

Oxidation of graphite and its reduction to GO is one of the easiest and cheapest ways for its large scale production. The individual graphene layers in graphite are hold together only by weak van der Waals interactions. The very first step for GO preparation is to oxidate graphite into graphite oxide. After being oxidated, graphite starts to be hydrophilic and interlayer distance increases. These two effects are crucial for exfoliation in liquid phase, which is done usually by ultra-sonication, that turns graphite oxide into GO.

The synthetic procedures to obtain GO are separated into two groups, depending on the oxidizing agent used. The older techniques (Staudenmaier, Hofmann) are based on using chlorate agents and provide a very uniform oxidation. The newer approaches based on permanganate agents (Hummers, Tour) are easier and safer to perform in general, but the oxygen-containing groups show higher diversity.

1.2.3. Staudenmaier method

The Staudenmaier method was reported almost 40 years after Brodie experiment had been performed. In a standard procedure, 87.5 mL of sulfuric acid and 27 mL of fuming nitric acid are mixed in reaction flask. The mixture is cooled down to 0 °C in an ice bath for 30 minutes. In the next step, 5 g of graphite are added under vigorous stirring to obtain a homogeneous suspension. While the flask is still in the ice bath, 55 g of potassium chlorate are added over 30 minutes. This period served to avoid a sudden increment in temperature and the formation of explosive chlorine dioxide gas. The mixture was stirred at room temperature for 96 hours. At the end, the final product was washed several times with deionized water to get rid of the acidic residues and obtain a GO suspension with neutral pH [21].

1.2.4. Hofmann method

The Hofmann method is similar to the Staudenmaier method, the only difference being the use of non-fuming nitric acid (68%) instead of fuming one [21].

1.2.5. Hummers method

Hummers method was used for the first time in 1958 [22]. The creation of a safer, faster and more effective way of GO production was the main motivation for bringing up this technique. The product made by this process has a carbon/oxygen ratio between 2.1 and 2.9. The modified version, which operates with a double amount of $KMnO_4$, is one of the most popular ways for graphene oxide production in the research labs these days.

In the Hummers, potassium permanganate is used as oxidizing agent. 5 g of graphite and 2.5 g of sodium nitrate are mixed with 115 mL of sulphuric acid (98%). After the mixture is cooled down to 0 °C in an ice bath, 15 g of potassium permanganate are slowly added to it over 2 hour period under vigorous stirring. The suspension is heated up to 35 °C for 30 minutes. After dilution in deionized water, the system is heated up to 70 °C. The remaining unreacted potassium permanganate is reduced by addition of 30% hydrogen peroxide. At the end, the suspension is cooled

down and GO is washed with water to remove the metal ions residues [23].

1.2.6. Tour method

Another step to simplify the preparation of GO was made by Tour et al in 2010 [24]. Firstly, a 9:1 solution of concentrated sulphuric and phosphoric acid is prepared. Into that mixture the graphite flakes and potassium permanganate are added. The reaction is exothermic with raise of the temperate up to 40 °C. The mixture is heated to 50 °C and stirred for 12 h. The suspension is then cooled down to room temperature and poured onto ice. The final step is the addition of 30% hydrogen peroxide. The final product is filtered using polyester fiber and the filtrate is washed with water, 30% hydrochloric acid and two times with ethanol. The solid part is vacuum-dried for several hours at room temperature.

The GO prepared by the Tour method exhibits the largest amount of oxygen-containing groups among all techniques. The Tour approach has several advantages over Hummers method, in particular because the reaction is only slightly exothermic and there is no production of toxic gases, thus the process is much safer. Because of these properties, the Tour method is currently best candidate for use in large-scale production of GO.

1.3. Reduced graphene oxide

The properties of graphene and GO are quite different in terms of solubility, electrical and mechanical properties. GO can be modified with reduction processes into a graphene-like material (Fig. 3). The most common techniques involve thermal or chemical reduction.

One of the easiest ways to reduce the oxide groups is to anneal graphene oxide at temperatures up to 1000 °C in a reducing atmosphere (e.g. H_2). The whole process can be monitored in situ with the use of a XRD reaction chamber. With increase of the temperature, the diffraction peak of graphite shifts toward higher degrees. Comparison with other characterization techniques (e.g. X-ray photoelectron spectroscopy (XPS), Fourier transformed infrared spectroscopy (FT-IR), reveals that thermally reduced graphene oxide (rGO) is less functionalized with oxygen than GO, but has more defects and shows more amorphous character than pristine graphene [25][26].

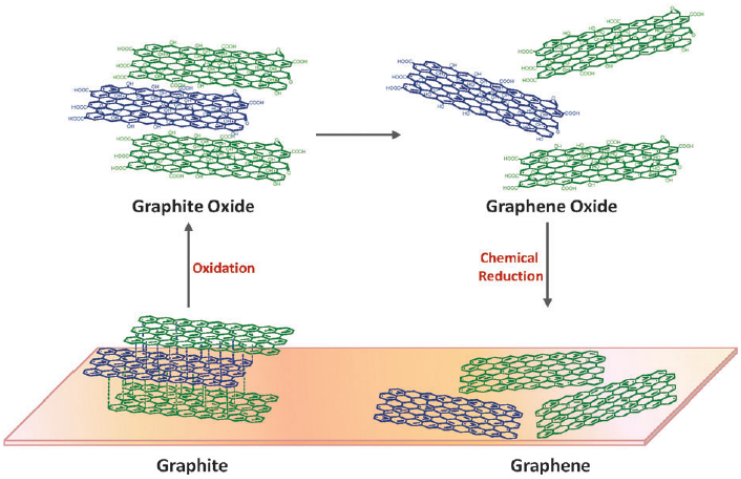

Figure 3 GO synthesis and reduction to graphene (reprinted with permission from [18]).

The chemical approach for GO reduction involves the use of various reducing agents. The reduction methods could be divided into two groups consisting of reductions with "well-supported" mechanisms and "proposed" mechanisms.

The reduction methods of "well-supported" mechanism involve reducing agents which have been used in synthetic chemistry for a long time, so their properties and impact on carbon functional groups is well-known. This group includes reducing agents such as boron hydrides (e.g. $NaBH_4$), aluminium hydride (e.g. $LiAlH_4$), hydrohalic acids (e.g. HI, HBr, HCl), and sulphur-containing reducing agents (e.g. thiourea dioxides, ethanethiol/$AlCl_3$, Lawesson's reagent). The second group with the 'proposed' mechanics includes reducing agents containing nitrogen (e.g. hydrazine), oxygen (e.g. organic solvents, such as ethanol, methanol etc.), sulphur (e.g. $NaHSO_3$), metal-acids (e.g. Al/HCl), metal-alkali (e.g. Zn/NH_3), and amino acids (e.g. glycine) [18].

Covering all aspects of each reduction technique of GO is beyond the scope of this work. The use of different reducing agents results in various degrees of reduction and thus different carbon/hydrogen/oxygen ratios.

1.4. Other carbon derivatives

In nano-scale physics, the materials could be distinguished according to their electron movement restriction in different directions, which is called the "dimensionality" of the material. The two-dimensional graphene is being considered as a basic building material for other carbon allotropes, such as 0D buckyballs (wrapped sheets), 1D nanotubes (rolled sheets), and 3D graphite (stacked sheets) [2]. In this section we will present a brief overview of other carbon allotropes with respect to their dimensionality, hybridization and relation to graphene.

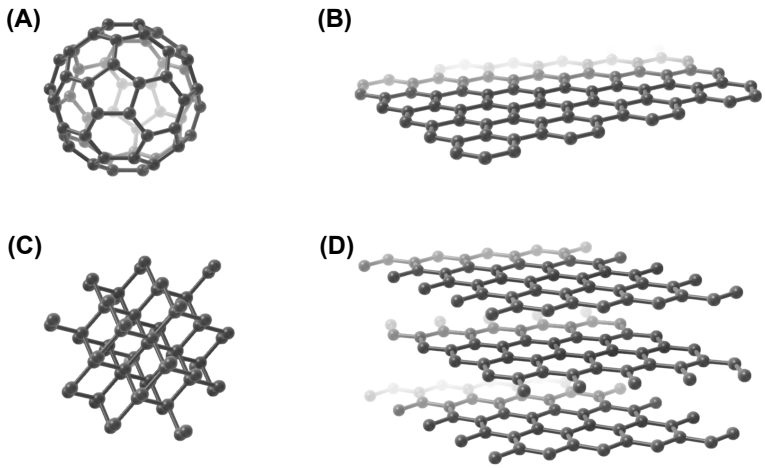

Figure 4 Carbon allotropes distinguished by their dimensionality: **(A)** 0D fullerene C_{60}, **(B)** 2D graphene, **(C)** 3D Diamond, **(D)** 3D graphite.

1.4.1. 0D Carbon allotropes – Fullerenes and quantum dots

The electron movement is restricted in each direction. This group is represented by fullerenes, carbon quantum dots, and graphene quantum dots. Fullerenes were discovered by R. E. Smalley, R. F. Curl and H. W. Kroto [27]. For this discovery they were awarded the Nobel Prize in Chemistry in 1996. Fullerenes consist of several carbon atoms arranged in pentagons and hexagons warped into a ball-like structure. Although the carbon atoms have sp^2 hybridization, a "pseudo"-sp^3 bonding component due to its non-planar arrangement of the structure is considered [28]. Nowadays, fullerenes find wide applications in non-linear optics, cosmetics, surface coating, and medicine [29].

Quantum dots are dimensionless systems with a discrete electron spectrum, which provides a large photoluminescence response. Carbon quantum dots have a diameter from 2 to 10 nm with carbon atoms mostly of sp^3 hybridization. On the other hand, graphene quantum dots consist of few layers of small size graphene with sp^2 hybridized atoms and can be obtained by GO reduction

[30]. The properties of graphene quantum dots are changing with size, shape and edges, and can find potential application in photovoltaics, bioimaging, photo-transistors, and photo-catalysis [28].

1.4.2. 1D Carbon allotropes – Carbon nanotubes

1D carbon allotropes are typically represented by carbon nanotubes (CNT). Carbon atoms are sp^2 hybridized and arranged and into hexagonal lattice. CNT could be prepared by CVD or arc discharge techniques [31] and single-walled (diameter ∼0.4–2 nm) or multi-walled systems, with length up to several µm can be obtained. CNT could be distinguished into three groups based on their edges shape, since their electrical properties are strongly dependent on that (Fig. 5):

- **Armchair** - behave as a conductor.
- **Zigzag** - single-walled CNTs are semiconductors, multi-walled ones are conductors.
- **Chiral** - behave as a semiconductor. The current flows only if an external energy is provided in the form of light or electric field.

The main advantages of the CNTs are mechanical strength (Young's modulus is higher in case of multi-walled CNTs), various electric states (semiconductor or conductor), and very good thermal conductivity. They are widely applied in various fields, such as sport equipment (bicycles, ski, boats [32]), aerospace (structure heat thermal monitor [33]), and electronics (CNT field effect transistors [34]).

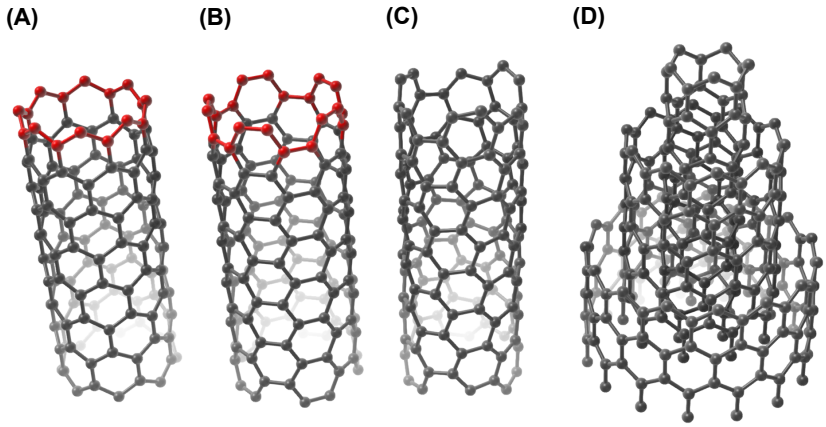

Figure 5 | Types of CNT: **(A)** Zig-zag, **(B)** Armchair, **(C)** Chiral, **(D)** Multi-walled CNT.

1.4.3. 3D Carbon allotropes – Graphite and diamond

In nature, the most common and stable form of carbon is graphite. It consists of multiple graphene layers stacked on top of each other with spacing of 0.335 nm. Due to the weak van der Waals bonds between planes, graphene could be easily separated from the bulk. There are two forms of graphite known as *alpha* (hexagonal AB Bernal stacking) and *beta* (rhombohedral ABC stacking). As already mentioned graphite is often used as a starting material for other carbon allotropes synthesis (GO, graphene).

Diamond is 3D carbon allotrope and it is one of the toughest material in nature. Hybridization of this material is sp^3 and carbon atoms crystallize into a face centered cubic lattice. Diamonds are created in the Earth upper mantle in the presence of high pressures (4.6 −6 GPa) and temperature (900 −1300 °C) or could be prepared synthetically. They are applied in areas in which high mechanical strength is required.

1.5. Iron oxides

Recently an increasing amount of interest has been dedicated to iron oxides, especially to their nanosize polymorphs. Iron oxides are well known for their magnetic properties, which are affected by the method of preparation, particle size, morphology, and aggregation [35]. They are distinguished into hydrated (e.g. goethite, akaganeite, lepidocrocite, feroxyhyte, ferrihydrite, high pressure FeOOH, schwertmannite, and fougerite) and non-hydrated forms [36] (Fig. 6). Hydrated iron oxyhydroxides forms can be found in nature as minerals and can be transformed into non-hydrated iron oxides through thermal treatment. The non-hydrated forms are classified into three categories with respect to the valence state of iron contained in their crystal lattice (only Fe^{2+} ions, only Fe^{3+} ions, and both Fe^{2+} and Fe^{3+} ions) [36]. In this section, we focus on several forms of ferric (Fe^{3+}) oxides and magnetite.

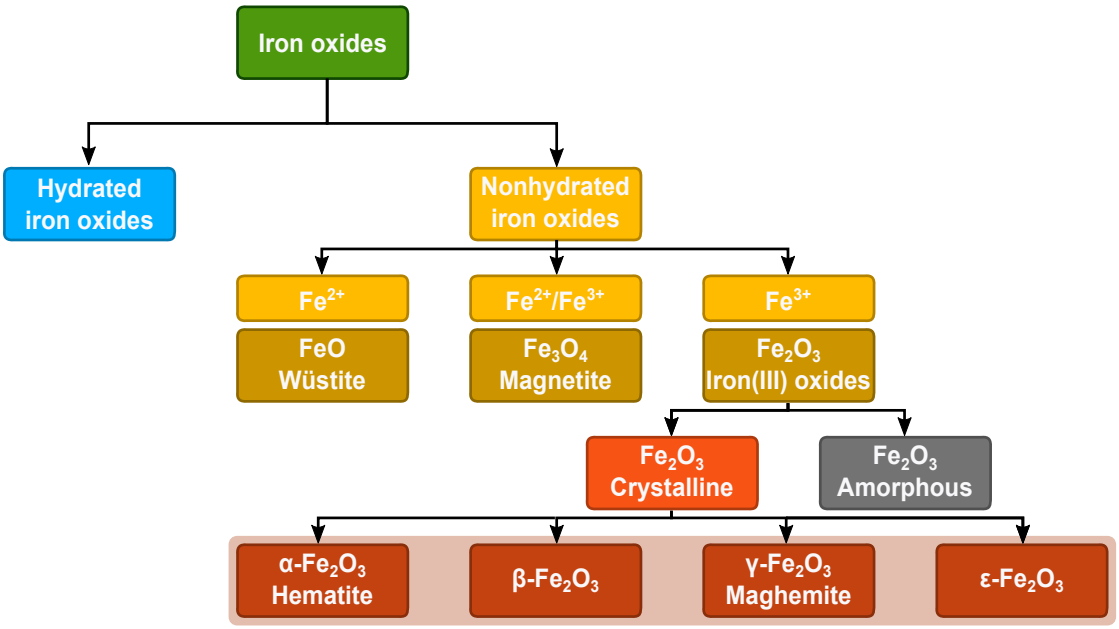

Figure 6 | Classification of iron oxides.

The preparation of iron oxide nanoparticles is relatively cheap and the product is usually non toxic. Iron oxides have various potential applications, especially in medicine (e.g. hyperthermia, contrast medium for magnetic resonance), environmental applications (e.g. water treatment), and electronics.

1.5.1. Magnetic properties of iron oxides

With the formation of crystal lattice, different magnetic states appear [37]. These states are characterized by dimensionless magnetic susceptibility, which is defined as:

$$\chi_m = \frac{M}{H}, \tag{1}$$

where M is magnetization and H is a magnetic field strength. For paramagnetic substances, the susceptibility is $0 < \chi_m << 1$, and for ferromagnetic substances is $\chi_m >> 1$.

Different types of magnetism occurring in iron oxides (Fig. 7):

- **Paramagnetism.** In paramagnetic state the individual magnetic moments are randomly oriented with respect to each other. If an external magnetic field is applied, magnetic moments are set in the same direction and the crystal shows a weak external magnetic moment.
- **Ferromagnetism.** Due to the parallel orientation of magnetic moments, the crystal exhibits large external magnetic field.
- **Antiferromagnetism.** Magnetic moments are oriented antiparallel to each other. The material shows no external magnetic field.
- **Ferrimagnetism.** Magnetic moments are oriented antiparallel to each other, but their magnitude is different. The crystal shows a weak external magnetic moment.
- **Superparamagnetism.** Superparamagnetic state occurs in nanoparticles of ferromagnetic or ferrimagnetic substances, which have smaller diameter than critical diameter of material. The magnetic ordering is maintained by an anisotropic energy, which defines the energy barrier required for a change of magnetization. Nano-scale particles have similar magnitude of anisotropic energy and thermal fluctuation, so the magnetization can be changed spontaneously without the use of external magnetic field.

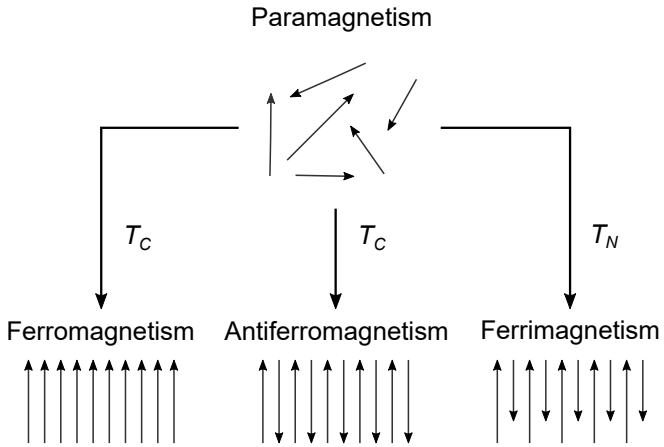

Figure 7 | Types of magnetism.

Because of thermal fluctuation of each magnetic moment, the alignment is distorted with arising temperature [37]. The magnetic ordering is completely lost at the temperatures called Néel temperature (T_N - for antiferromagnetic substances) and Curie temperature (T_C - for ferromagnetic and ferrimagnetic substances).

1.5.2. Fe_3O_4 – Magnetite

At room temperature magnetite is a ferrimagnetic material, which crystallizes into cubic symmetry with inverse spinel structure with crystal lattice constant $a = 8.397$ Å (space groups $Fd\bar{3}m$). Fe^{3+} ions are distributed between octahedral and tetrahedral positions and Fe^{2+} ions are located only at octahedral positions. When the Curie temperature is above 850 K, magnetite loses its magnetic ordering.

The properties of magnetite strongly depend on the way of synthesis, the aggregation rate, and the particle size. Particles smaller than 6 nm are superparamagnetic at room temperature. The magnetic coercivity changes with the crystal symmetry and it increases with the number of magnetization axes in the following order: sphere < cube < octahedral. The bulk magnetite has the highest conductivity (10^2–$10^3 \Omega^{-1}$ cm^{-1}) among all iron oxide polymorph and it is both an n and a p type semiconductor with the small band gap of 0.1 eV [38].

1.5.3. α-Fe_2O_3 – Hematite

Hematite crystallizes into a rhombohedrally centred hexagonal structure of the corundum type with a crystal lattice constants $a = 5.036$ Å and $c = 13.752$ Å (space group $R\bar{3}c$) [36] (Fig. 8). Two thirds of octahedral positions are occupied by Fe^{3+} ions. It is the most thermodynamic stable Fe_2O_3 polymorph. The synthesis of hematite is probably the most accessible among all Fe_2O_3 polymorphs.

The magnetic properties of hematite are changing critically across two transformation temperatures. Below Morin transition temperature ($T_M \simeq 263$ K), pure hematite exhibits antiferromagnetic ordering with spins lying along the c-axis. With increasing temperature (above ~ 263 K) the spins are reoriented and rotated by 90°. The low ferromagnetic moment is created due to the 5 degree deviation of the spins from two adjacent magnetic sublattices [39]. The magnetic order is lost for temperatures above $T_N \simeq 980$ K, when hematite becomes paramagnetic. The final properties of hematite particle are strongly dependent on particle size, number of defects, impurities, and admixtures.

Due to its low magnetic momentum, hematite is not suitable for magnetic applications. On the other hand, there is a large potential field of non-magnetic applications because of its width of bandgap (2.2 eV), high corrosion resistance, and low cost of production [38]. In the future, hematite could be used as a selective gas detection (e.q. oxygen, formaldehyde or ethanol [40]) and because of the high theoretical capacity (1007 mA h g^{-1}), this material could become very promising for application in energy storage devices for active lithium intercalation processes [41].

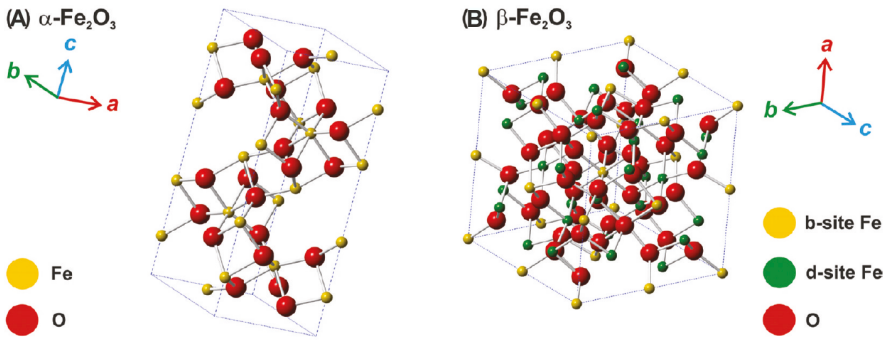

Figure 8 Crystallographic structure of **(A)** α-Fe_2O_3 – Hematite and **(B)** β-Fe_2O_3 (reprinted with permission from [42]).

1.5.4. β-Fe_2O_3

β-Fe_2O_3 is a rare Fe^{3+} oxide polymorph, which occurs only in nanometric scale and can be obtained only in laboratory conditions. β-Fe_2O_3 crystallizes into body centred cubic lattice (crystal lattice constant $a = 9.393$ Å, space group $Ia\bar{3}$) with two nonequivalent octahedral crystallographic sites [36] (Fig.8).

Below Néel temperature ($T_N = 100$–119 K), β-Fe_2O_3 exhibits antiferromagnetic ordering. Above this temperature, the behaviour is purely paramagnetic and it is the only Fe^{3+} oxide polymorph to be paramagnetic at the room temperature. The application potential is limited due to its thermodynamic instability. Hollow β-Fe_2O_3 particles transform spontaneously to α-Fe_2O_3 or γ-Fe_2O_3 [42].

1.5.5. γ-Fe_2O_3 – Maghemite

Maghemite has a cubic crystal structure with two nonequivalent crystallographic sublattices – tetrahedral (Fe_A) and octahedral (Fe_B). The structure type of the maghemite is inverse spinel with

lattice constant $a = 8.351$ Å (Fig. 9). Maghemite contains vacancies in the octahedral positions, which carry a virtual negative charge to compensate an increment of the Fe^{3+} ions positive charge in the structure [42].

Depending on the vacancies layout, there are three crystallographic configurations to be distinguished:

- Cubic structure with random vacancies.
- Cubic structure with ordered vacancies.
- Tetragonal structure with a threefold doubling along the c-axis and ordered vacancies.

Because of two non-equivalent crystallographic sites, maghemite is a material with ferrimagnetic ordering with strong magnetic response to the external magnetic field and can be permanently magnetized. Nanoparticles smaller than 10 nm exhibit a superparamagnetic behaviour. The bulk maghemite behaves as an n type semiconductor with band gap 2.03 eV [38].

Because of the chemical stability and nontoxicity of the material, there is a large variety of potential applications in medicine, such as hyperthermia, and as a contrast substance for magnetic resonance. Similarly to β-Fe_2O_3, maghemite is not thermodynamically stable and above a certain temperature (depends on several physico-chemical parameters) it transforms into α-Fe_2O_3.

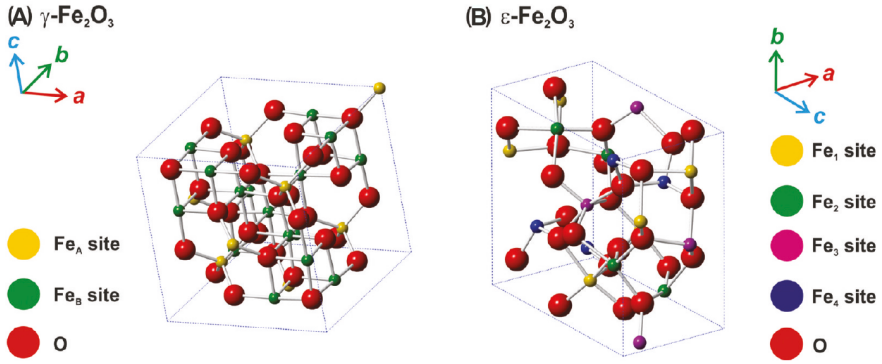

Figure 9 Crystallographic structure of **(A)** γ-Fe_2O_3 – Maghemite and **(B)** ϵ-Fe_2O_3 (reprinted with permission from [42]).

1.5.6. ϵ-Fe_2O_3

ϵ-Fe_2O_3 is a Fe_2O_3 polymorph occurring only in nanoscale form and it is very difficult to be found in nature. It crystallizes into orthorombic structure with lattice constants $a = 5.095$ Å, $b = 8.736$ Å, $c = 9.418$ Å (space group $Pna2_1$) (Fig.9) [36]. Unlike γ-Fe_2O_3, all cations positions are filled with Fe^{3+} ions without any vacancies.

By now, the magnetic properties of ϵ-Fe_2O_3 are not fully known. At room temperature ϵ-Fe_2O_3 behaves as a collinear ferrimagnet with enormous coercive field of 2 T, which could be caused by its disordered structure. The large coercive field at room temperature creates applications potential in high density storage media.

The first structural change occurs at ~110 K. At this temperature the spins are being reoriented, resulting in a different magnetic ordering, followed by significant decrease of magnetic coercivity. The material loses magnetic ordering above Curie temperature $T_C \simeq 495$ K and becomes paramagnetic [43][44].

1.5.7. Methods for the preparation of iron oxide nanoparticles

Iron oxide nanoparticles can be prepared with various techniques, which give access to different particle size, shape, phase purity, and yield. The most popular methods include:

- **Chemical Vapour Deposition (CVD).** CVD is a promising technique for deposition of a large amount of iron oxide nanoparticles. Depending on the precursor used, reaction could take place under various conditions. Iron oxide nanoparticles are obtained from the decomposition of metallo-organic precursors (e.g. Fe^{3+} acetylacetonate, iron trifluoro-acetylacetonate) at different pressures (from vacuum to atmospheric) and at temperatures between 300 °C and 800 °C [37].
- **Laser pyrolysis.** Laser pyrolysis is a fabrication process based on a resonant interaction between laser photons (in most cases CO_2 laser) and organometallic precursor in a gas form. Reaction is initialized with the heating of the floating gas mixture and maintained by laser until the critical concentration for creation of homogeneous particles is reached. The produced nanoparticles are removed with carrier gas and collected at the chamber exit [37].
- **Iron salt decomposition.** Decomposition of iron-containing salts is considered as one of the standard techniques for obtaining magnetite or maghemite. The process consists of mixing Fe^{2+} and Fe^{3+} in 1:2 molar ratio in aqueous environment. The process is started with the change of pH towards basic range, which is usually done by addition of NH_4OH. The preparation has several variables, such as reaction temperature, pH, Fe^{2+}:Fe^{3+} molar ratio, type of salt precursor, stirring rate of the mixture, and dropping rate of the basic solution. With different combinations of those parameters, iron oxide nanoparticles could be prepared with different size, shape, and phase purity [37][45][46].
- **Hydrothermal methods.** Hydrothermal methods are based on the ability of water to hydrolyze and dehydrate under various temperatures and pressures often in the presence of a surfactant [47]. The low solubility of the iron oxides leads to supersaturation of the system. The final size and shape of nanoparticles is affected by pressure, temperature, reaction time, and iron precursor. The procedure is usually performed in teflon stainless steel autoclaves at temperatures between 130–250 °C and at vapour pressure in the range from 0.3 to 4 MPa. The main advantage of this method is that the iron oxides nanoparticles could be synthesised directly on the surface of another material (e.g. graphene/GO)[37][45][46].

1.6. GO-iron oxide hybrid materials for energy storage devices

1.6.1. Li-ion batteries

It is critical to have stable and reliable energy source for today's electronics. The most used power supplies are batteries based on lithium ion current. The idea of creating Li-ion battery was originated in the Bell Labs in 1960. The first commercially available Li-ion battery was introduced by Sony in 1991 [48].

Li-ion battery consists of anode (made of carbon) and cathode (metal oxide). These days, the most commonly used cathode materials are from the family of cobalt oxides (e.g. $LiCoO_2$), which provide high energy density. Other materials used are iron phosphates (e.g. $LiFePO_4$) and manganese oxides (e.g. $LiMn_2O_4$, Li_2MnO_3), which are safer (don't explode), but their energy density is lower.

Main advantages of Li-ion batteries:

- High volume energy density (250–620 W h L^{-1}).
- Low weight and size.
- Different shapes can be obtained.
- No memory effect.
- Can withstand many charging cycles (500–1200).

Main disadvantages of Li-ion batteries:

- Danger of explosion or self-ignition if the battery is damaged or overcharged.
- Battery life negatively affected by high temperature.
- Capacity of the battery damaged if the battery is fully charged or completely discharged for a long time.

Despite many disadvantages Li-ion batteries are considered as the most suitable energy storage for portable devices these days. Batteries based on the lithium ion current are being developed by several companies around the globe and their performance is enhanced every year.

1.6.2. Lithium intercalation processes

The charging and discharging of Li-ion battery is described through intercalation (insertion) and deintercalation (extraction) of Li^+ ions into a porous matrix. With the use of the battery, Li^+ ions move from anode to cathode generating an electrical current. The charging is provided in the opposite way, when external current guides Li^+ ions and electrons back to the anode (Fig. 10). For $LiCoO_2$ cathode used in the early Li-ion batteries, the charge/discharge process could be described using the following electrochemical formulas for the anode [49]

$$C + xLi + xe^- \leftrightarrow Li_xC_6, \tag{2}$$

and cathode [49]

$$LiCoO_2 \leftrightarrow Li_{1-x}CoO_2 + xLi + xe^-. \tag{3}$$

Another important part of a rechargeable battery is the type of electrolyte, which can be in liquid or solid form. Liquid electrolytes are usually composed of a lithium salt (e.g. $LiPF_6$, $LiBF_4$, $LiClO_4$) dissolved in an organic solvent (carbonates such as ethylene carbonate, dimethyl carbonate) depending on the cathode and anode materials [50]. However, carbonate electrolytes are highly flammable at temperature $\sim 30\,°C$. Another drawback comes with the use of $LiPF_6$ as the electrolyte salt, which could produce hydrofluoric acid (HF) in the presence of water or at temperatures above 60 °C in the combination with carbonate [51].

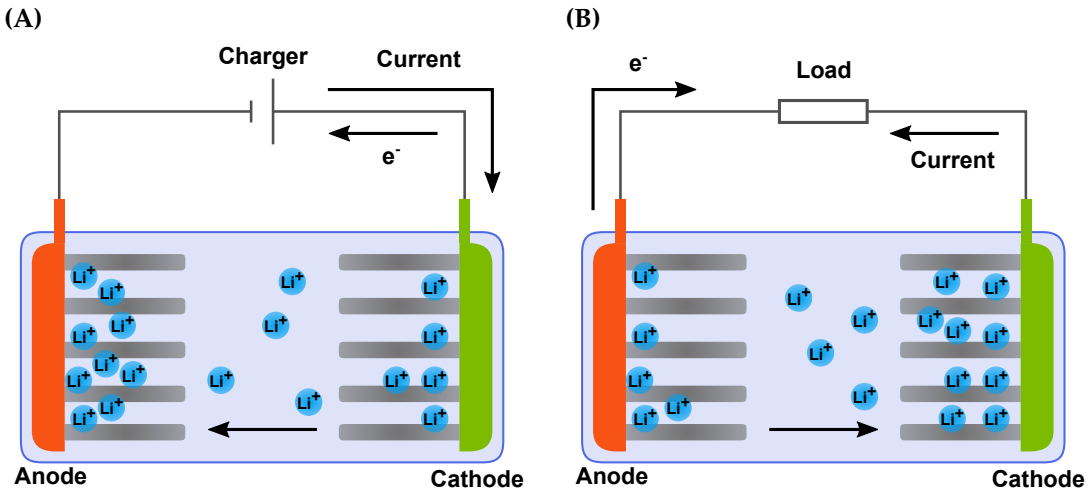

Figure 10 | **(A)** Battery charging process, **(B)** Battery discharging process

The problem of electrolyte leaking and formation of HF could be solved using solid state electrolytes for increasing the safety of Li-ion battery usage. The systems are based on ceramics (lisicon and thio-lisicon, garnet, perovskite, nasicon), glass, or combination of both materials. Li-ion is transported due to the presence of intrinsic lithium in the structure. The main disadvantage of solid state electrolytes is low ionic conductivity, which could be improved by sulphur or oxygen doping [51][52].

1.6.3. Metal oxides and GO hybrid compounds

The application of graphene based materials has been considered for increasing the performance of the Li-ion batteries. Due to its thickness, high specific surface area, and electrical and thermal conductivity, graphene could serve as a high quality support material for metal oxide nanoparticles (e.g. α-Fe_2O_3, γ-Fe_2O_3, Fe_3O_4 CoO, Co_3O_4, NiO, Cr_2O_3). The intercalation process with the use of metal oxide is described by the following formula[53]:

$$M_xO_y + 2ye^- + 2yLi^+ \leftrightarrow x[M]^0 + yLi_2O, \tag{4}$$

where M represents a transition metal (Ni, Co, Cu, Fe, Mn). Metal oxides provide several advantages including high theoretical capacity (500–1200 $mA\,h\,g^{-1}$), low cost production, and environmental sustainability[49]. On the other hand, they have several disadvantages, such as low coulumbic efficiency, large potential hysteresis, and poor cycle life. The use of hollow metal oxide nanoparticles in energy storage application is limited due to a large volume expansion of metal oxide nanoparticles during the Li^+ intercalation/deintercalation process and aggregation after the end of the cycle. Creation of graphene-metal oxide hybrids could solve some crucial problems [53][54]:

- Graphene flakes could provide a supporting matrix to prevent volume expansion of metal oxide nanoparticles.
- Metal oxide nanoparticles anchored to graphene have less chance to aggregate.
- Graphene increases the electric conductivity.
- Porosity and defects of the hybrid structure could provide more active sites for lithium storage.
- Metal oxide nanoparticles prevent graphene restacking into graphite.

1.6.4. Fabrication of iron oxide and GO hybrid system

GO is more suitable for hybrid fabrication than pristine graphene due to various oxide function groups, such as epoxy (C-O-C), hydroxy (-OH), and carboxyl (-COOH) that favours coordination to iron. Iron oxide nanoparticles could be attached to GO mainly by two anchor mechanisms [55] [56]:

- **Physical absorption** is based on non covalent van der Waals interactions between iron oxide and graphene/GO substrate. These bonds are in general quite weak and could be destroyed in unsuitable environment. The graphene/GO and iron oxide nanoparticles are usually prepared separately and mixed together. The process of physical absorption is not well controlled and the quality of the final product could be decreased by aggregation of nanoparticles on the flakes surface, which affects negatively the physical properties of the system.
- **Covalent bonding** provides stronger linking of iron oxide nanoparticles to graphene/GO. The iron could be anchored to carbon directly (Fe-C) or indirectly (Fe-OC) upon bonding. The hybridization of carbon atoms can be changed from sp^2 to sp^3, which could affect the geometry, mechanical, electrical, and magnetic properties of the hybrid.

The synthetic pathways involves a single or multiple steps solution. The single step synthesis of iron oxide nanoparticles preparation (e.g. hydrothermal, iron salt decomposition, CVD, see section 1.5.7) occurs in the presence of pre-synthesized GO. The multiple step synthesis usually consists of the following steps:

1. GO synthesis by modified Hummers method or by Tour method.
2. Modification of GO surface by organic compound/polymer or sulphuric acid [57][58] for increasing the attaching capability of the substrate.
3. Preparation of iron oxide nanoparticles.
4. Hybrid creation by mixing iron oxide and GO together (e.g. in aqueous solution with ultrasonication).

The multiple step method has several disadvantages, which include imprecise coverage of the substrate and time consuming preparation. The hybrid system could be chemically reduced or thermally treated in reducing atmosphere (e.g. H_2, CO) for partially removing of the GO oxygen-containing groups or to trigger the phase transformation of iron oxide nanoparticles [55].

2. Techniques for samples characterization

All samples were characterized by vibration spectroscopy, including Raman spectroscopy and Fourier Transform Infrared Spectroscopy (FT-IR), to determine functionalization groups and defects. Transmission electron microscopy (TEM) was performed to investigate the size distribution and the coverage of iron oxide nanoparticles on the GO. X-ray photoelectron spectroscopy (XPS) and Energy dispersive X-ray spectroscopy (EDS) were used for elemental survey and for functional groups determination. The amount of iron oxide in various materials was measured by Simultaneous thermal analysis (STA) and the phases of iron oxides were identified by X-ray diffraction (XRD) and by ^{57}Fe Mössbauer spectroscopy.

2.1. Raman spectroscopy

Raman spectroscopy is a non-destructive technique which is frequently used in both physics and chemistry to detect vibration or rotation states of a molecule. The polarizability of the molecule is the main condition to observe Raman effect [59]. Monochromatic light is inelastically scattered by the vibration energy states or by phonons of the material, thus causing energy shift of the collected light. Collection is distinguished between Stokes scattering (higher energy than the excitation beam) and Anti-Stokes scattering (lower energy than the excitation beam) (see Fig. 11).

Usually, the measurements are focused on the Stokes part, but the comparison with the Anti-Stokes one could be useful for the determination of the sample temperature and confirmation of the Raman effect observation. The Raman spectrum is interpreted in wavenumbers $\tilde{\nu}$ (cm^{-1}). The spectral conversion between wavelength $\lambda_{0,m}$ (nm) and $\tilde{\nu}$ (cm^{-1}) is calculated by the following formula [60][61]:

$$\Delta\tilde{\nu}(\mathrm{cm}^{-1}) = \left(\frac{1}{\lambda_0(\mathrm{nm})} - \frac{1}{\lambda_m(\mathrm{nm})}\right) \times \frac{(10^7\,\mathrm{nm})}{(\mathrm{cm})}, \tag{5}$$

where λ_0 is excitation wavelength, λ_m is Raman spectrum wavelength and $\Delta\tilde{\nu}$ is Raman shift in cm^{-1}. The intensity ratio between Stokes and anti-Stokes energy is given by:

$$\frac{I(\mathrm{Stokes})}{I(\mathrm{anti-Stokes})} = \frac{(\nu_0 - \nu_m)^4}{(\nu_0 + \nu_m)^4}\exp(hc\nu_m/kT), \tag{6}$$

where λ_0 is the excitation wavelength, λ_m is the measured wavelength, h is Planck's constant, c is the speed of light, k is the Boltzmann constant and T is the absolute temperature.

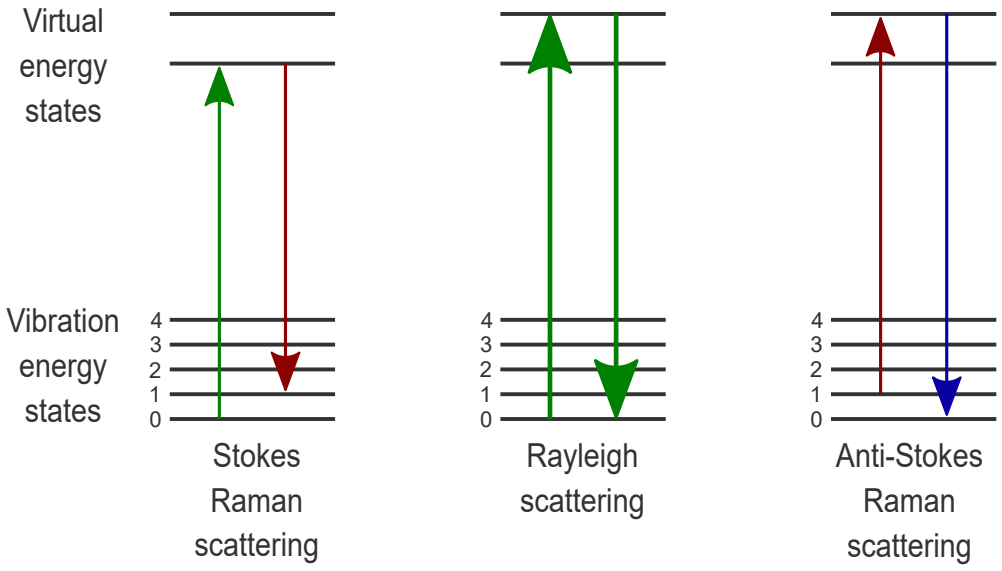

Figure 11 | Raman scattering on vibration energy states of the material.

The experimental set-up usually consists of laser, lenses or microscope objectives located before movable sample bench, filter (to remove the Rayleigh scattering of the laser), a monochromator, and a detector, which is usually charge-coupled device (CCD) chip. The Raman spectrum of carbon based materials can provide information about defects, edges, thickness, mechanical strain, level of doping, and thermal conductivity. The main band of the graphene-like materials are [62][63][64][65][66]:

- **D band**($1330\,cm^{-1}$) determines the level of functionalization and the amount of vacancies in graphene or GO. It represents the breathing modes of hexagonal atom ring and requires defects to activate, thus of that it is not visible in pristine graphene.
- **G band**($1585\,cm^{-1}$) is characteristic for graphitic material. It stands for primal vibration modes of graphite (stretching the bonds in the plane). It is a confirmation of sp^2 hybridization.
- **2D band**($2655\,cm^{-1}$) occurs in both graphene and graphite. It is the D-band over-tone and its intensity and shape are changing with the number of graphene layers.

For GO characterization it is customary to calculate the ratio between D and G bands for determining the amount of defects of the material.

Transition metals compounds could also be detected using Raman spectroscopy. Vibration modes of metals usually occurs in a low energy region of the spectrum, approximately between $200\,cm^{-1}$ to $800\,cm^{-1}$. Investigation of the hybrid materials was focused on distinguishing hematite, maghemite and magnetite in the samples (a brief overview of their vibration modes could be found in Table 1).

Iron oxide phase	**Raman shift (cm^{-1}) and Raman active phonon mode**
Hematite	229 (A_{1g}), 249 (E_g), 295 (E_g), 302 (E_g), 414 (E_g), 500(A_{1g}), 616 (E_g), 660 (LO E_u)
Maghemite	365 (T_{2g}), 511 (E_g), 700 (A_{1g})
Magnetite	310 (T_{2g}), 554 (T_{2g}), 672 (A_{1g})

Table 1 Raman active phonon modes of iron oxide phases (wavenumbers of Raman shifts taken from [67]).

It is very important to mention that the samples could be heated by the high excitation power of the laser, which would result into polymorph transformation from maghemite/magnetite to hematite [67][68][69]. The Raman signal produced by a transition metal oxide can be very hard to detect, because of its low intensity compared to the carbon bands or samples fluorescence in the low energy region.

Instrument used : DXR Raman Microscope with 633 nm diode laser.

2.2. FT-IR – Fourier transform infrared spectroscopy

Fourier transformed infrared spectroscopy (FT-IR) is a technique used for identification of bond vibration frequencies, which provide information about chemical groups present within the material. The infrared spectrum is generated by vibrations which induce changes in the dipole moment.

The measurement can be performed in absorption or transmittance mode. In general, polychromatic infrared beam (the source is in the most cases a black body radiator) after passing through a Michelson interferometer interacts with the sample (Fig. 12). The Michelson interferometer is composed of a set of mirrors and the beam splitter. One mirror is fixed and the other one is moved, which causes photons to constructively or destructively interfere. The sample spectrum is compared with the reference data from the interferometer. The final spectrum is obtained after being processed by a computer algorithm using the Fourier transformation [61][70].

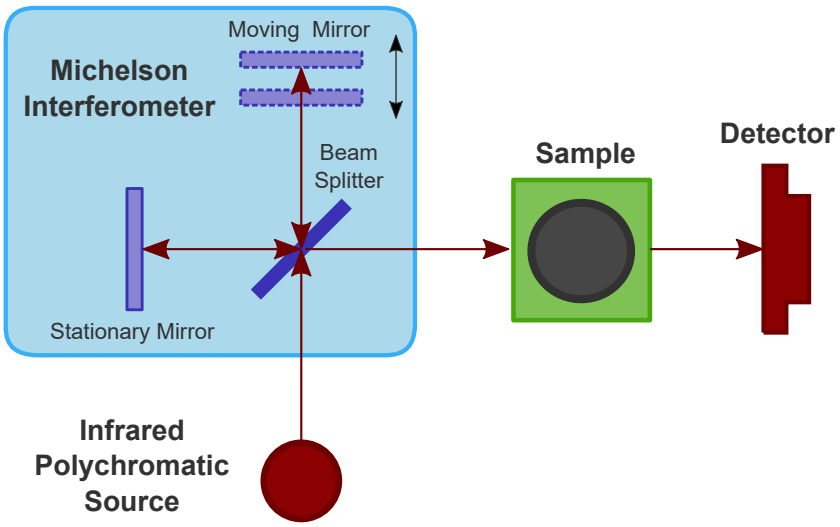

Figure 12 | Experimental setup for FT-IR measurement.

FT-IR is a very useful technique for the study of carbon materials. The absorption bands can supply information about oxide and other functional groups. The instrument used in this work, however, did no allow to detect the low energy bands of iron oxide bonds (below 600 cm^{-1}).

Main bands observed from graphitic FT-IR spectrum are [24][71][72][73]:

- **O-H stretching vibration**(3420 cm^{-1}).
- **C=O stretching vibration**(1720–1740 cm^{-1}), a signature band for carboxylic/carbonyl group.
- **C=C**(1590–1620 cm^{-1}), generated by sp^2 carbon bonds.
- **C-O vibrations**(850–1380 cm^{-1}) represents single carbon-oxygen bonds, such as C–O epoxy bending (∼850 cm^{-1}), C–O alkoxy stretching (1070 cm^{-1}), C–O epoxy stretching (1200 cm^{-1}), and C-O carboxyl group (∼1409 cm^{-1}) .

Our measurements were performed using Smart Orbit ZnSe attenuated total reflectance (ATR) attachment (Fig. 13). The sample is dissolved in ethanol and than placed on the crystal. The infrared beam interacts with sample through the crystal with higher refractive index than the measured sample, creating an evanescent wave analysed by a detector. FT-IR spectrum is obtained after evaporation of ethanol, which is confirmed by the decrease of intensity of O-H vibration.

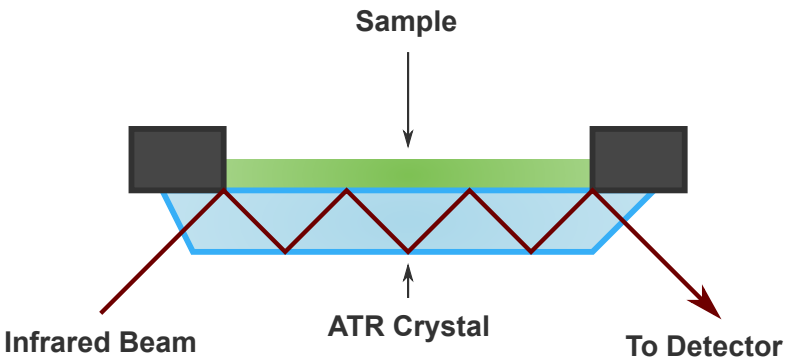

Figure 13 | Scheme of the FT-IR using ATR crystal..

Instrument used: iS5 FT-IR spectrometer (Thermo Nicolet) with Smart Orbit ZnSe attenuated total reflectance (ATR) attachment, spectral range from 4000 to 650 cm^{-1}.

2.3. XPS – X-ray photo-electron spectroscopy

X-ray photo-electron spectroscopy (XPS) is a surface sensitive technique used for determination of elemental composition and electronic states of a material. The technique is based on the photoelectric effect, where the energy of the X-ray beam is transferred to the electrons of the sample. The ejected electrons are focused with magnetic lenses to a hemispheric detector, which is used to distinguish their energy. The electrons kinetic energy refers directly to the binding energy in the sample, so it allows to identify the original orbital of the electron and the elemental composition. The final XPS spectrum consist of the number of counts on the detector for each binding energy, which is calculated by the following formula:

$$E_{binding} = E_{photon} - (E_{kinetic} + \phi), \tag{7}$$

where $E_{binding}$ is the binding energy of the electron, E_{photon} is the energy of X-ray photon, $E_{kinetic}$ is the kinetic energy measured by the instrument and ϕ is a work function, which is affected both by the material and spectrometer.

XPS is a very powerful tool for the study of GO and 2D materials in general. Our measurements were focused on the elemental survey of the sample and deconvolution of C1s (Table 2) and O1s (Table 3) peak in high resolution mode .

Binding Energy [eV]	FWHM Range [eV]	Bond	Chemical State
283.8–284.6	0.6–0.8	C-C	sp^2 carbon
284.7–286.0	0.6–1.2	C-C	sp^3 carbon
286.3–287	0.6–1.2	C-O	Epoxy/Hydroxyl
287.8–288.3	0.6–1.2	C=O	Ketone
289.0–289.5	0.6–1.2	O=C-OH	Carboxyl

Table 2 Binding energies and full width at half maximum (FWHM) of carbon C1s peak for carbon materials (values from [74][75][76]).

Binding Energy [eV]	FWHM Range [eV]	Bond	Chemical State
$\sim$ 531.3	1.2–2	C=O	Ketone
$\sim$ 533.3	2.5–3.2	C-O	Epoxy
$\sim$ 533.8	1.5–2.1	O=C-OH	Carboxyl

Table 3 Binding energies and full width at half maximum (FWHM) of oxygen O1s peak for carbon materials (values from [77][78]).

Data were analysed with MultiPak (Ulvac-PHI, Inc.) software package. The background corrections for high resolution XPS were carried out using Shirley's baseline and all peak were fitted with Gaussian-Lorentzian functions to determine the energy and area of each bond involved.

Instrument used: PHI VersaProbe II (Physical Electronics) spectrometer, X-ray – AlK_α (15 kV, 50 W).

2.4. XRD – X-ray powder diffraction

X-ray powder diffraction is a method for the determination of the structural properties of a crystalline material. This technique uses Bragg's law (Fig. 14) for diffraction of X-ray photons on the crystal lattice of the sample, which is described by the following formula:

$$2dsin(\Theta) = n\lambda, \tag{8}$$

where d is an interlayer distance, Θ is the angle of the incident X-ray radiation, n is an integer representing the order of diffraction, and λ is the wavelength of X-ray photons.

The measurements could be performed under various configuration and geometries, such as Debye-Scherrer or Bragg-Brentano (Fig. 15).

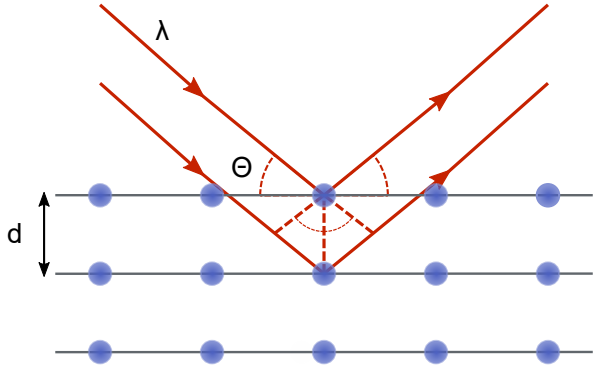

Figure 14 | Braggs law

The measurements were performed using Bragg-Brentano set up, which consists of X-ray source, divergence-limiting slit, sample holder, anti-scatter slit, monochromator crystal, and detector. XRD characterization of our samples was focused on the determination of the iron oxide nanoparticles phase and mean coherence length (MCL) of the system. The signal was analysed using the Rietveld method, which finds the best agreement between measured data and the ideal structure from the database using the least squares regression analysis.

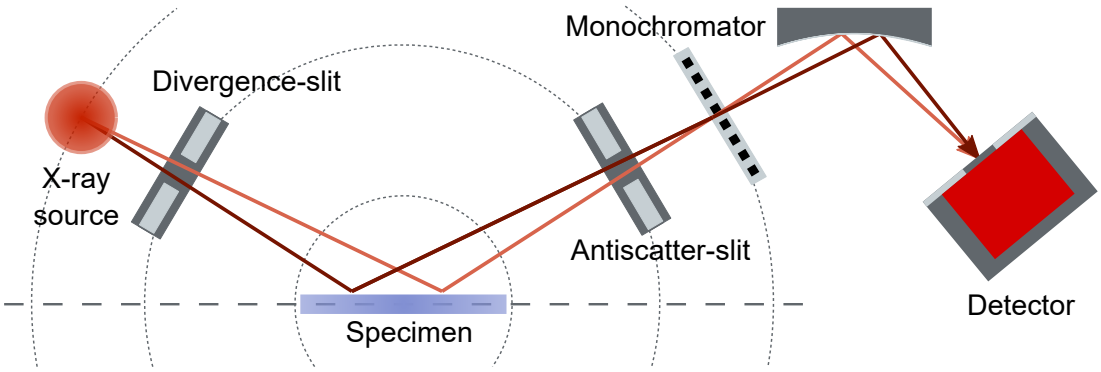

Figure 15 | XRD Bragg-Brentano geometry

Instrument used: PANalytical X'Pert Pro MPD, Θ-Θ Bragg-Brentano parafocusing geometry with Co Kα radiation (λ = 1.790 31 Å).

2.5. TEM – Transmission electron microscopy

Transmission electron microscopy (TEM) was used for the determination of the shape, size distribution, and the coverage of iron oxide nanoparticles on the GO. In a typical configuration, electrons produced by an electron gun (a tungsten filament/needle, or a lanthanum hexaboride single crystal source) are collimated to the sample by electromagnetic lenses. The passed electrons are collected on a fluorescent screen or by CCD chip.

TEM is normally suitable only for samples thinner than 100 nm or on a solution deposited on the grid (carbon coated copper grid is used in most cases). An electron microscope is usually equipped with energy dispersive X-ray spectrometer (EDS), which provides elemental analysis of the material. High energy beam of electrons interacts with the specimen electrons, which

are ejected from the inner shell leaving a hole behind. This hole is filled with the electron from higher shells, which generates emission of characteristic X-ray photons analysed by a semiconductor Si(Li) detector.

Instrument used: JEOL 2100 with 80-200 kV accelerating voltage.

2.6. STA-MS – Simultaneous Thermal Analysis and Mass Spectroscopy

Simultaneous thermal analysis (STA) is a destructive technique consisting of thermogravimetric analysis (TGA), differential scanning calorimetry (DSC) with addition of mass spectroscopy (MS) in case of STA-MS configuration. In this work, STA is mostly used for the determination of amount and phase of iron oxide nanoparticles in hybrid systems.

A change of mass with the raising temperature (up to 2000 °C) is provided by TGA. The temperature of phase transformation, sublimation, decomposition, oxidation and reduction could be obtained from the measured mass profile and residual mass depending on the type of atmosphere used for the experiment [79].

DSC measurement examines the amount of heat needed for the temperature increment of a sample compared to a reference. DSC provides information on melting temperature, crystallization temperature, oxidation and decomposition of the material, whereas TGA simultaneously shows the amount of combustible and incombustible components.

MS scans the evolved gases created during the heating process. Knowing the residual mass of the sample and the m/z ratios of the evolved gases, it is possible to derive the chemical equation responsible for the thermal degradation of a sample.

Figure 16 STA449 C Jupiter-Netzsch connected to QMS 403 Aëolos mass spectrometer (Netzsch).

All measurements were performed under the same condition in a temperature range from 40 °C to 1000 °C with the heating rate 10 K min^{-1}. The synthetic air (flow rate 70 mL min^{-1}) was used as an atmosphere in the chamber and nitrogen gas was used as a protective gas (flow rate 10 mL min^{-1}).

Instrument used: TGA/DSC were performed on STA449 C Jupiter-Netzsch, MS was measured by QMS 403 Aëolos mass spectrometer (Netzsch).

2.7. Mössbauer spectroscopy

Mössbauer spectroscopy is a technique based on the Mössbauer effect, which was first observed in 1958 by R.L. Mössbauer. For this discovery he was awarded by Nobel Price in Physics in 1961. The effect is based on resonance absorption and emission of γ-photons between two nuclei. However, nucleus emitting γ-photon is pushed back by recoil energy, which modulates the wavelength of the radiated γ-photon. The recoil could be suppressed by fixation of the atom to another crystal lattice. The emitter is usually placed on a transducer, which modulates the radiation using Doppler effect. The measurement is performed in transmission or backscatter geometry. In the transmission geometry, the final spectrum is measured as the dependence between relative velocity of the emitter and the photon counts on the detector.
Information obtained from Mössbauer spectroscopy (Fig. 17):

- **Isomer shift** represents the shift of the whole spectrum with respect to its centre of gravity. This phenomenon originating from interaction between the positively charged nucleus (volume is different in the case of excited and non-excited one) and distribution of the negatively charged s electron orbital.
- **Quadrupole splitting** is the result of interaction between nucleus quadrupole moment (originating in non-spherical distribution of charge in all nuclei with angular momentum higher than 1/2) and an electric field gradient of the valence electrons and ligands. The nucleus energy levels are split into two lines and the doublet is observed in the Mössbauer spectrum.
- **Magnetic hyperfine splitting** reflects the interaction between the magnetic dipole moment of the nucleus and a magnetic field (also knows as Zeeman effect), which leads into degeneration of the system splitting energy levels into six lines observed as the sextet in the Mössbauer spectrum. Nuclear transitions between excited states and ground states have to obey the selection rules of magnetic dipoles, which allow excitation only if the magnetic quantum number is changed by 0 or 1.

The ^{57}Fe zero-field Mössbauer spectroscopy is very powerful for samples containing iron in various oxidation states. Mössbauer spectrum of the material is used for qualification of the phase composition, determination of valence and spin states of atoms, differentiation of structural positions of iron atoms, stochiometry examination of cation substitution, determination of the magnetic state, local configuration of magnetic moments of the atoms, and mechanism and kinetics of reactions including phase transformation [80][81][82].

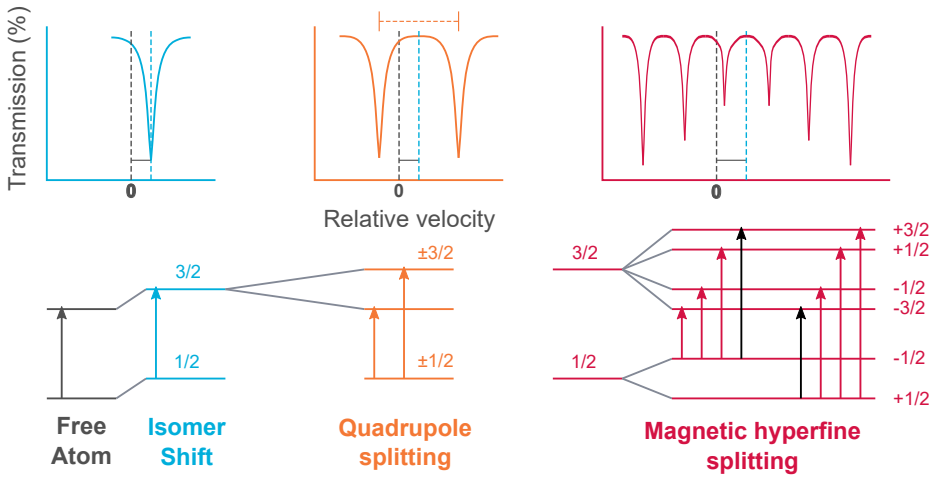

Figure 17 Information obtained from Mössbauer spectroscopy:
Isomer shift, Quadrupole splitting, Magnetic hyperfine splitting.

The ^{57}Fe zero-field Mössbauer spectra were recorded at the room temperature employing a Mössbauer spectrometer operating in a constant acceleration mode and equipped with a 50 mCi 57Co(Rh) source. The values of the center shift are referred to α-Fe at room temperature. All the acquired Mössbauer spectra were fitted using the MossWinn software [83].

3. Synthesis and sample characterization

GO was prepared by modified Hummers method and Tour method. The GO-iron oxide composites were synthesized by one-step method, that is decomposition of ferric acetylacetone in 1-methyl-2-pyrrolidone in the presence of GO, hydrothermal method with subsequent thermal reduction under nitrogen atmosphere, decomposition of iron(II) and iron(III) salt in the presence of GO, and multi-step method involving sulphonation of GO and mixing with pre-synthesized magnetite nanoparticles (overview in Fig. 18). GOs were characterized by TEM, FT-IR, Raman spectroscopy, STA-MS, and XPS with focus on structural properties, amount of defects, elemental composition, and amount of oxygen-containing groups. The structural-morphological properties of GO-iron oxide composites were investigated by TEM, EDS, FT-IR, Raman spectroscopy, XPS, STA-MS, XRD, and room temperature ^{57}Fe zero-field Mössbauer spectroscopy.

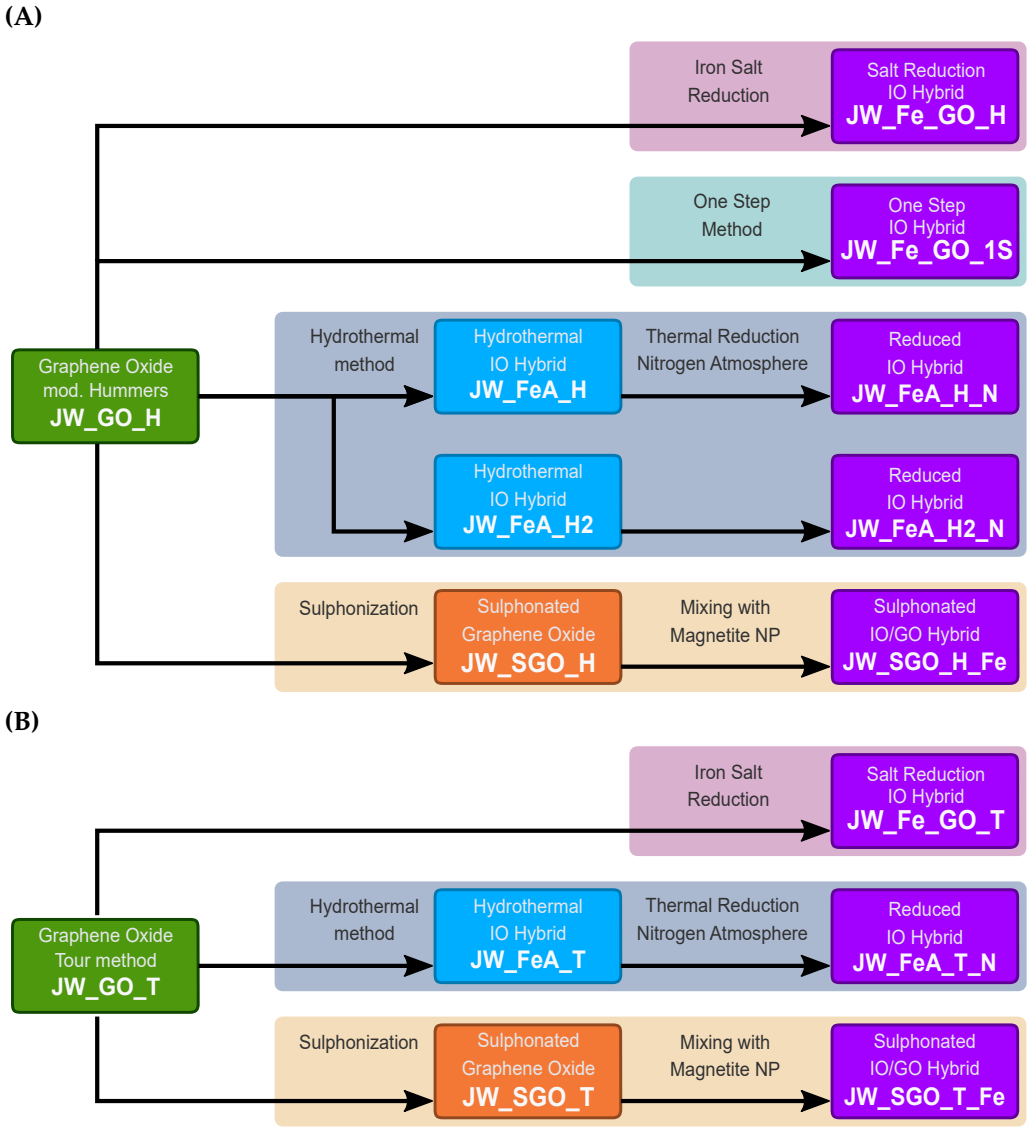

Figure 18 The overview of the prepared materials including samples labels differentiate with respect to the starting material: **(A)** GO prepared by modified Hummers method, **(B)** GO prepared by Tour method.

3.1. Graphene oxide prepared by the modified Hummers Method

The first GO was prepared by the modified Hummers method. Our procedure was inspired by previous works [23][84], with small adjustments. The mixture of concentrated sulphuric acid and potassium permanganate was used to introduce the oxygen-containing groups into graphite via oxidation. Sodium nitrate acts as a catalyst for the reaction and helps to decrease the number of layers of the final GO [85]. Hydrogen peroxide (30% concentration) was used to quench the residual unreacted potassium permanganate. The synthesis was performed in a 500 mL round-bottomed flask with magnetic stirring bar. The final material was labelled as **JW_GO_H**.

Starting materials:

- Graphite, Sigma-Aldrich $\sim$ 20 µm flakes, $m_{\mathrm{G}} = 1\,\mathrm{g}$
- Sulphuric acid (H_2SO_4), Lach-Ner 96% concentration, $V_{\mathrm{H_2SO_4}} = 46\,\mathrm{mL}$
- Sodium nitrate ($NaNO_3$), Sigma-Aldrich, $m_{\mathrm{NaNO_3}} = 1\,\mathrm{g}$
- Potassium permanganate ($KMnO_4$), Penta, $m_{\mathrm{KMnO_4}} = 6\,\mathrm{g}$
- Deionized water, $V_{\mathrm{H_2O}}$ =250 mL
- Hydrogen peroxide (H_2O_2), Sigma-Aldrich 30% concentration, $V_{\mathrm{H_2O_2}} = 20\,\mathrm{mL}$

Procedure:

1. Graphite was added to the flask placed in an ice bath (T = 0 °C).
2. H_2SO_4 was slowly added at T = 0 °C with 15 minutes stirring after addition.
3. $NaNO_3$ was slowly added at T = 0 °C with 30 minutes stirring after addition.
4. The suspension was oxidated with slow addition of $KMnO_4$ at T = 0 °C.
5. The mixture was heated to T = 35 °C in the oil bath.
6. 100 mL of deionized water were slowly poured into the mixture.
7. The temperature was raised to T = 90 °C and the suspension stirred for 1 hour.
8. The suspension was cooled to room temperature naturally, 150 mL of deionized water were added, followed by 20 mL of H_2O_2.
9. The brown suspension was stirred over night at room temperature.
10. The final product was washed several times with deionized water via centrifugation (13500 RPM, 10 minutes per cycle).
11. The suspension was frozen to -80 °C and then they undergo sublimation by vacuum in lyophilizer for two days.

The TEM images (Fig.19) show few layered folded flakes with lateral size of approximately 1 µm.

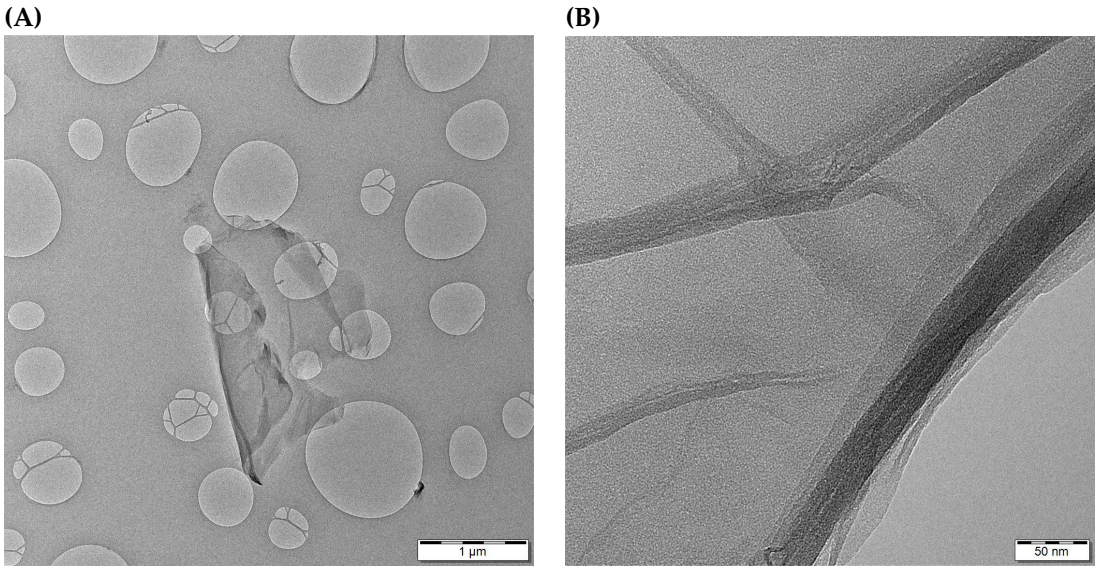

Figure 19 | TEM images of JW_GO_H.

The FT-IR spectrum of **JW_GO_H** (Fig. 20A) shows oxygen functionalities bands at 3420 cm^{-1} (O-H), 1740 cm^{-1} (C=O carboxyl/carbonyl group) and 850 – 1380 cm^{-1} (C-O). The C-O band region can be distinguished into several components involving C-O epoxy (bending $\sim$ 860 cm^{-1} and stretching 1220 cm^{-1}), C-O alkoxy ($\sim$1047 cm^{-1}), and C-O carboxyl (1384 cm^{-1}) [71][72]. The contribution of the aromatic C=C band (1620 cm^{-1}) is relatively small compared to the oxygen-containing bands, which suggests high level of oxygen functionalization.

The Raman spectrum (Fig. 20B) was carried out using the 633 nm diode laser (excitation power 5 mW) with 50$\times$ objective in the front of the sample. The baseline of the final Raman spectrum was corrected using Origin 2016. All main carbon band can be distinguished (D band at 1339 cm^{-1}, G band at 1599 cm^{-1}, and 2D band at $\sim$ 2500–3200 cm^{-1}) and the I_D/I_G ratio was calculated as 1.15, which indicates high amount of sp^3 carbon, defects, and oxygen functionalization [64][66].

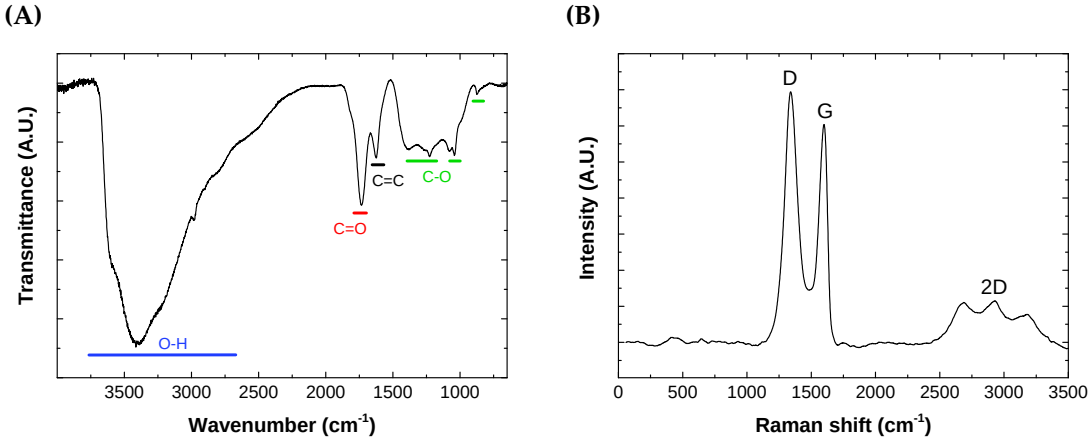

Figure 20 | Vibration spectroscopy of JW_GO_H: **(A)** FT-IR spectrum of JW_GO_H showing high functionalization with oxygen-containing groups, **(B)** Raman spectrum of JW_GO_H with I_D/I_G=1.15.

XPS elemental survey (Fig. 21) revealed the presence of carbon ($\sim$ 66.25%), oxygen ($\sim$ 32.44%), nitrogen ($\sim$ 0.9%) and sulphur ($\sim$ 0.41%). The bonding and oxidation states of carbon were determined from the deconvolution of the high resolution XPS spectrum. C1s peak of high resolution

XPS spectrum (Fig. 22A) shows the following functionalities: C-C sp^2 at 283.81 eV (∼ 14.13%), C-C sp^3 at 284.87 eV (∼ 33.08%), C-O at 286.92 eV (∼ 41.86%), C=O at 288.25 eV (∼ 7.9%), and O=C-OH at 289.24 eV (∼ 3.03%). The higher amount of sp^3 carbon suggests the presence of vacancies, defects, and high level of oxygen functionalization. It has to be mentioned that the precise determination of the amount of sp^3 and sp^2 carbon is not possible, due to the asymmetric shape of sp^2 component and peak overlapping [74]. Deconvoluted O1s peak of high resolution XPS spectrum (Fig. 22B) consists of C=O at 531.08 eV (∼ 4.88%), C-O at 532.62 eV (∼ 89.42%), and O=C-OH at 533.91 eV (∼ 5.7%). The comparison of C1s and O1s bands indicates that C-O functionality is preferred over C=O and O=C-OH.

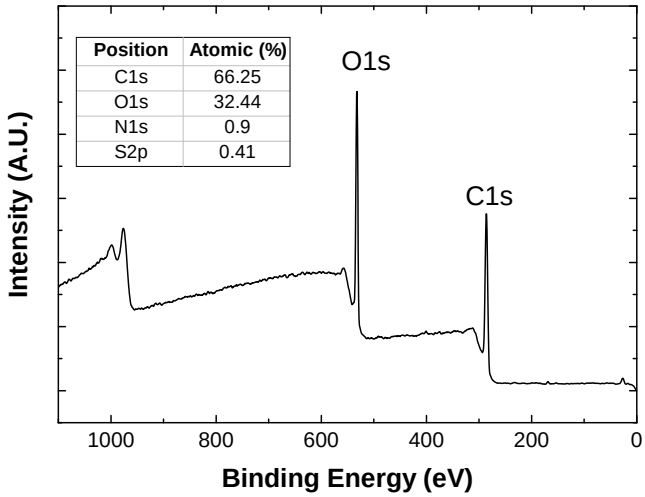

Figure 21 | XPS elemental survey of JW_GO_H.

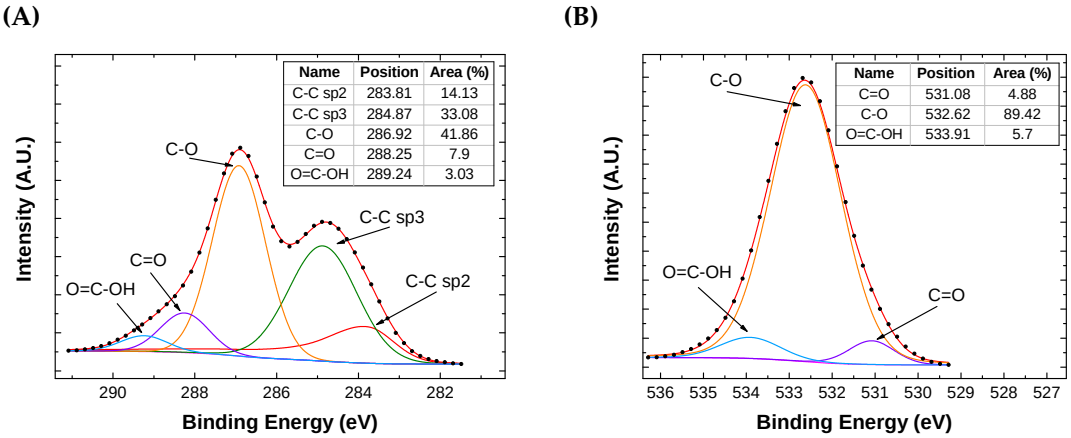

Figure 22 | High resolution XPS spectra of JW_GO_H: **(A)** C1s peak, **(B)** O1s peak.

The STA-MS measurement of **JW_GO_H** (Fig. 23A and Fig. 23B) was performed in Al_2O_3 crucible in temperature range from 40 to 1000 °C with heating rate 10 K min^{-1} under synthetic air (flow rate 70 mL min^{-1}) with N_2 used as a protective gas (flow rate 10 mL min^{-1}). The initial mass loss can be identified as the evaporation of physisorbed water, which can be confirmed by m/z=18 detection by MS. The first exothermic process at 225 °C (from DSC chart: onset 212 °C, end 238 °C, enthalpy $-557.9\,J\,g^{-1}$) can be assigned to the evaporation of chemisorbed water and carbon combustion. The combustion of carbon can be associated to the detection of m/z=44 by MS, which can be identified as CO_2. The second exothermic process at 470 °C (from DSC chart: onset 468 °C, end 510 °C, enthalpy $-3210\,J\,g^{-1}$) is the burning of the residual graphitic backbone. The ash content after the whole process is 1.08%.

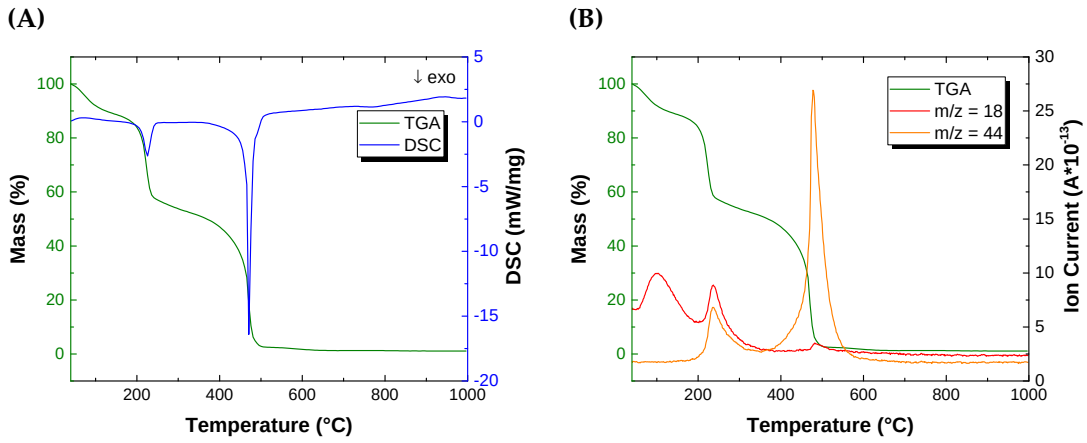

Figure 23 STA-MS measurement in temperature range from 40 to 1000 °C (heating rate 10 K min^{-1}) under synthetic air (flow rate 70 mL min^{-1}) with N_2 used as a protective gas (flow rate 10 mL min^{-1}): **(A)** STA of JW_GO_H and **(B)** TGA-MS of JW_GO_H.

In conclusion, all characterisation techniques confirmed the high amount of oxygen-containing groups, making the material suitable for hybrid system formation.

3.2. Graphene oxide prepared by the Tour Method

The second GO was prepared by Tour method. This method is safer, easier and reportedly provides a greater extend of oxidation than the modified Hummers method [24]. The result of the synthesis strongly depends on the quality of the graphite used as starting material, but we did not explore different providers and the same graphite used for modified Hummers method was utilised. The reaction mechanism is similar to modified Hummers method, the main differences being the use of a $\sim$ 9:1 mixture of concentrated sulphuric and phosphoric acid , higher amount of potassium permanganate, and exclusion of sodium nitrate. The synthesis was performed in a 500 mL round-bottomed flask with magnetic stirring bar. The final material is labelled as **JW_GO_T**.

Starting materials:

- Graphite, Sigma-Aldrich, $\sim$ 20 µm flakes, $m_G = 1$ g
- Sulphuric acid (H_2SO_4), Lach-Ner 96% concentration, $V_{H_2SO_4} = 120$ mL
- Phosphoric acid (H_3PO_4), Sigma-Aldrich 75% concentration, $V_{H_3PO_4} = 14$ mL
- Potassium permanganate ($KMnO_4$), Penta, $m_{KMnO_4} = 6$ g
- Hydrogen peroxide (H_2O_2), Sigma-Aldrich 30% concentration, $V_{H_2O_2} = 3$ mL
- Ice from deionized water, $V_{ice} \cong 300$ mL

Procedure:

1. Graphite flakes and $KMnO_4$ were added into $\sim$ 9:1 mixture of concentrated H_2SO_4/H_3PO_4 at T = 0 °C (ice bath), causing slight exothermic reaction and the temperature raised up to $\sim$40 °C.
2. The reaction was heated to 50 °C and stirred for 20 hours.
3. The suspension was cooled down to room temperature and poured into ice ($\sim$400 mL) with addition of 30% H_2O_2.
4. The mixture was washed by deionized water and filtered through ashless filter paper (Fisher Scientific).

5. The filtrate (**JW_GO_T1**) and the residual material on the filter (**JW_GO_T2**) were washed separately several times with deionized water via centrifugation (13000 RPM, 10 minutes per cycle).

6. The final product was dried under vacuum (20–30 mbar) overnight.

In the original preparation [24], the authors use only the filtrate for further analysis. We decided to make an initial measurement by XPS to investigate the difference between elemental composition and oxidation states of **JW_GO_T1** and **JW_GO_T2**. XPS elemental survey (Fig. 24A and Fig. 24B) revealed that **JW_GO_T1** has slightly higher amount of oxygen (T1: 38.37%, T2: 37.17%) and sulphur (T1: 2.23%, T2: 1.5%) than **JW_GO_T2** and lower amount of carbon (T1: 58.11%, T2: 60.44%). However, the shape of C1s peak of high resolution XPS spectrum of **JW_GO_T2** is not typical for GO and oxygen-containing groups are more abundant than carbon ones (see Fig. 25A and Fig. 25B for detailed comparison). High resolution XPS spectrum of O1s peak of **JW_GO_T2** (Fig. 26B) is broader than that of **JW_GO_T1** (Fig. 26A), which suggests a larger variety of oxygen functional groups. After XPS analysis, we decided that only the GO obtained from the filtrate (**JW_GO_T1**) will be used for further synthesis and it will be labelled as **JW_GO_T** for the rest of the work.

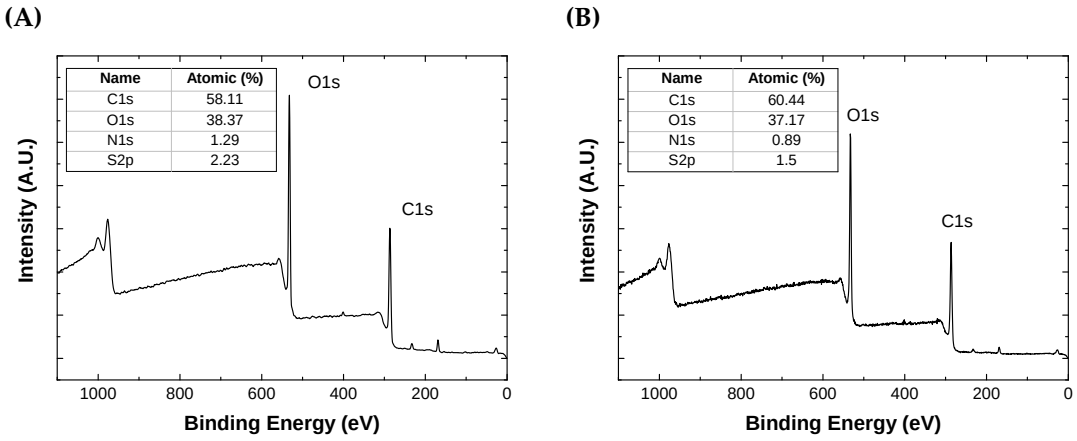

Figure 24 | XPS elemental survey of **(A)** JW_GO_T1 and **(B)** JW_GO_T2.

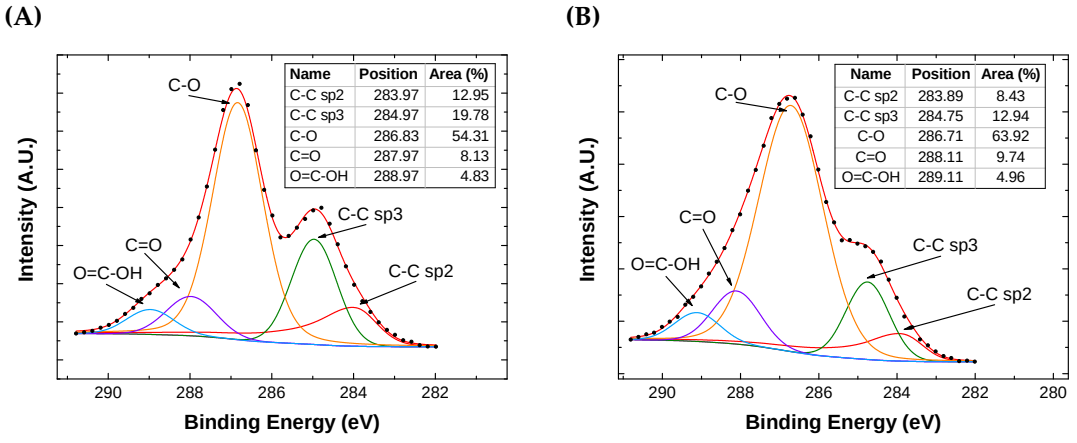

Figure 25 | High resolution XPS spectrum of C1s peak of **(A)** JW_GO_T1 and **(B)** JW_GO_T2.

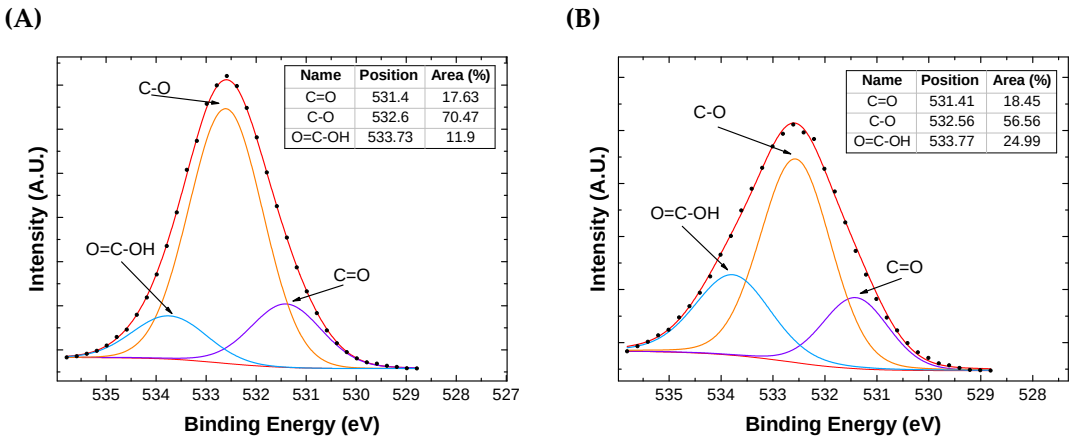

Figure 26 | High resolution XPS spectrum of O1s peaks of **(A)** JW_GO_T1 and **(B)** JW_GO_T2.

TEM images show a folded few layered structure with lateral size under 1 µm (Fig.27).

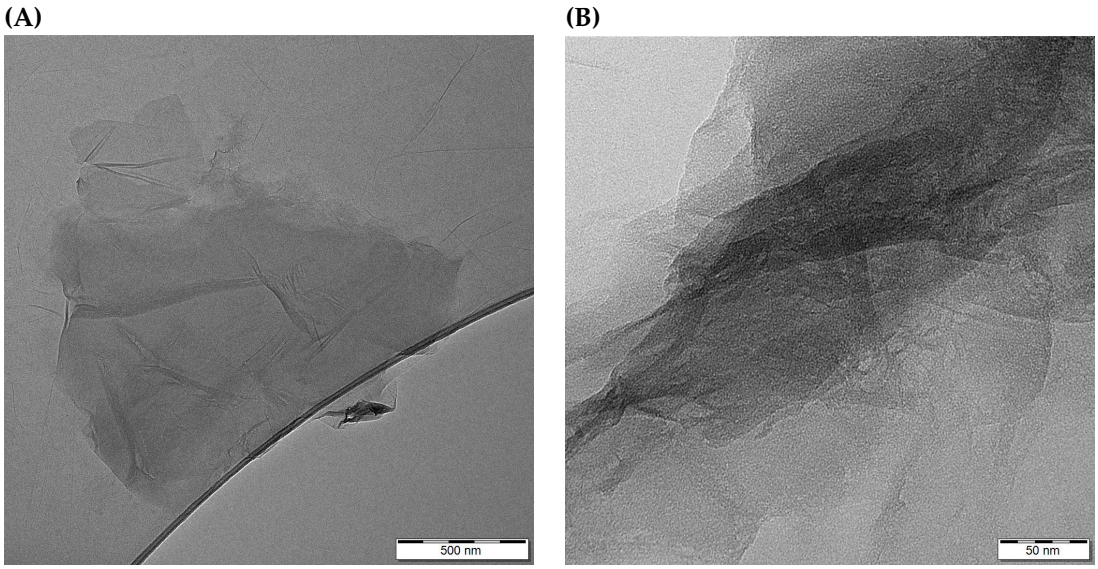

Figure 27 | TEM images of JW_GO_T.

Similarly to **JW_GO_H**, the FT-IR spectrum of **JW_GO_T** (Fig. 28A) revealed the presence of oxygen-containing groups (O-H at 3358 cm^{-1}, C=O carboxyl/carbonyl at 1740 cm^{-1}, C-O at 850–1380 cm^{-1}), which have higher intensity than the C=C band (1637 cm^{-1}). The sharp absorption bands at 2874 cm^{-1} and 2897 cm^{-1} correspond to the symmetric and anti-symmetric stretching vibration of CH.

The Raman spectrum (Fig.28B) was measured by 633 nm diode laser (excitation power 8 mW) with 50× objective in the front of the sample. After the baseline correction of the Raman spectrum, the intensity ratio of the D band (1338 cm^{-1}) and G band (1599 cm^{-1}) was determined as $I_D/I_G = 1.13$, which is very close to that of **JW_GO_H** ($I_D/I_G = 1.15$).

In conclusion, **JW_GO_T** is more oxidized and shows more variety of oxygen-containing groups than **JW_GO_H**, as predicted by the literature [24].

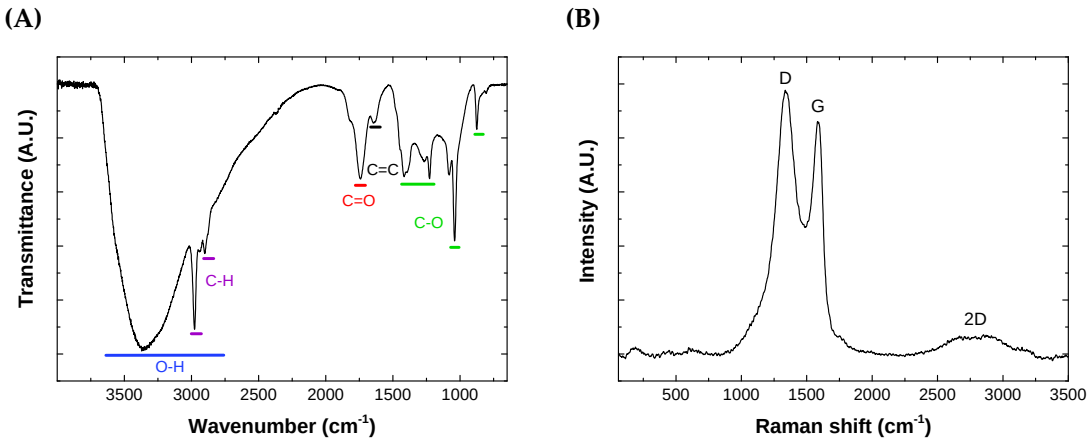

Figure 28 Vibration spectroscopy: **(A)** FT-IR spectrum of JW_GO_T display high level of functionalization with oxygen-containing groups. **(B)** Raman spectrum of JW_GO_T with $I_D/I_G = 1.13$.

3.3. Single-step hybrid preparation

The first hybrid system was made by single-step synthesis [86]. These type of techniques should provide faster way of production and good coverage of iron oxide on GO. The GO-iron oxide hybrid is created by high temperature reaction of ferric acetylacetonate with GO in 1-methyl-2-pyrrolidone. The final sample is labelled as **JW_Fe_GO_1S**.

Starting material:

- GO made by modified Hummers method, **JW_GO_H**, $m_{\text{JW\_GO\_H}} = 99.8\,\text{mg}$
- 1-methyl-2-pyrrolidone (NMP), Sigma-Aldrich, $V_{\text{NMP}} = 50\,\text{mL}$
- Ferric acetylacetonate ($Fe(acac)_3$), Sigma-Aldrich, $m_{Fe(acac)_3} = 1.414\,\text{g}$

Procedure:

1. GO was sonicated in 30 mL of NMP for 1 hour.
2. The solution was heated to 180 °C (oil bath) under nitrogen atmosphere.
3. $Fe(acac)_3$ was dissolved in 20 mL of NMP.
4. The solution of $Fe(acac)_3$ was added dropwise into the GO suspension under vigorous stirring and kept stirred for 1 hour.
5. After cooling to room temperature, the mixture was poured into ethanol and the solid part was isolated by centrifugation (13000 RPM, 10 minutes per cycle).
6. The sample was washed 5 times with acetone via centrifugation (13000 RPM, 10 minutes) and several times with water.
7. The final product was dried under the vacuum.

JW_Fe_GO_1S was measured by STA-MS (Fig. 29A and Fig. 29B) under the same condition as **JW_GO_H** (temperature range from 40 to 1000 °C with heating rate 10 K min^{-1} under synthetic air with flow rate 70 mL min^{-1} and N_2 used as a protective gas with flow rate 10 mL min^{-1}, sample loaded into Al_2O_3 crucible). The initial loss (until ~180 °C) can be assigned to the evaporation of physisorbed water (MS detection of m/z=18). The main mass loss occurs in the temperature range between 180 and 480 °C with enthalpy of $-10\,901\,\text{J g}^{-1}$, which can be assigned to the evaporation of chemisorbed water and the combustion of GO (MS detection of m/z=18 and m/z=44). The residual mass at 1000 °C was 19.30%, which indicates a relatively low amount of iron in the hybrid material.

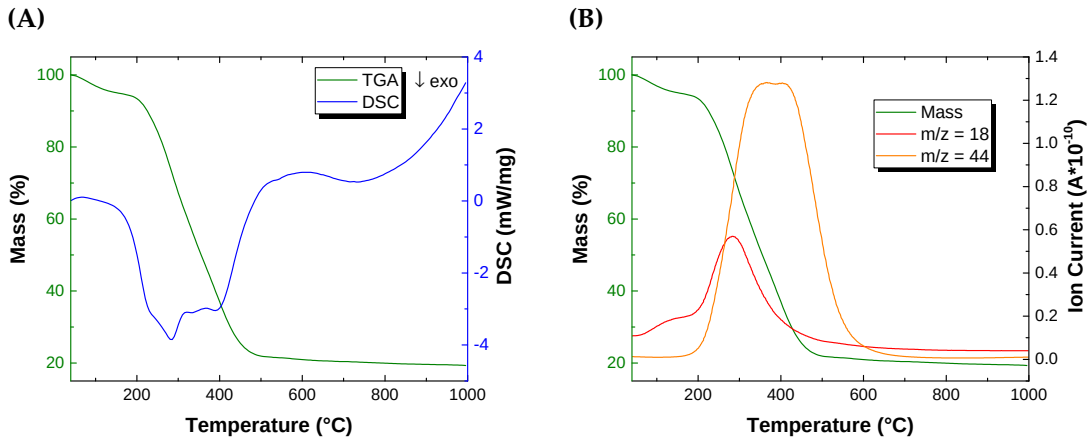

Figure 29 STA-MS measurement in temperature range from 40 to 1000 °C (heating rate 10 K min^{-1}) under synthetic air (flow rate 70 mL min^{-1}) with N_2 used as a protective gas (flow rate 10 mL min^{-1}): **(A)** STA of JW_Fe_GO_1S and **(B)** TGA-MS of JW_Fe_GO_1S.

The low iron oxide content may be caused by a low temperature of $Fe(acac)_3$ decomposition. We decided to stop the characterization of **JW_Fe_GO_1S** and move to other syntheses.

3.4. Multi-step hybrid preparation

3.4.1. Iron(II) and iron(III) salts decomposition

The GO-iron oxide composite was prepared by decomposition of iron(II) and iron(III) salts in the presence of GO. The aim of the synthesis was to functionalise the GO surface with magnetite nanoparticles. It is critical to keep ratio between iron(II) and iron(III) salt at 1:2 to obtain magnetite nanoparticles. The magnetite formation is initialized by addition of ammonia solution (25–29% concentration), which changes pH towards basic. The same procedure was used for both GOs (**JW_GO_H** and **JW_GO_T**) and the final products were labelled as **JW_Fe_GO_H** and **JW_Fe_GO_T** with respect to the GO used. The synthesis was performed in two round-bottomed flasks (100 mL and 250 mL).

Starting materials:

- GO made by modified Hummers method, **JW_GO_H**, $m_{JW\_GO\_H} = 208$ mg
- GO made by Tour method, **JW_GO_T**, $m_{JW\_GO\_T} = 194$ mg
- Iron(II) chloride tetrahydrate ($FeCl_2 \cdot 4H_2O$), Sigma-Aldrich, $m_{FeCl_2 \cdot 4H_2O} = 0.86$ g
- Iron(III) chloride hexahydrate ($FeCl_3 \cdot 6H_2O$), Sigma-Aldrich, $m_{FeCl_3 \cdot 6H_2O} = 2.34$ g
- Ammonia solution (NH_4OH), Penta 25–29% concentration, $V_{NH_4OH} = 5$ mL
- Ascorbic acid – spatula tip

Procedure:

1. GO was added into water and sonicated for 20 minutes in 100 mL round-bottomed flask.
2. The GO suspension was transferred to the 250 mL flask and vigorously bubbled with nitrogen for 20 minutes.
3. A spatula tip of ascorbic acid is added into suspension to prevent Fe^{2+} oxidation.
4. To obtain magnetite nanoparticles $FeCl_2 \cdot 4H_2O$ was added first, followed by $FeCl_3 \cdot 6H_2O$.
5. Ammonia solution was added slowly into the mixture.

6. The magnetic suspension was stirred for 30 minutes and then collected on the bottom by a magnet.
7. The suspension was washed several times with water and ethanol via centrifugation (13500 RPM, 10 minutes per cycle).
8. The final product was dried under vacuum (20–30 mbar) overnight.

TEM images revealed a dense coverage of iron oxide nanoparticles on both **JW_Fe_GO_T** (Fig. 30A) and **JW_Fe_GO_H** (Fig. 30B). The lateral size of iron oxide nanoparticles can be estimated at ∼10 nm. The EDS was measured on a carbon-coated copper grid, which shows the presence of iron and oxygen. The EDS charts with the TEM image of investigated area can be found in appendix A.1.

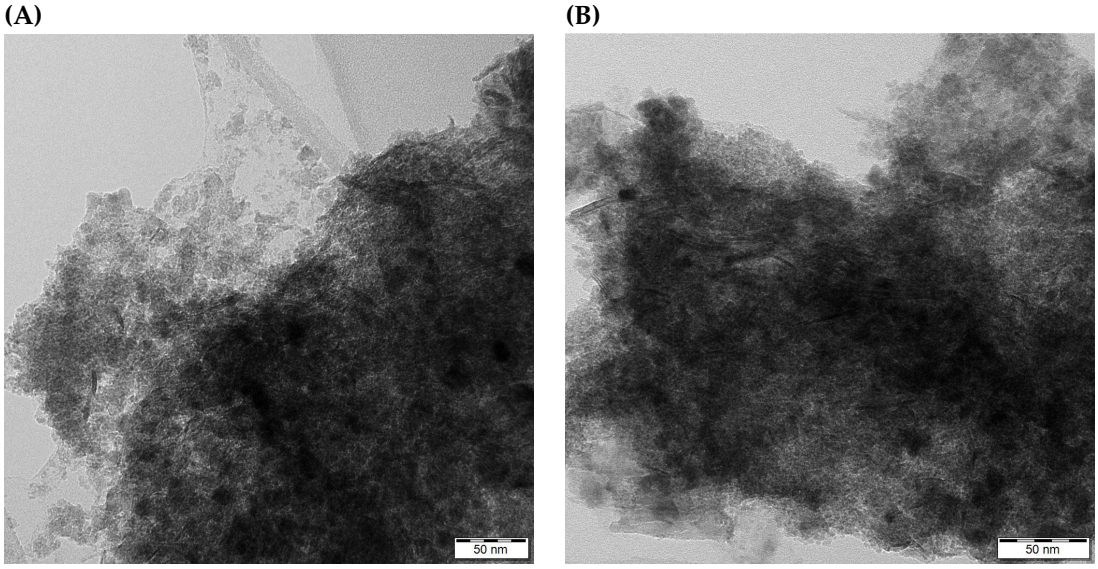

Figure 30 TEM images showing GO densely covered by iron oxide nanoparticles: **(A)** JW_Fe_GO_T and **(B)** JW_Fe_GO_H.

The intensity of FT-IR spectra of GOs (**JW_GO_T** and **JW_GO_H**) and GO-iron oxide composites (**JW_Fe_GO_T** and **JW_Fe_GO_H**) were normalised from 0 to 100 with respect to O-H band of each spectrum, due to the generally low transmittance intensity of both GO-iron oxide composites. The FT-IR spectra of both composites (Fig. 31A and Fig. 31B) show a significant decrease in intensity of oxygen-containing groups compared to the corresponding GO. The O-H band (3340 cm^{-1}) is present in both structures and can be identified as absorbed water on the surface of the material. The broad band from ∼1720 cm^{-1} to ∼1480 cm^{-1} can be assigned to C=O and C=C bonds. The wavenumber of C=O bond may be shifted due to the formation of $-COO^-$ after iron oxide nanoparticles anchoring [87]. The intensity of C-O bands is decreased in both **JW_Fe_GO_T** and **JW_Fe_GO_H** compared to those observed in GO alone.

The Raman spectra (Fig. 31C and Fig. 31D) were obtained using 633 nm diode laser (excitation power 0.5 mW) with 50× objective in the front of the sample. The excitation power had to be kept under 1 mW to prevent heating of the sample and phase transition of iron oxide nanoparticles [67][68][69]. The I_D/I_G ratios of **JW_Fe_GO_T** and **JW_Fe_GO_H** were calculated as 1.23 and 1.35, respectively. The Raman spectrum of **JW_Fe_GO_H** shows five peaks in the low energy region (219 cm^{-1}, 286 cm^{-1}, 399 cm^{-1}, 597 cm^{-1}, and 656 cm^{-1}), which can be identified as traces of goethite (α-FeOOH) and lepidocrocite (γ-FeOOH) [88].

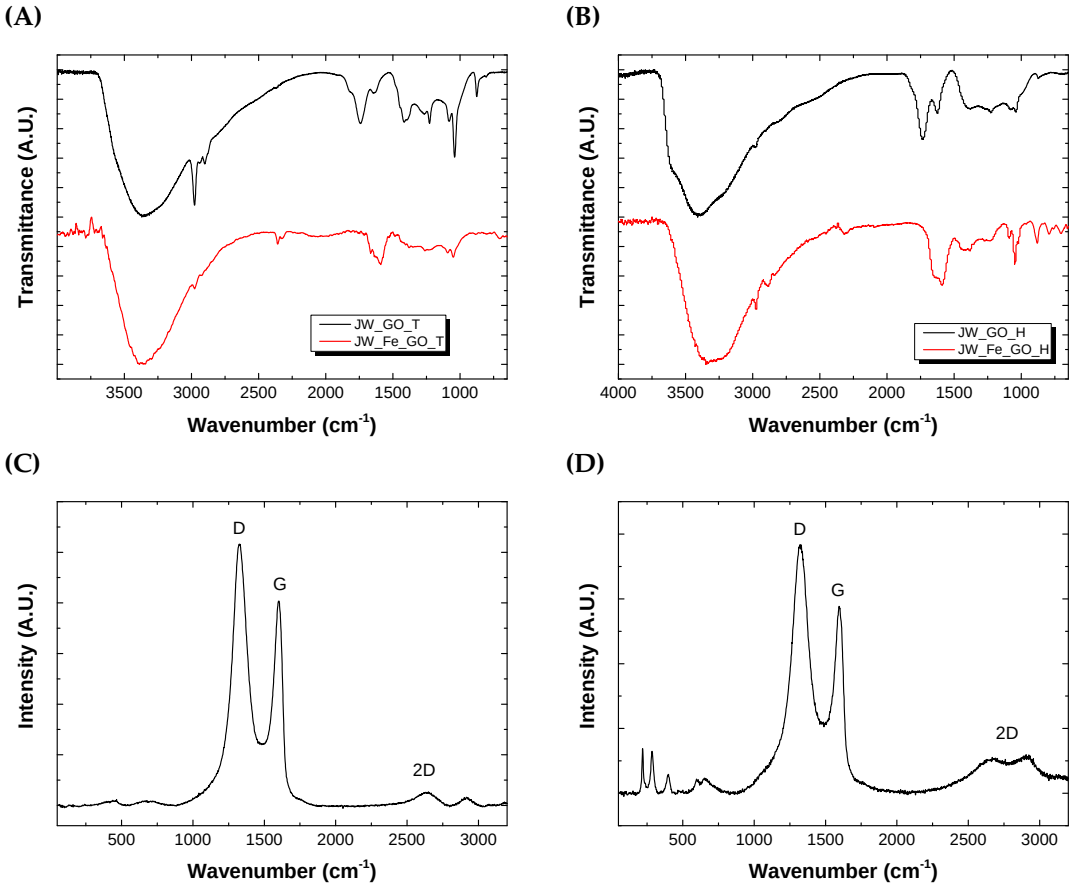

Figure 31 FT-IR spectra normalized from 0 to 100 with respect to O-H band of each structure, showing a general decrease in oxygen-containing groups of GO-iron oxide composites: **(A)** JW_Fe_GO_T, **(B)** JW_Fe_GO_H.
Raman spectra of **(C)** JW_Fe_GO_T and **(D)** JW_Fe_GO_H with I_D/I_G ratios 1.23 and 1.35, respectively.

Both samples (**JW_Fe_GO_T** and **JW_Fe_GO_H**) were analysed by XPS, which revealed the presence of the following major elements (Fig. 32A and Fig. 32B): carbon (T: 36.81%, H: 34.8%), oxygen (T: 43.27%, H: 45.72%), and iron (T: 17.21%, H: 17.99%). The high resolution XPS spectra of the Fe2p peak (Fig. 32C and Fig. 32D) consist of two peaks ($Fe2p_{3/2}$ at ∼711 eV and $Fe2p_{1/2}$ at ∼725 eV). The shape of the high resolution XPS spectra of Fe2p and the position of $Fe^{3+}Fe2p_{3/2}$ satellite feature suggest the presence of Fe^{3+} [89]. It has to be mentioned that XPS is mainly surface-sensitive technique and is not the ideal method for precise determination of oxidation states of iron and phases of iron oxide nanoparticles. These information have to be confirmed with other techniques, such as Mössbauer spectroscopy and XRD. As already mentioned in section 1.6.4, iron oxide nanoparticles can be anchored to GO via Fe-OC or Fe-C bonds. In the case of Fe-C bond, the two peaks are simultaneously detected in high resolution spectrum of C1s and Fe2p at 283.3 eV and at 707.5 eV, respectively. Due to the fact that XPS spectra of both GO-iron oxide composites do not display any of these peaks, we assume that iron oxide nanoparticles are bounded to GO via Fe-OC bond [56][90]. The deconvoluted C1s peaks of high resolution XPS spectra of both hybrid composites (Fig. 32E and Fig. 32F) show the following bonds: C-C sp^2 (∼284.7 eV), C-C sp^3 (∼285.5 eV), C-O (∼286.8 eV), and C=O (∼288.7 eV). The decrease in the relative intensity of C1s oxygen-containing bonds compared to the non-functionalized GO also supports the formation of Fe-OC bond. The XPS high resolution spectra of O1s peak (Fig. 32G and Fig. 32H) show a shift towards lower binding energies than in the case of pristine GO, which indicates the presence of Fe-O bond (∼530 eV) standing for the lattice oxygen of magnetite [90]. The peak at 531.55 eV can be identified as Fe-OC bond or C=O bond (531.2 eV). However, considering that the intensity of C=O peak is lower in pure GO, we assume that the peak at 531.55 eV originates mainly from Fe-OC bond [90].

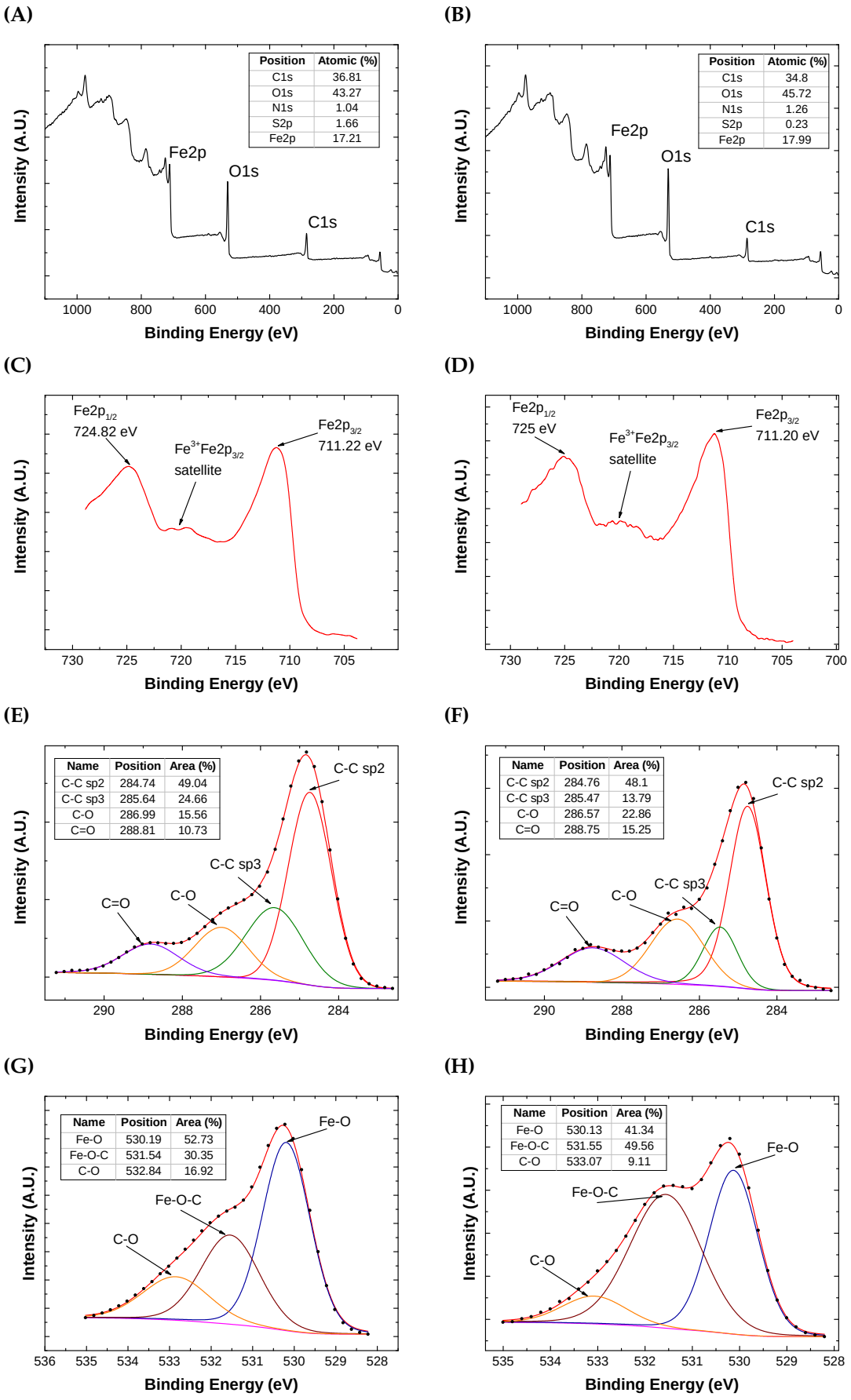

Figure 32 XPS spectra of GO-iron oxide compound prepared by iron salts decomposition: **(A)** JW_Fe_GO_T elemental survey, **(B)** JW_Fe_GO_H elemental survey, **(C)** JW_Fe_GO_T Fe2p, **(D)** JW_Fe_GO_H Fe2p, **(E)** JW_Fe_GO_T C1s, **(F)** JW_Fe_GO_H C1s, **(G)** JW_Fe_GO_T O1s, **(H)** JW_Fe_GO_H O1s.

The XRD patterns of both composites were analysed by Rietveld method (see fit in Appendix B.1A and B.1B). The iron oxide part of **JW_Fe_GO_T** (Fig. 33A) was determined as magnetite with lattice parameter a =8.371 Å and MCL=10 nm. The phase composition cannot be precisely identified, because the value of lattice parameter lies between the lattice parameter of maghemite (a =8.351 Å) and magnetite (a =8.396 Å), low MCL, and peak broadening. The XRD pattern of **JW_Fe_GO_H** (Fig. 33B) shows multi-phase system consisting of magnetite/maghemite (76.8%, a =8.381 Å, MCL=15 nm), goethite (16.4%, MCL=13 nm) and lepidocrocite (6.8%, MCL=19 nm). The presence of the hydrated phases may be caused by the aqueous environment where the synthesis took place or due to the oxidation of the unreacted Fe^{2+} residues in air after the synthesis.

The room temperature ^{57}Fe zero-field Mössbauer spectra of both compounds (Fig. 33C and Fig. 33D) show one dublet component, which can be assigned to small Fe^{3+} nanoparticles in superparamagnetic state with respect to the hyperfine parameters of the fit (Table 4) confirming that the size is below 20 nm in agreement with TEM and XRD.

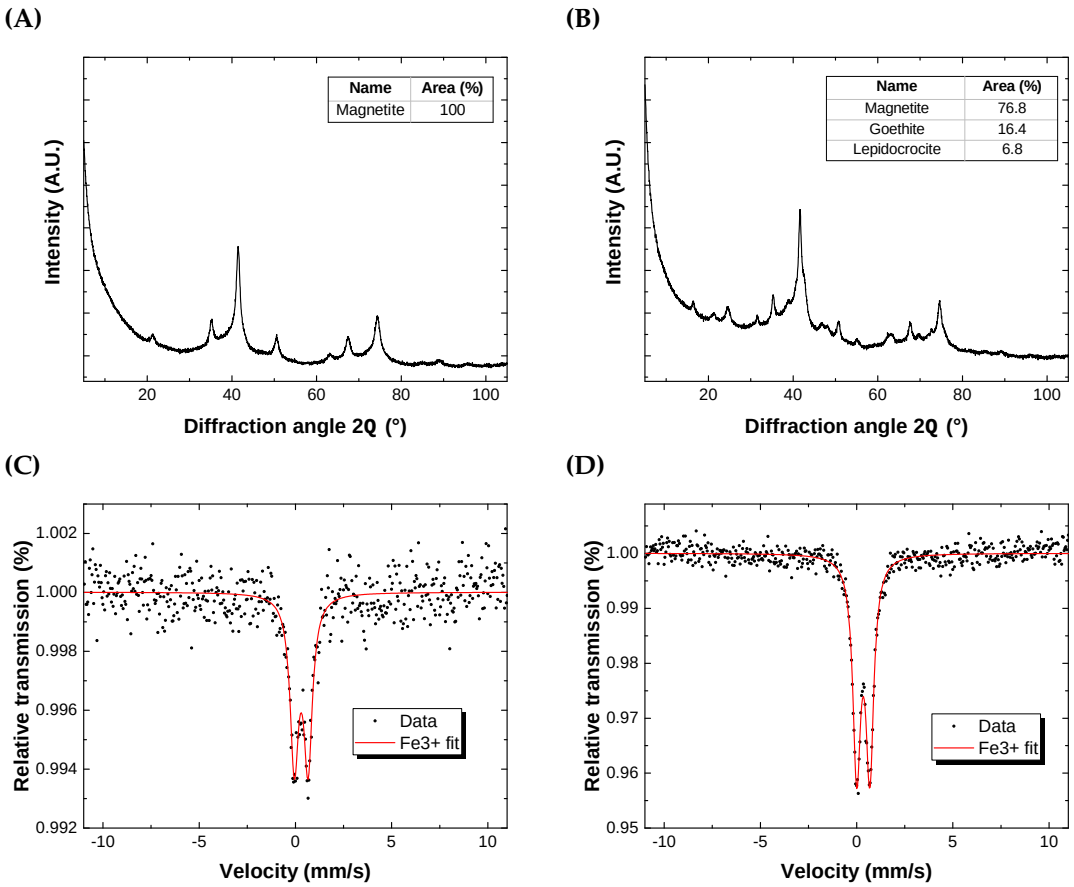

Figure 33 XRD patterns of **(A)** JW_Fe_GO_T and **(B)** JW_Fe_GO_H. The room temperature ^{57}Fe zero-field Mössbauer spectra of **(C)** JW_Fe_GO_T and **(D)** JW_Fe_GO_H.

Sample Component	**Isomer shift** δ (mm s^{-1})	**Quadrupole splitting** δE_Q (mm s^{-1})	**Component relative spectral area** (%)
JW_Fe_GO_T			
Fe^3+ doublet	0.30	0.71	100
JW_Fe_GO_H			
Fe^3+ doublet	0.35	0.68	100

Table 4 The hyperfine parameters of the room temperature ^{57}Fe zero-field Mössbauer spectra of JW_Fe_GO_T and JW_Fe_GO_H.

The amount of iron contained in the GO-iron oxide compounds was determined by STA-MS measurement in the temperature range from 40 to 1000 °C (heating rate 10 K min^{-1}) under synthetic air (flow rate 70 mL min^{-1}) and N_2 used as a protective gas (flow rate 10 mL min^{-1}). Samples were loaded into an Al_2O_3 crucible. The TGA shows the continued loss of mass from the beginning of the process until ~400 °C for both samples. According to DSC, that area can be divided into two regions in the case of **JW_Fe_GO_T** (Fig. 34A and Fig. 34B). The first mass loss occurs from 95 to 235 °C (enthalpy −106.9 J g^{-1}) and can be associated with the evaporation of physisorbed water from the sample (m/z=18 from MS). The second loss from 280 to 400 °C (enthalpy −1060 J g^{-1}) can be assigned to the combustion of carbon, as indicated by the previous STA-MS measurement of **JW_GO_H** (Fig. 23A) and the presence of m/z=44 in MS. The residual mass at 1000 °C is 77.45% suggesting high amount of iron in the structure.

The DSC chart of **JW_Fe_GO_H** (Fig. 34C) shows an exothermic process taking place in 3 steps. The first one (120–225 °C, enthalpy −62.45 J g^{-1}) is probably due to the evaporation of physisorbed water from the sample (m/z=18 from MS). The second (240–273.2 °C, enthalpy −23.53 J g^{-1}) and the third process (296.8–398.4 °C, enthalpy −461.2 J g^{-1}) stand for the evaporation of the residual water and the combustion of carbon (m/z=44 from MS). The residual mass shown by the TGA chart at 1000 °C is 75.58%.

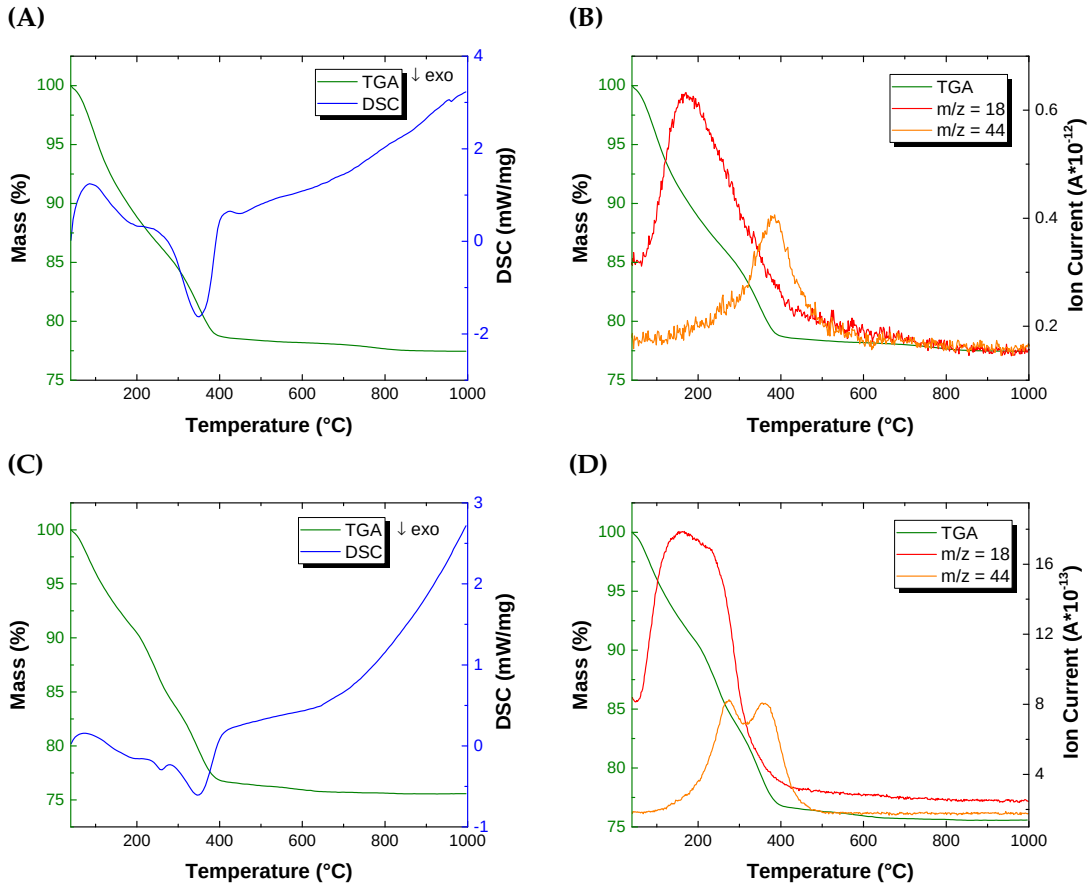

Figure 34 STA-MS measurement in temperature range from 40 to 1000 °C (heating rate 10 K min^{-1}) under synthetic air (flow rate 70 mL min^{-1}) with N_2 used as a protective gas (flow rate 10 mL min^{-1}). **(A)** JW_Fe_GO_T TGA/DSC, **(B)** JW_Fe_GO_T TGA/MS, **(C)** JW_Fe_GO_H TGA/DSC, **(D)** JW_Fe_GO_H TGA/MS.

In conclusion, both composites show high amount of iron oxide nanoparticles, which is confirmed by TEM images and high residual mass from TGA at 1000 °C. The multi-phase composition of **JW_Fe_GO_H** was confirmed by Raman spectroscopy and XRD. The iron oxide part of both materials cannot be distinguished precisely due to the small particle size (10-20 nm MCL from XRD

measurements). Data provided by XPS suggest Fe-OC anchoring mechanism between iron oxide nanoparticles and GO. The iron oxide nanoparticles of both GO-iron oxide hybrid systems possess superparamagnetic behaviour observed as one Fe^{3+} doublet in the room temperature ^{57}Fe zero-field Mössbauer spectra.

3.4.2. Hydrothermal method

In the first part of hydrothermal procedure, hematite nanoparticles are prepared by hydrothermal reaction in a Teflon lined stainless steel autoclave in the presence of GO. In a separate follow-up procedure, part of the product is subsequently thermally treated under nitrogen atmosphere up to 500 °C (heating rate 2 °C min^{-1}), maintained at 500 °C for 2 h, and then left cooling to room temperature. The thermal treatment is done in order to reduce oxygen-containing groups of GO and the resulting material is compared to the fraction that did not undergo the thermal treatment under nitrogen. The GOs used for the synthesis were those prepared by modified Hummers method (**JW_GO_H**) and Tour method (**JW_GO_T**). In the case of **JW_GO_H**, GO-iron oxide composites were synthesised using two different ratios between **JW_GO_H** and iron(III) chloride hexahydrate (1:6 and 1:3) to investigate the rate and density of the iron oxide coverage. The GO-iron oxide hybrid systems with **JW_GO_T** as the starting material were prepared only with the ratio 1:6 between GO and iron(III) chloride hexahydrate. For detailed sample labels see Table 5.

GO	GO:$FeCl_3 \cdot 6H_2O$ ratio	Reduction	Sample Label
JW_GO_H	1:6	–	JW_FeA_H
JW_GO_H	1:3	–	JW_FeA_H2
JW_GO_T	1:6	–	JW_FeA_T
JW_GO_H	1:6	500 °C under N_2 atm.	JW_FeA_H_N
JW_GO_H	1:3	500 °C under N_2 atm.	JW_FeA_H2_N
JW_GO_T	1:6	500 °C under N_2 atm.	JW_FeA_T_N

Table 5 Sample labels of GO-iron oxide composites prepared by hydrothermal method and subsequent thermal treatment under nitrogen atmosphere.

Starting materials for JW_FeA_H and JW_FeA_H_N:

- GO made by modified Hummers method, **JW_GO_H**, $m_{JW\_GO\_H} = 197$ mg
- Iron(III) chloride hexahydrate ($FeCl_3 \cdot 6H_2O$), Sigma-Aldrich, $m_{FeCl_3 \cdot 6H_2O} = 1.22$ g
- Ammonia solution (NH_4OH), Penta 25–29% concentration, $V_{NH_4OH} = 4$ mL
- Deionized water, $V_{H_2O} = 50$ mL

Starting materials for JW_FeA_H2 and JW_FeA_H2_N:

- GO made by modified Hummers method, **JW_GO_H**, $m_{JW\_GO\_H} = 140$ mg
- Iron(III) chloride hexahydrate ($FeCl_3 \cdot 6H_2O$), Sigma-Aldrich, $m_{FeCl_3 \cdot 6H_2O} = 0.4$ g
- Ammonia solution (NH_4OH), Penta 25–29% concentration, $V_{NH_4OH} = 4$ mL
- Deionized water, $V_{H_2O} = 40$ mL

Starting materials for JW_FeA_T and JW_FeA_T_N:

- GO made by Tour method, **JW_GO_T**, $m_{JW\_GO\_T}$ =160 mg
- Iron(III) chloride hexahydrate ($FeCl_3 \cdot 6H_2O$), Sigma-Aldrich, $m_{FeCl_3 \cdot 6H_2O} = 0.96$ g
- Ammonia solution (NH_4OH), Penta 25–29% concentration, V_{NH_4OH} =4 mL
- Deionized water, $V_{H_2O} = 40$ mL

Procedure:

1. GO was dispersed in deionized water via sonication for 1 hour.
2. $FeCl_3 \cdot 6H_2O$ was gradually added to the GO suspension and sonicated for 5 minutes.
3. The mixture was stirred at room temperature for 30 minutes.
4. The ammonia solution was added to the suspension.
5. The suspension was transferred into a Teflon lined stainless steel autoclave and sealed.
6. The Teflon lined stainless steel autoclave was place into the furnace (120 °C) for 16 hours.
7. After furnace cooling to room temperature, the material was washed several times with water and ethanol (centrifugation 13500 RPM, 10 minutes per cycle) and dried under vacuum.
8. Part of the material was thermally treated under nitrogen atmosphere from room temperature to 500 °C (heating rate 2 °C min^{-1}) and maintained at 500 °C for 2 hours.
9. The sample was cooled to room temperature.

The TEM images revealed dense coverage of GO with iron oxide nanoparticles. The diameter of iron oxide nanoparticles was analysed by ImageJ software from all obtained TEM images (Table 6), however only one representative image per sample is shown in this work. The particle size histograms fitted with normal distribution curve are shown within TEM images for each structure in Fig. 35 and Fig. 36.

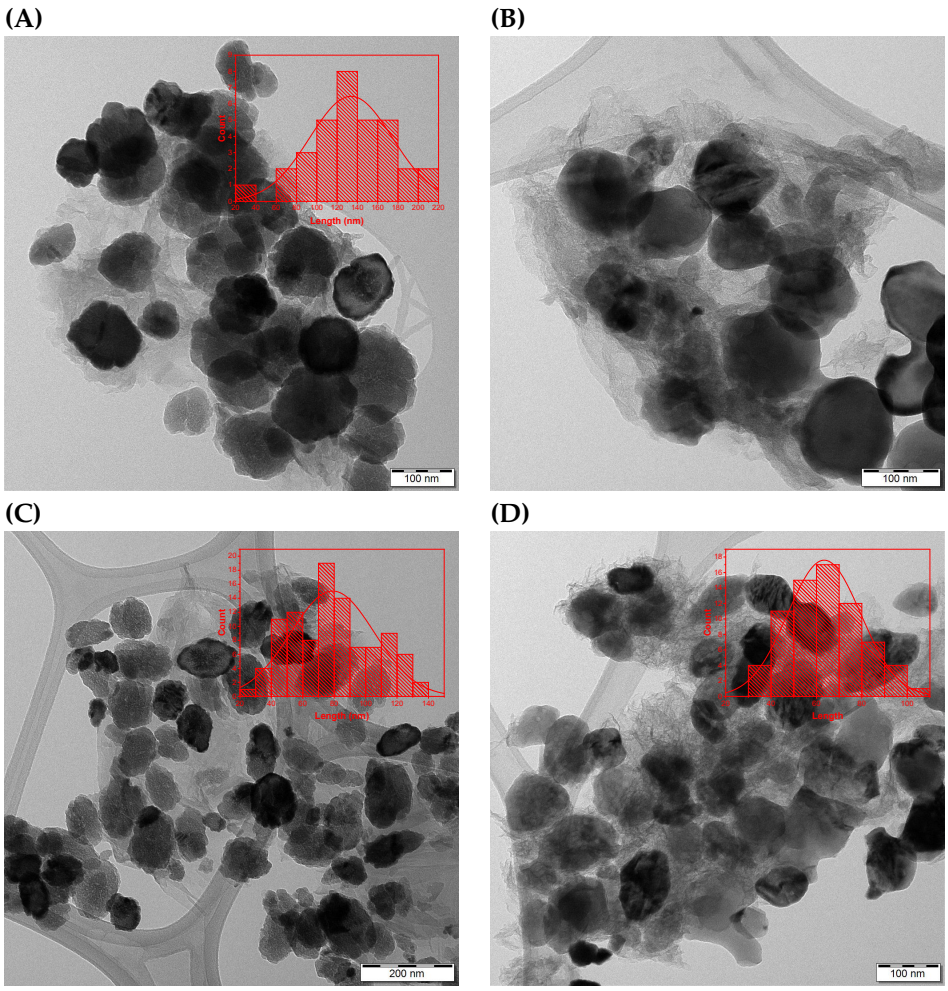

Figure 35 TEM images of GO-iron oxide compounds prepared by hydrothermal method in the presence of JW_GO_H and subsequent thermal reduction with particle size distribution histograms (fitted with normal distribution curve): **(A)** JW_FeA_H, **(B)** JW_FeA_H_N, **(C)** JW_FeA_H2, **(D)** JW_FeA_H2_N.

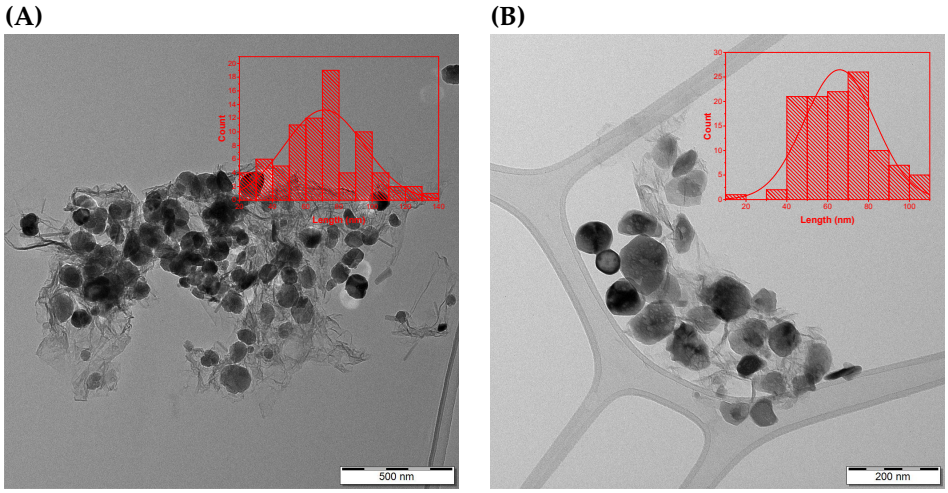

Figure 36 TEM images of GO-iron oxide compounds prepared by hydrothermal method in the presence of JW_GO_T and subsequent thermal reduction with particle size distribution histograms (fitted with normal distribution curve): **(A)** JW_FeA_T, **(B)** JW_FeA_T_N.

Sample	**TEM** (nm)	**Hematite** XRD MCL(nm)	**Magnetite** XRD MCL(nm)	**Goethite** XRD MCL(nm)
JW_FeA_H	133.75±40.72	64	–	–
JW_FeA_H2	78.98±26.54	46	–	–
JW_FeA_T	71.14±24.16	50	–	17
JW_FeA_H_N	–	39	63	–
JW_FeA_H2_N	63.40±16.11	–	40	–
JW_FeA_T_N	65.84±17.33	51	64	–

Table 6 Size of iron oxide nanoparticles prepared by hydrothermal method determined by TEM (particle size histogram were fitted with normal distribution curve) and XRD (MCL).

The Raman spectroscopy was carried out using 633 nm diode laser and 50× objective in the front of the sample with excitation power kept on 0.5 mW for all samples. The low energy region of Raman spectra of non-thermally treated samples (Fig. 37A, Fig. 37C, and Fig. 37E) revealed the presence of hematite vibration modes (A_{1g} at ∼229 cm^{-1} and ∼500 cm^{-1}, E_g at ∼295 cm^{-1}, ∼414 cm^{-1}, and ∼615 cm^{-1}, and LO E_u at ∼660 cm^{-1}) [67]. However, not all vibration modes of hematite are clearly visible due to the small particle size of iron oxide nanoparticles. The Raman spectra obtained after the thermal treatment under nitrogen atmosphere (Fig. 37B, Fig. 37D, and Fig. 37F) show different pattern in low energy region with one major asymmetric peak (670 cm^{-1}), which is typical for A_{1g} vibration mode of nanoscale magnetite [67]. T_{1g} vibration modes of magnetite (300 cm^{-1} and 550 cm^{-1}) display very low intensity and they cannot be distinguished from the noise of measured spectra.

The FT-IR spectra of all samples from this section (Fig. 37G and Fig. 37H) are shown after baseline correction and smoothing using Savitzky-Golay method (25 points) by Origin 2016 software. However, the material was hard to disperse, thus not fully suitable for ATR FT-IR measurements using ZnSe crystal. All FT-IR spectra were normalized from 0 to 100 with respect to C=C band (1620 cm^{-1}), which possesses the highest relative transmittance intensity. The region from 1280 to 1000 cm^{-1} contains the typical C-O/C-OH bands. The decrease of intensity of O-H band (3280 cm^{-1}) and C=O band (1720 cm^{-1}) demonstrates the reduction of oxygen-containing groups after anchoring iron oxide nanoparticles via hydrothermal method and further reduction after thermal treatment under nitrogen atmosphere. It has to be mentioned that some features of the spectra may be generated by the software processing. For complete information, the unprocessed FT-IR spectra are included in Appendix C.1.

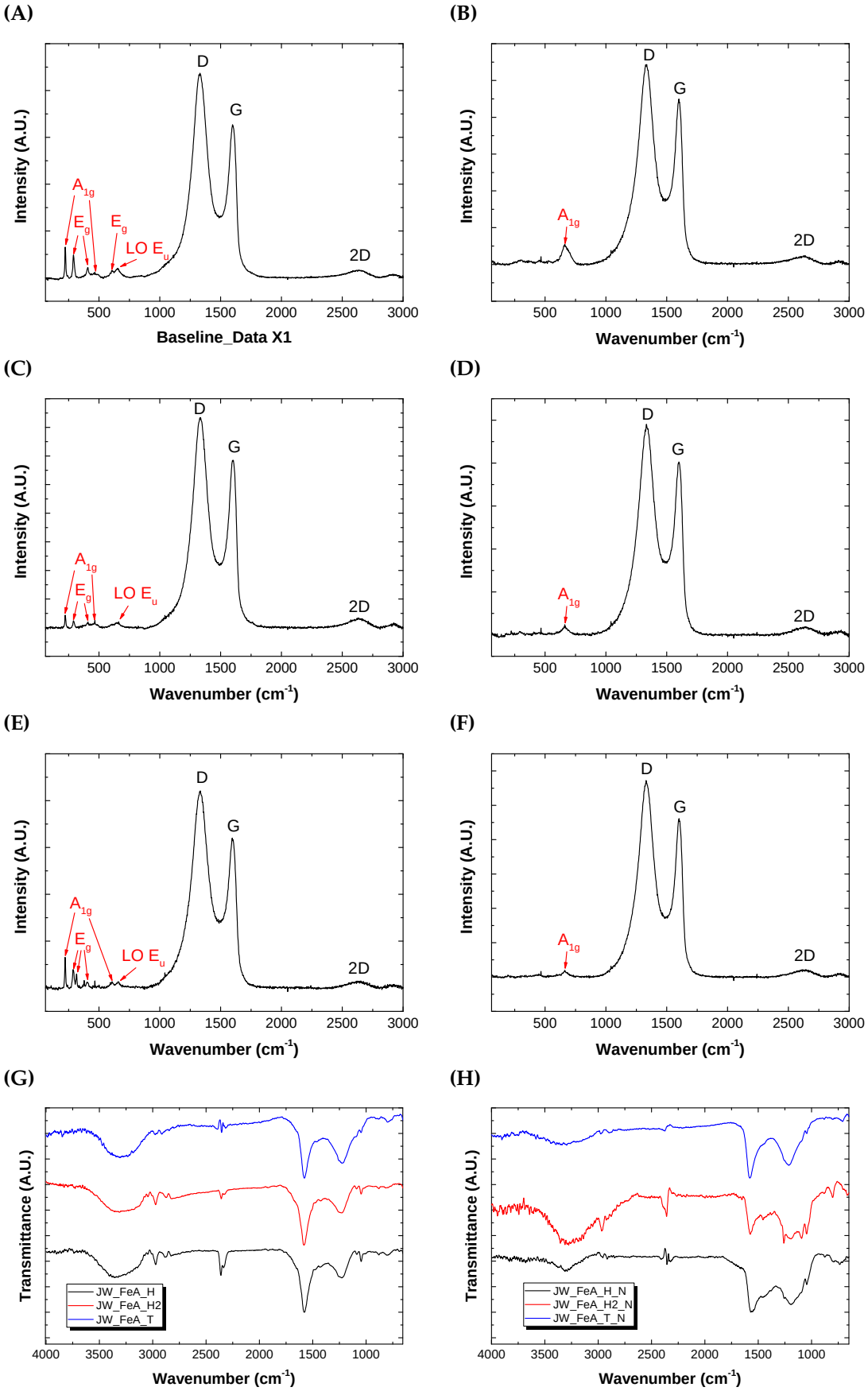

Figure 37 Raman spectra of composites prepared by hydrothermal method. The vibration modes of iron oxides are highlighted by red arrows with assigned vibration mode. **(A)** JW_FeA_H, **(B)** JW_FeA_H_N, **(C)** JW_FeA_H2, and **(D)** JW_FeA_H2_N, **(E)** JW_FeA_T, **(F)** JW_FeA_T_N. FT-IR of GO-iron oxide compounds made by hydrothermal method: **(G)** before thermal treatment, **(H)** after thermal treatment.

The XPS elemental surveys show the presence of carbon, oxygen, nitrogen, and iron (the amount of each element can be found in Fig. 38 for each sample). The amount of iron is higher in the case of non-reduced samples. The nitrogen in all samples probably derives from ammonia solution, which was used during the hydrothermal process and from the nitrogen atmosphere, in which the thermal reduction took place. The high resolution XPS spectra of C1s (Fig. 39A-F) and O1s (Fig. 40) peak exhibit similar features to those of the previous section (**JW_Fe_GO_H** and **JW_Fe_GO_T** Fig. 32E–H). Due to the absence of Fe-C bond in C1s peak (283.3 eV) and Fe2p peak (707.5 eV), we assume that bonding is provided through Fe-OC bonds (∼531.2 eV) observed in O1s peak. The high resolution XPS spectra of Fe2p peaks (Fig. 39G and Fig. 39H) display two major peaks at 711.09 eV ($Fe2p_{3/2}$) and 724.29 eV ($Fe2p_{1/2}$). The satellite feature is not distinguishable, thus oxidation states cannot be determined via XPS.

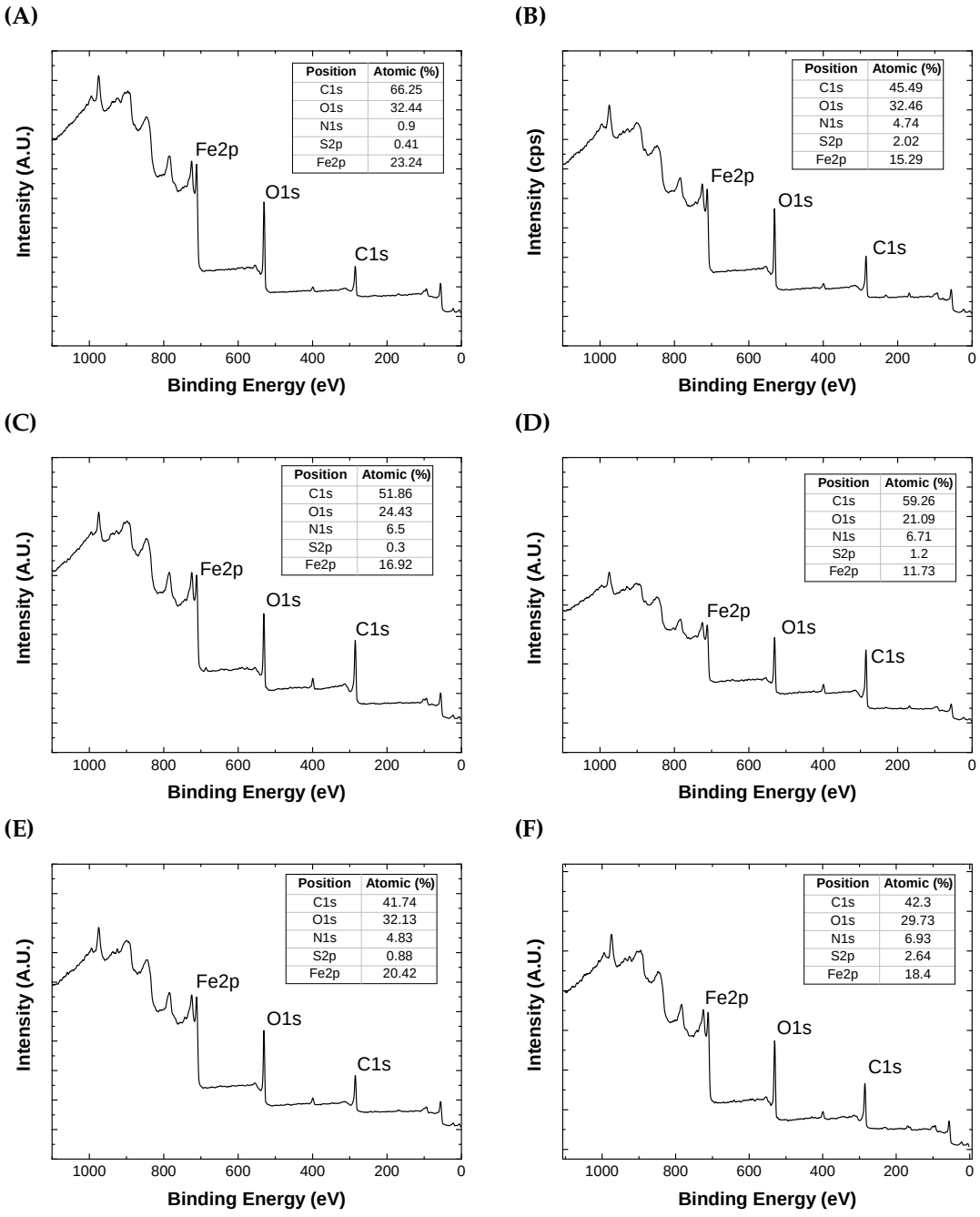

Figure 38 XPS elemental surveys of composited prepared by hydrothermal method: **(A)** JW_FeA_H, **(B)** JW_FeA_H_N, **(C)** JW_FeA_H2, **(D)** JW_FeA_H2_N, **(E)** JW_FeA_T, and **(F)** JW_FeA_T_N.

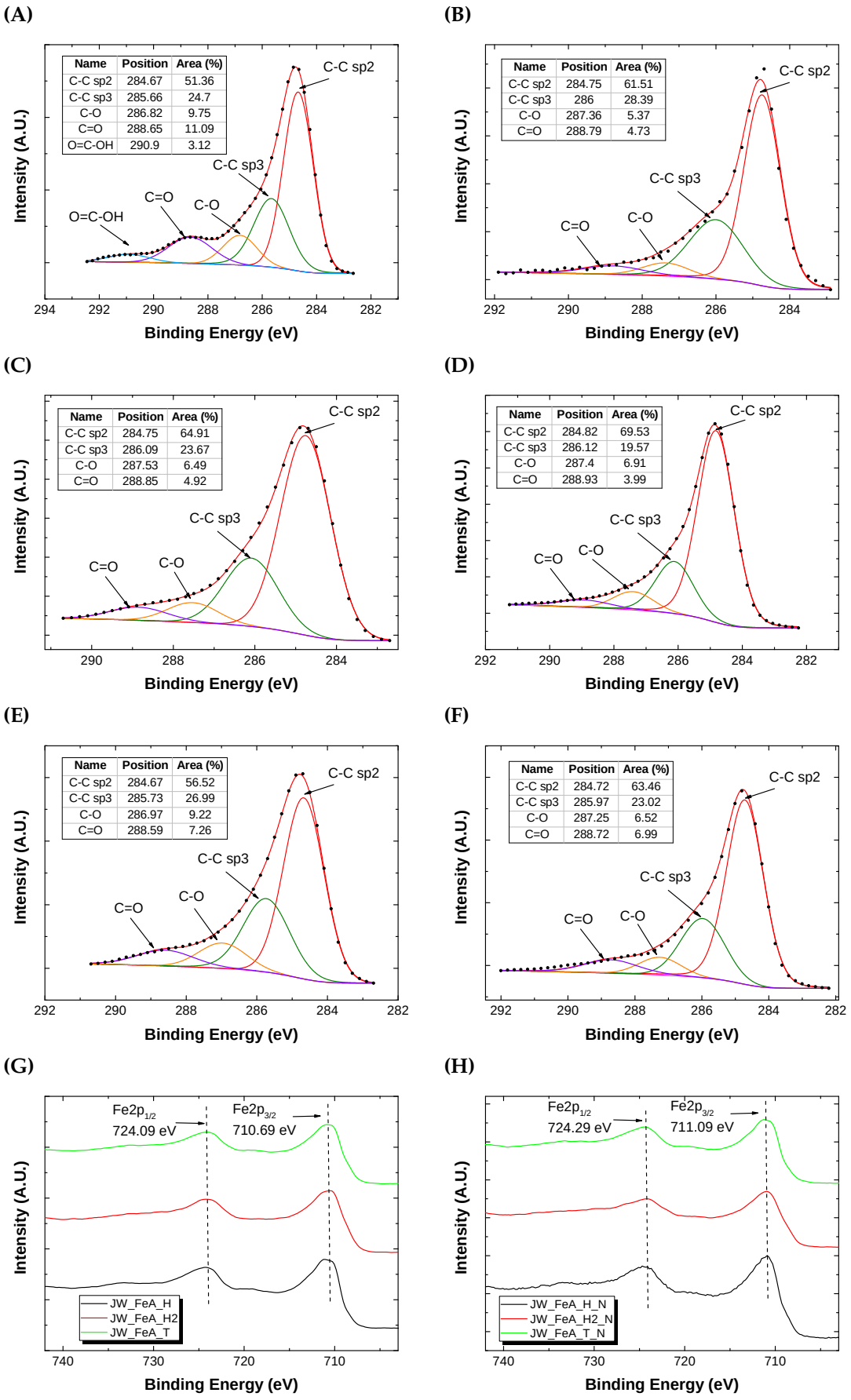

Figure 39 C1s and Fe2p peaks of high resolution XPS spectra of composited prepared by hydrothermal method: **(A)** JW_FeA_H C1s, **(B)** JW_FeA_H_N C1s, **(C)** JW_FeA_H2 C1s, **(D)** JW_FeA_H2_N C1s, **(E)** JW_FeA_T C1s, **(F)** JW_FeA_T_N C1s, **(G)** samples without thermal treatment Fe2p, **(G)** samples with thermal treatment Fe2p.[50]

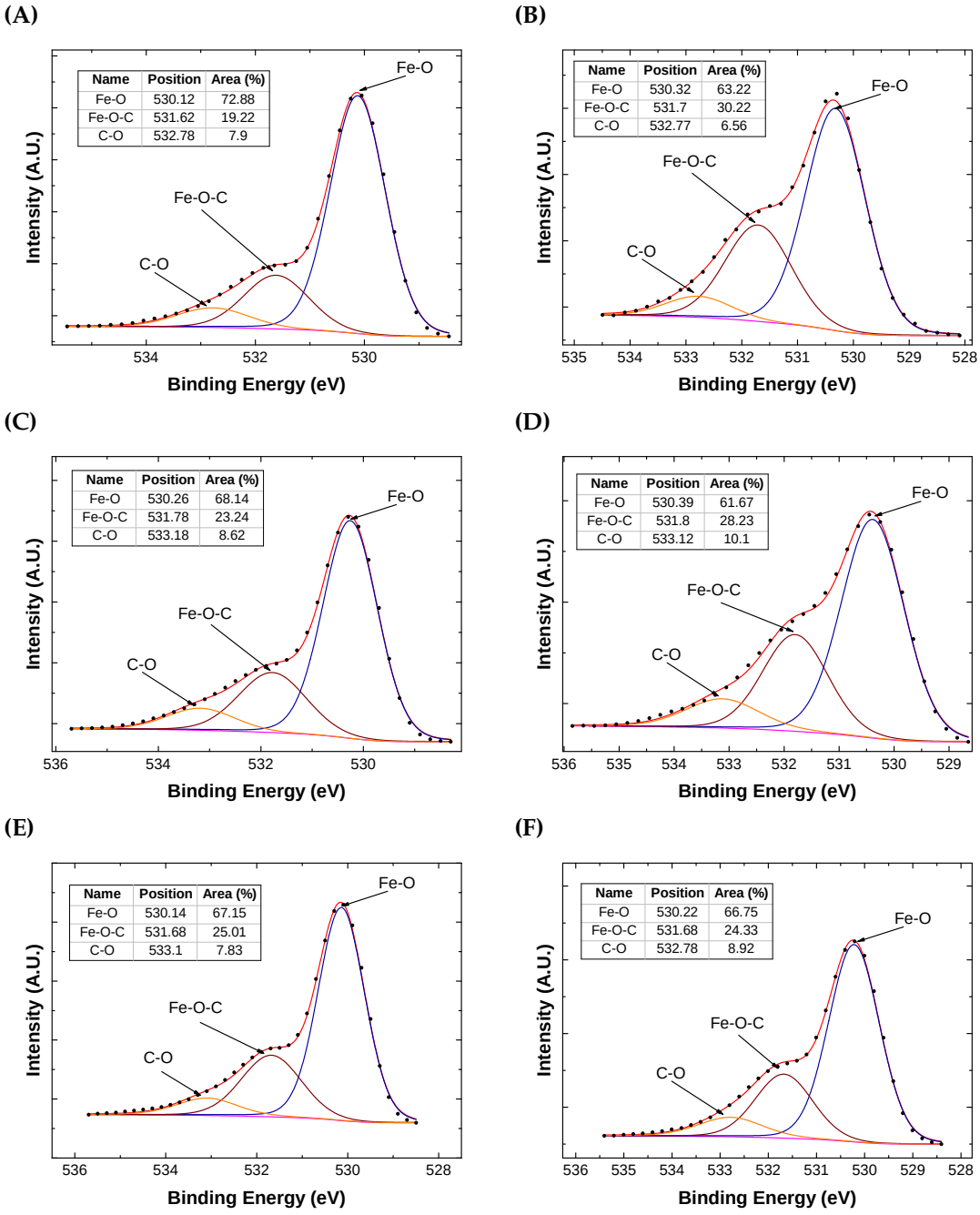

Figure 40 O1s peak of high resolution XPS spectra of composited prepared by hydrothermal method: **(A)** JW_FeA_H, **(B)** JW_FeA_H_N, **(C)** JW_FeA_H2, **(D)** JW_FeA_H2_N, **(E)** JW_FeA_T, **(F)** JW_FeA_T_N.

The structural and morphological properties of the iron oxide part of the compounds were obtained from XRD patterns analysed by Rietveld method (Fig. 41, fit in Appendix B.2). **JW_FeA_H** and **JW_FeA_H2** display 100% of hematite, whereas **JW_FeA_T** shows 96% of hematite and 4% traces of goethite. Samples thermally treated at 500 °C under nitrogen show phase transformation from hematite to magnetite. The amount of magnetite was determined as 97%, 100%, and 36% for **JW_FeA_H_N** (a =8.393 Å, MCL=63 nm), **JW_FeA_H2_N** (a =3.889 Å, MCL=40 nm), and **JW_FeA_T_N** (a =8.394 Å, MCL=64 nm), respectively. Hematite can be reduced by carbon at elevated temperatures in the presence of gases, such as nitrogen, hydrogen or CO/CO_2 mixture [38]. The conversion rate of hematite to magnetite transformation increases with rising temperature, amount of carbon present during the reaction, and is higher in case of smaller hematite

particles [91]. The reduction mechanism can take place as follows [92]:

$$3Fe_2O_3 + CO \rightarrow 2Fe_3O_4 + CO_2 \tag{9}$$

A CO was probably formed from the functional groups of GO with rising temperature under nitrogen. **JW_FeA_H2** possesses the highest conversion rate to magnetite, followed by **JW_FeA_H** and **JW_FeA_T**. **JW_FeA_H2** display the lowest amount of residual mass at the end of TGA measurement, implying the correlation between GO/iron oxide ratio and the rate of hematite-to-magnetite conversion (residual masses from the lowest to the highest: H2: 58.81%, H: 69.28%, T: 76.13%, see next paragraph)

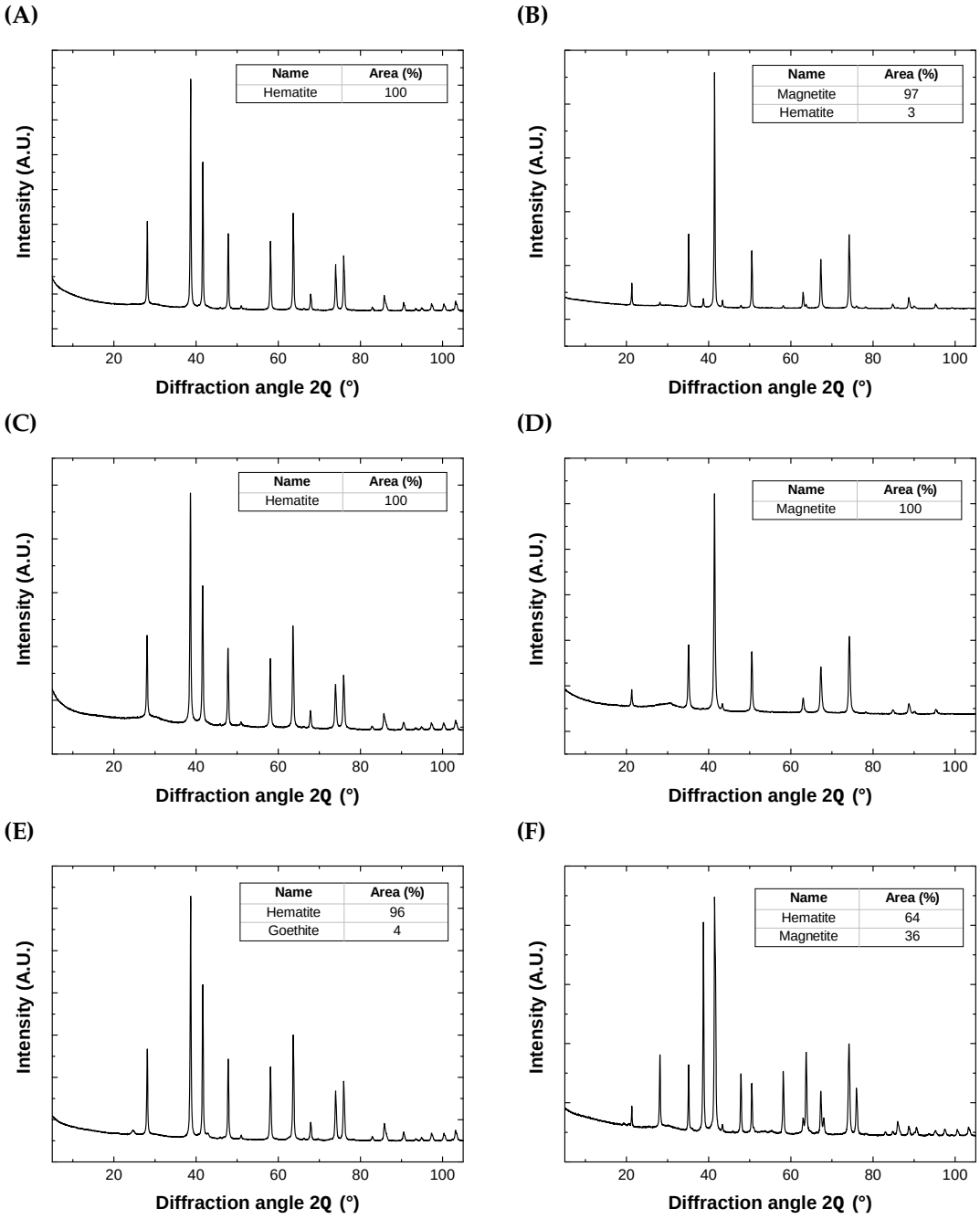

Figure 41 XRD patterns of GO-iron oxide composites made by hydrothermal method. Samples without thermal treatment: **(A)** JW_FeA_H, **(C)** JW_FeA_H2, and **(E)** JW_FeA_T. Samples after thermal treatment: **(B)** JW_FeA_H_N, **(D)** JW_FeA_H2_N, and **(F)** JW_FeA_T_N.

The STA-MS measurements were carried out in the temperature range from 40 to 1000 °C (heating rate 10 K min^{-1}) under synthetic air (flow rate 70 mL min^{-1}) with N_2 used as a protective gas (flow rate 10 mL min^{-1}). All samples were measured in Al_2O_3 crucibles. STA-MS of **JW_FeA_H**, **JW_FeA_H2**, and **JW_FeA_T** (Fig. 42) show weight loss from the beginning of the process until ~310 °C, which can be assigned to the evaporation of physisorbed water from the surface (MS detection of m/z=18). The TGA-DSC charts display one major mass loss (details from DSC charts in Table 7) for each non-reduced sample, originating from thermal decomposition of the GO backbone (MS detection of m/z=44). The residual mass at 1000 °C was determined by TGA as 69.28%, 58.81%, and 76.13% for **JW_FeA_H**, **JW_FeA_H2**, and **JW_FeA_T**, respectively.

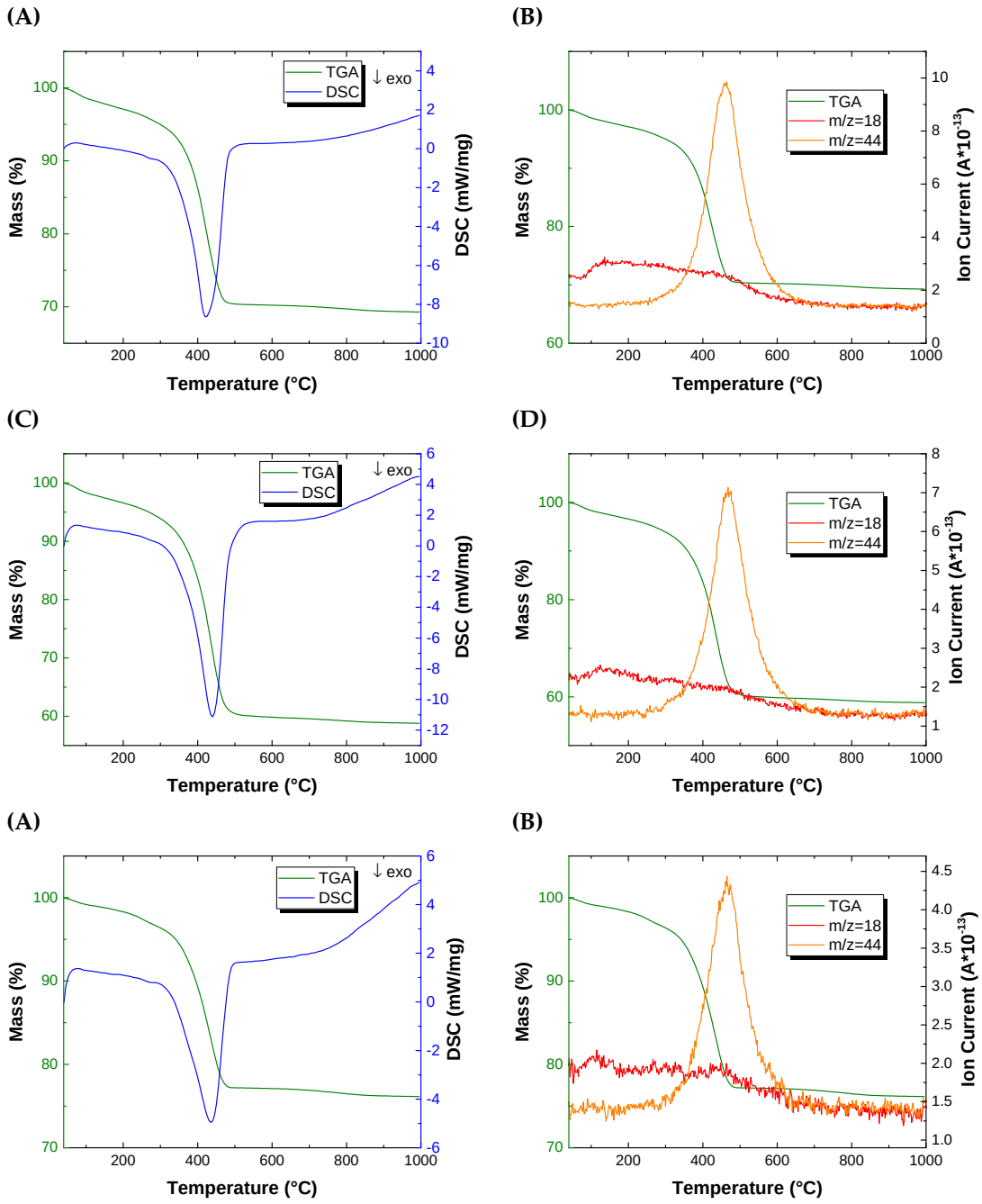

Figure 42 STA-MS of samples prepared by hydrothermal method without thermal treatment: **(A)** JW_FeA_H TGA-DSC, **(B)** JW_FeA_H TGA-MS, **(C)** JW_FeA_H2 TGA-DSC, **(D)** JW_FeA_H2 TGA-MS, **(E)** JW_FeA_T TGA-DSC, **(F)** JW_FeA_T TGA-MS.

STA analysis of **JW_FeA_H_N**, **JW_FeA_H2_N**, and **JW_FeA_T_N** (Fig. 43 and Fig. 44) was performed under the same conditions as **JW_FeA_H**, **JW_FeA_H2**, and **JW_FeA_T**. The MS of **JW_FeA_H2_N** is not available. An initial mass loss (from 40 to 160 °C) is detected in all cases, which could attributed to the loss of physisorbed water (MS detection of m/z = 18 in case of **JW_FeA_H_N** and **JW_FeA_T_N**). The mass gain from approximately 160 to 360 °C can be identified as oxidation of Fe_3O_4 to Fe_2O_3 described with the following formula [93]:

$$4Fe_3O_4 + O_2 \rightarrow 6Fe_2O_3. \tag{10}$$

The reaction show the mass increase of 3.3% in the ideal case of 100% conversion of Fe_3O_4 to Fe_2O_3. The mass gain detected was as 1.80%, 0.56%, and 1.11% for **JW_FeA_H_N**, **JW_FeA_H2_N**, and **JW_FeA_T_N**, respectively. A major mass loss then occurs from ∼390 to ∼600 °C (parameters obtained from DSC charts can be found in Table 7). **JW_FeA_T_N** possesses the highest residual mass at the end of the process (1000 °C), followed by **JW_FeA_T_N** (79.93%) and **JW_FeA_H2_N** (62.26%).

Sample	Onset (°C)	End (°C)	Enthalpy ($J\,g^{-1}$)	Residual mass (1000°C) (%)	Mass gain (160–360°C) (%)
JW_FeA_H	368.3	479.0	-4333	69.28	–
JW_FeA_H2	384.3	482.1	-5609	58.81	–
JW_FeA_T	336.0	483.6	-3383	76.13	–
JW_FeA_H_N	402.5	544.7	-2772	83.34	1.80
JW_FeA_H2_N	379.2	537.0	-6731	62.26	0.56
JW_FeA_T_N	427.8	491.5	-2475	79.93	1.11

Table 7 Parameters of DSC measurements, residual mass at 1000 °C, and mass gain (160–360 °C) of GO-iron oxide composites made by hydrothermal method.

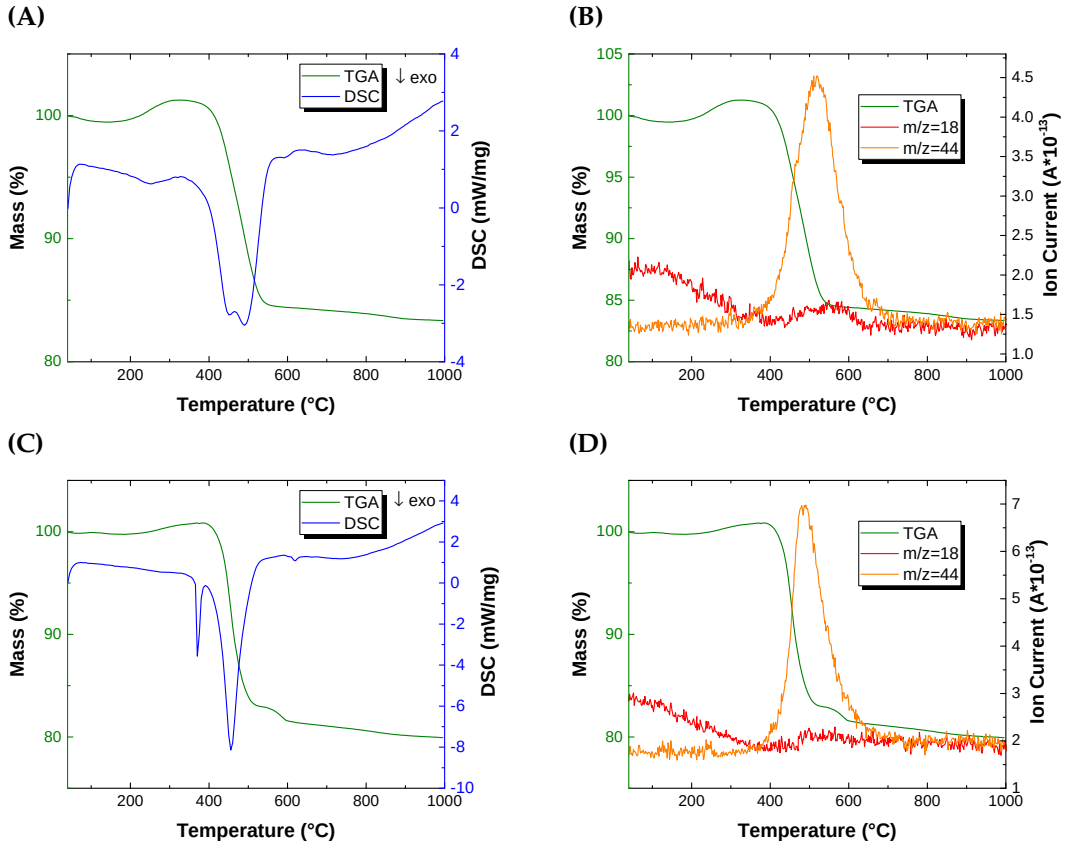

Figure 43 STA-MS of samples prepared by hydrothermal method with subsequent thermal treatment: **(A)** JW_FeA_H_N TGA-DSC, **(B)** JW_FeA_H_N TGA-MS, **(C)** JW_FeA_T_N TGA-DSC, **(D)** JW_FeA_T_N TGA-MS.

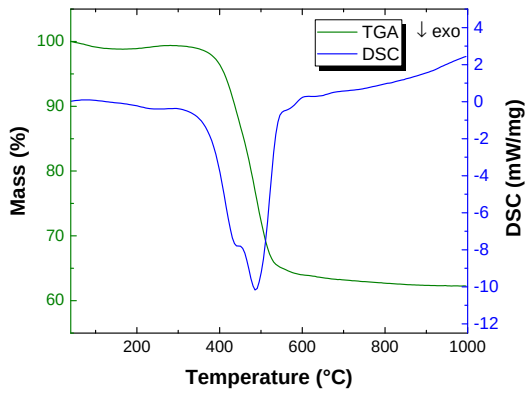

Figure 44 | STA of JW_FeA_H2_N.

The chemical states of iron involved in GO-iron oxide compounds were investigated by the room temperature ^{57}Fe zero-field Mössbauer spectroscopy (Fig 45). All spectral components were determined with respect to hyperfine parameters of hematite sextet, Fe^{3+} superparamagnetic doublet, and octahedral sites (O-sites) and tetrahedral sites (T-sites) sextets of magnetite [38] (Table 8). The Mössbauer spectra of **JW_FeA_H** and **JW_FeA_H2** exhibit one sextet assigned to hematite. **JW_FeA_T** shows 97% of hematite sextet and 3% traces of doublet assigned to Fe^{3+} nanoparticles in superparamagnetic state. Mössbauer spectra of all thermally treated samples contain magnetite sextets. The magnetite is stoichiometric, if Mössbauer spectrum shows a 1:2 ratio between tetrahedral and octahedral sites occupancy [94]. **JW_FeA_H_N** consists of 94% of non-stoichiometric magnetite (tetrahedral/octahedral occupancy ratio of 1:0.98) and 6% of hematite traces. The iron oxide part of **JW_FeA_H2_N** is formed by 100% of non-stoichiometric magnetite (tetrahedral/octahedral occupancy ratio of 1:0.92). **JW_FeA_T_N** contains 56% of hematite, 35% of nearly stoichiometric magnetite (tetrahedral/octahedral occupancy ratio of 1:1.83), and 7.3% traces of Fe^{3+} doublet, which could be caused by surface layers of maghemite nanoparticles.

Sample Component	**Isomer shift** δ (mm s^{-1})	**Quadrupole splitting** δE_Q (mm s^{-1})	**Hyperfine mag. field** B_{hf} (T)	**Spectral area** (%)
JW_FeA_H				
Hematite	0.37	-0.22	50.52	100
JW_FeA_H2				
Hematite	0.37	-0.22	50.09	100
JW_FeA_T				
Hematite	0.37	-0.21	50.49	97.0
Fe^{3+} doublet	0.30	0.69	–	3.0
JW_FeA_H_N				
T-sites, Fe_3O_4	0.30	0.01	48.93	47.5
O-sites, Fe_3O_4	0.66	0.01	45.45	46.6
Hematite	0.35	-0.21	51.30	6.0
JW_FeA_H2_N				
T-sites, Fe_3O_4	0.30	-0.02	48.79	52.0
O-sites, Fe_3O_4	0.63	0.02	45.26	48.0
JW_FeA_T_N				
Hematite	0.37	-0.21	50.66	56.5
T-sites, Fe_3O_4	0.25	0.00	48.23	12.8
O-sites, Fe_3O_4	0.65	0.00	45.49	23.5
Fe^{3+} doublet	0.21	0.61	–	7.3

Table 8 | The hyperfine parameters of the room temperature ^{57}Fe zero-field Mössbauer spectra of GO-iron oxide hybrids prepared by hydrothermal method.

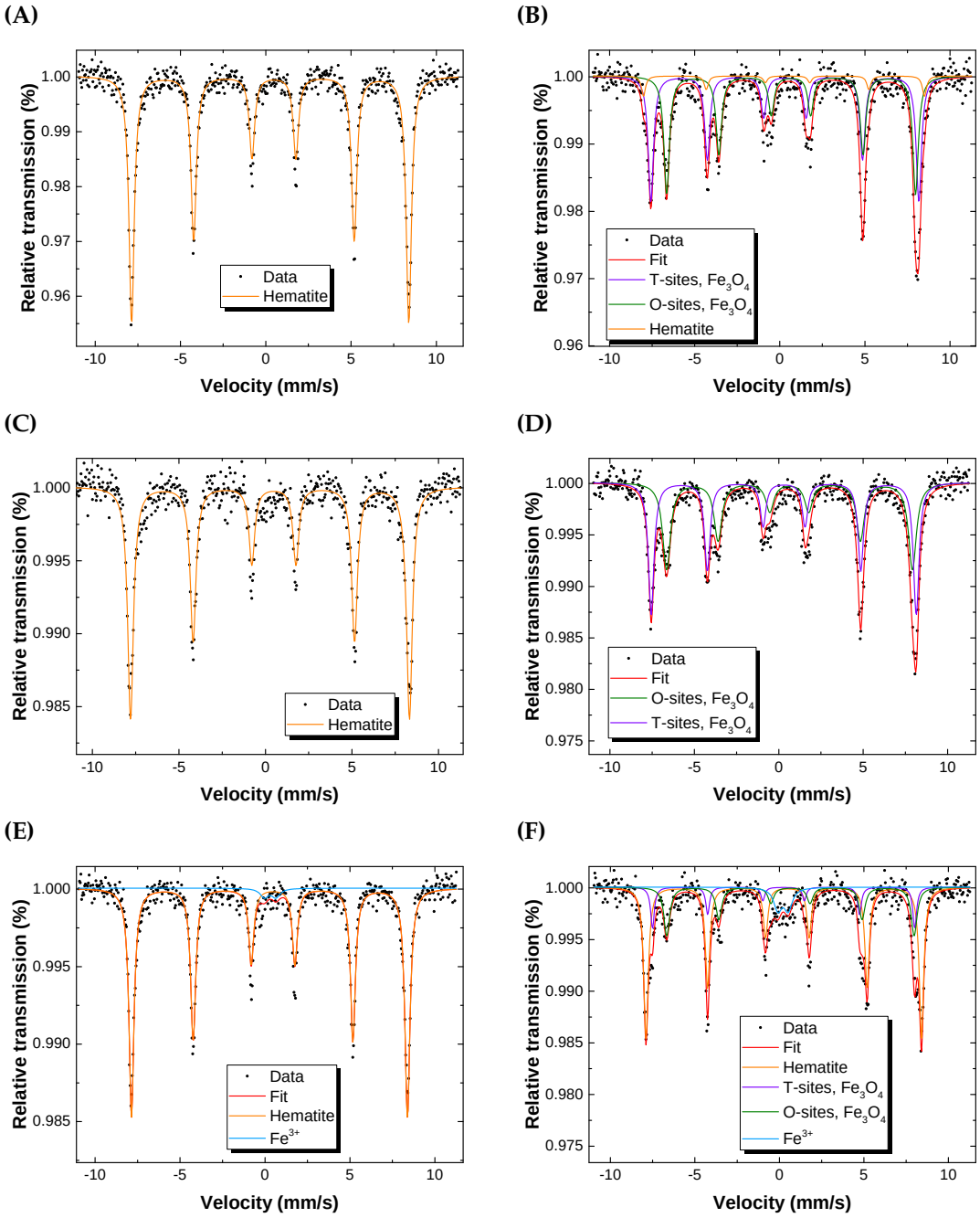

Figure 45 The room temperature ^{57}Fe zero-field Mössbauer spectra of **(A)** JW_FeA_H, **(B)** JW_FeA_H_N, **(C)** JW_FeA_H2, and **(D)** JW_FeA_H2_N, **(E)** JW_FeA_T, **(F)** JW_FeA_T_N.

In conclusion, GO-iron oxide composites prepared by hydrothermal method without further treatment contain mostly hematite nanoparticles. The hematite phase was confirmed by Raman spectroscopy, XRD, and room temperature ^{57}Fe zero-field Mössbauer spectroscopy. **JW_FeA_T** possesses the highest functionalization of hematite nanoparticles determined from residual mass of 76.93% provided by STA-MS measurement. The subsequent thermal treatment under nitrogen triggered the phase transformation of hematite to magnetite confirmed by the observation of magnetite vibration mode in Raman spectra, XRD, STA-MS detection of mass gain, and Mössbauer spectroscopy. The transformation rate from hematite to magnetite was found to be dependent on the amount of carbon present during the thermal treatment. **JW_FeA_H_N** and **JW_FeA_H2_N** show higher transformation rate between hematite to magnetite (94–97% and 100%, respectively) than **JW_FeA_T_N** (36%). Iron oxides nanoparticles of all samples included in this section are anchored via GOs oxygen-containing groups (Fe-OC bond) as suggested by XPS measurements.

3.4.3. Magnetite and sulphonated graphene oxide hybrid system

The last preparation technique undertaken is divided into three major steps. The first step includes treatment of GO (**JW_GO_H** and **JW_GO_T**) with sulphuric acid in order to introduce sulphonated groups on GO and thus increase an absorption capacity of GO, with the aim to obtain a hybrid composite with denser coverage of iron oxide nanoparticles (sulphonated GO labelled as **JW_SGO_H** and **JW_SGO_T**). The second step is separate synthesis of magnetite nanoparticles by solvothermal method in a Teflon lined stainless steel autoclave with the use of polyethylene glycol polymer (PEG, molar mass M_{PEG}=2000 g mol^{-1}). A heavier PEG was also initially tested (molar mass M_{PEG}=35 000 g mol^{-1}), but the prepared nanoparticles showed no major differences with those obtained using PEG M_{PEG}=2000 g mol^{-1}, so no further study on this heavier PEG was done. According to the literature [58], the amount of sodium hydroxide has a large impact on the size and shape of the synthesised magnetite nanoparticles, ranging from spherical nanoparticles smaller than 100 nm up to multifaceted nanoparticles with diameter higher than 100 nm. In the final step, the sulphonated GO and magnetite nanoparticles are mixed in aqueous environment and sonicated, creating a hybrid compound labelled as **JW_SGO_T_Fe** and **JW_SGO_H_Fe** with respect to starting sulphonated GO. The ratio between sulphonated GO and magnetite nanoparticles was 1.7:1.

Starting material for solvothermal synthesis of Fe_3O_4 nanoparticles:

- Iron (III) chloride hexahydrate ($FeCl_3 \cdot 6H_2O$), Sigma-Aldrich, $m_{FeCl_3 \cdot 6H_2O} = 1.35$ g
- Polyethylene glycol (PEG, Alfa Aesar – molar mass M_{PEG}= 2000 g mol^{-1} and Sigma-Aldrich – molar mass M_{PEG}= 35 000 g mol^{-1}), $m_{\mathrm{PEG}} = 1$ g
- Ethylene glycol (EG), Sigma-Aldrich, $V_{\mathrm{EG}} = 30$ mL
- Sodium hydroxide (NaOH), Lach-Ner, $m_{\mathrm{NaOH}} = 0.4$ g

Starting material for sulphonated GO (JW_SGO_H and JW_SGO_T) :

- GO made by modified Hummers method, **JW_GO_H**, $m_{\mathrm{JW\_GO\_H}} = 100$ mg
- GO made by Tour method, **JW_GO_T**, $m_{\mathrm{JW\_GO\_T}} = 107$ mg
- Sulphuric acid, Lach-Ner 96% concentration, $V_{H_2SO_4} = 35$ mL
- Deionized water, $V_{H_2O} = 100$ mL

Procedure:
Synthesis of magnetite nanoparticle by solvothermal method:

1. 30 mL of EG was vigorously bubbled by nitrogen gas for 20 minutes.
2. $FeCl_3 \cdot 6H_2O$ is dissolved in EG.
3. NaOH and PEG were added into the mixture and stirred for 30 minutes.
4. The suspension was transferred into a Teflon lined stainless steel autoclave and sealed.
5. The Teflon lined stainless steel autoclave was placed into the furnace (200 °C) for 8 hours.
6. The final product was collected from the suspension using an external magnetic field and washed with water and ethanol.
7. Magnetite nanoparticles were dried under vacuum (20–30 mbar).

Preparation of sulphonated GO:

1. GO was added into solution of water (100 mL) and H_2SO_4 (35 mL) at 0 °C (ice bath) to control the heating of the suspension caused by exothermic reaction.

2. The product was washed three times with deionized water via centrifugation (13000 RPM, 10 minutes per cycle). At pH higher than ~3, separation of the solid part by centrifugation was hard to achieve, thus the water part was removed at low pH.
3. The final product was washed three times with diethyl ether via centrifugation (13000 RPM, 10 minutes per cycle).
4. The sulphonated GO was dried under vacuum (15 mbar) for two days.

Preparation of sulphonated GO-magnetite nanoparticle composite:

1. Sulphonated GO was dispersed in deionized water and sonicated for 1 hour.
2. Magnetite nanoparticles were added into above suspension and stirred for 30 minutes.
3. The mixture was sonicated for 2 hours to achieve a homogeneous suspension.
4. The final product was washed several times with deionized water and ethanol using external magnetic field to separate unfunctionalized GO from the hybrid.
5. The GO-magnetite composite was dried under vacuum (20–30 mbar).

The particle size distribution was determined from TEM images by ImageJ software from approximately 200–300 nanoparticles and fitted with lognormal distribution (Fig. 46). A relatively uniform coverage of iron oxide nanoparticles is visible (size distribution with standard deviation obtained from lognormal fit can be found in Table 9). The EDS analysis (Appendix A.5) revealed the presence of iron and oxygen. The carbon coated copper grid, which was used as sample holder for the measurement attributed to copper and carbon detection.

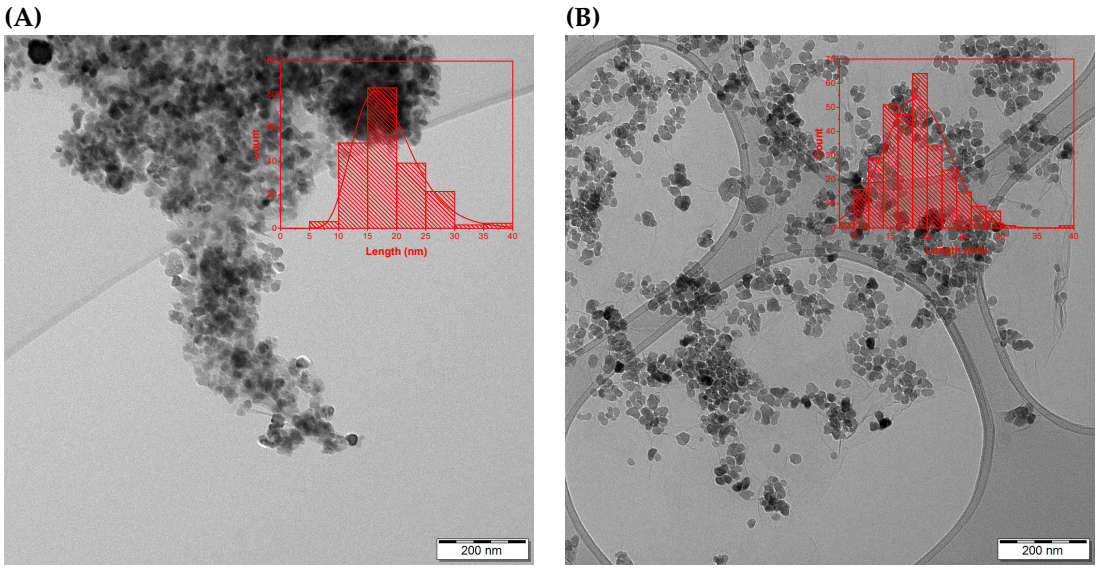

Figure 46 TEM images of sulphonated GO-magnetite composites: **(A)** JW_SGO_T_Fe and **(B)** JW_SGO_H_Fe.

Sample	TEM (nm)	Magnetite XRD MCL(nm)	Fougerite XRD MCL(nm)
JW_SGO_T_Fe	18.63±5.45	20	8
JW_SGO_H_Fe	18.44±4.47	–	–

Table 9 Size distribution of sulphonated GO-magnetite composites determined by TEM (histograms were fitted with lognormal distribution) and MCL of JW_SGO_T_Fe determined by XRD.

The FT-IR spectra of all samples presented in this section have corrected baseline and were smoothed by Savitzky-Golay method (25 points) in Origin 2016 software (Fig. 47A and Fig. 47B). All FT-IR spectra were normalized with respect to O-H (∼3408 cm^{-1}) band. The relative transmission intensity of O-H band (∼3408 cm^{-1}), C=O band (1720 cm^{-1}), and C-O bands region (1420–850 cm^{-1}) is lower in the case of sulphonated GO and GO-magnetite composite.

The Raman spectrum of **JW_SGO_T_Fe** (Fig. 47C) was obtained using 633 nm diode laser (excitation power 0.5 mW) with 50× objective in the front of the sample. The main GO bands (D 1333.2 cm^{-1}, G 1598.4 cm^{-1}, and 2D 2654.2 cm^{-1}) are clearly visible. The I_D/I_G ratio was calculated as 1.15. However, the presence of magnetite cannot be confirmed by Raman spectroscopy in this case due to the low signal of the low energy region, which could be caused by small size of magnetite nanoparticles.

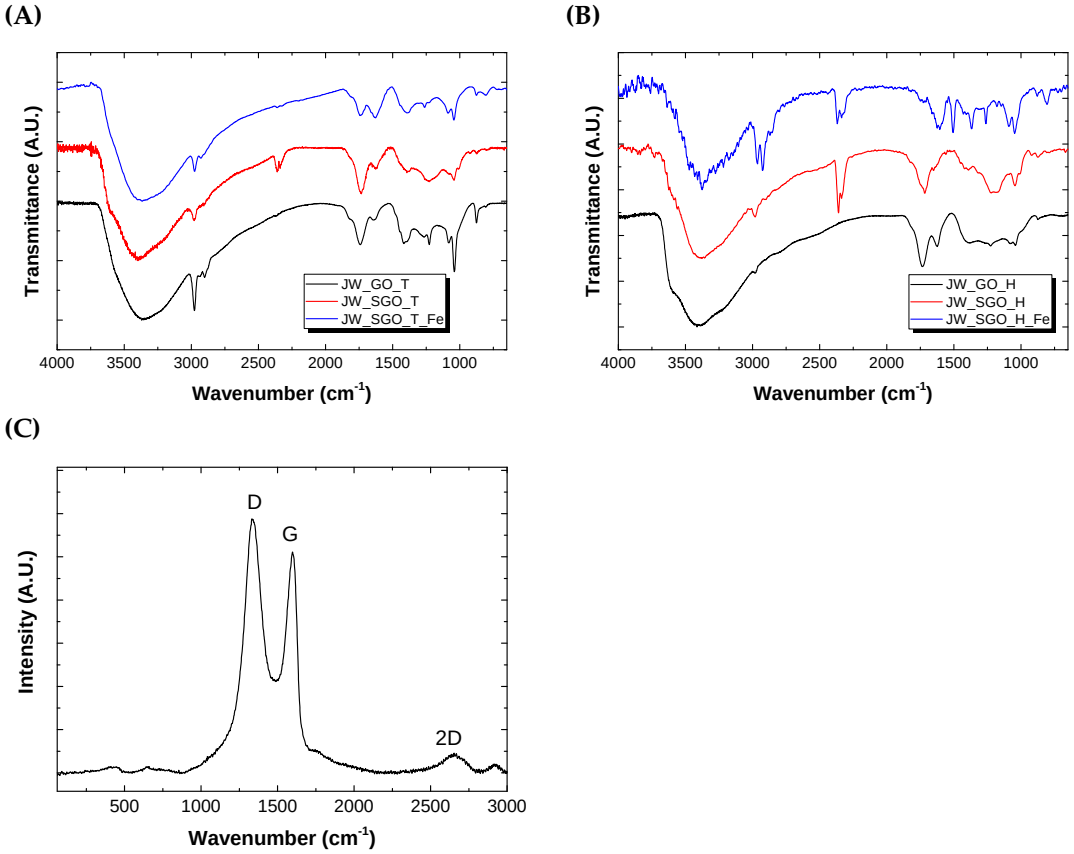

Figure 47 FI-IR spectra normalized with respect to O-H band: **(A)** materials based on JW_GO_T, **(B)** materials based on JW_GO_H. **(C)** Raman spectrum of JW_SGO_T_Fe with I_D/I_G=1.15.

Sulphonated GO (**JW_SGO_T**, **JW_SGO_H**) and sulphonated GO-magnetite hybrid composites (**JW_SGO_T_Fe**, and **JW_SGO_H_Fe**) were measured by XPS to investigate the elemental composition and the chemical states of the samples. The XPS elemental survey of **JW_SGO_T** and **JW_SGO_H** (Fig. 48A and Fig. 48B) revealed the following elements: carbon (T: 59.86%, H: 46.13%), oxygen (T: 32.3%, H: 41.38%), nitrogen (T: 1.92%, H: 4.54%), and sulphur (T: 5.92%, H: 7.95%). The relatively high amount of sulphur compared to pristine GO suggests successful incorporation of sulphur into material. The high resolution XPS spectra of C1s peak of both sulphonated GOs (Fig. 48C and Fig. 48D) display higher amount of sp^2 carbon (C-C sp^2 at 284.6 eV) than pristine GO. The relative intensities of deconvoluted peaks of sp^3 carbon (∼285.4 eV) and C=O (∼288.4 eV) are lower compared to pristine GO. The deconvoluted peak at 286.8 eV can be assigned to C-O (286.9 eV) or C-S (286.5 eV) bonds. Considering the high decrease of intensity of C-O bond (∼532.6 eV) in the high resolution XPS spectra of O1s peak (Fig. 48E and Fig. 48F), the 286.8 eV peak could be caused mainly by C-S bond [95]. The other components of O1s peak of high

resolution XPS spectra (C=O ∼531.5 eV and O=C-OH ∼533.63 eV) possess higher relative intensity than C-O peak than in the case of pristine GO. The deconvolution of high resolution XPS spectra of S2p peak (Fig. 49A and Fig. 49B) reveals five components. The peaks at ∼168.6 eV, ∼169.6 eV, and ∼170.5 eV can be assigned to the sulphur-containing groups, such as C- SO_2, C- SO_3, and C- SO_4, respectively [96][97]. The relatively low intensity of two peaks centered at ∼163.7 eV ($S2p_{3/2}$) and ∼164.9 eV ($S2p_{1/2}$) imply the low amount of -C-S-C- covalent bonds in the GO structure [98]. The information obtained from XPS measurements indicates the successful modification of GO by sulphuric acid.

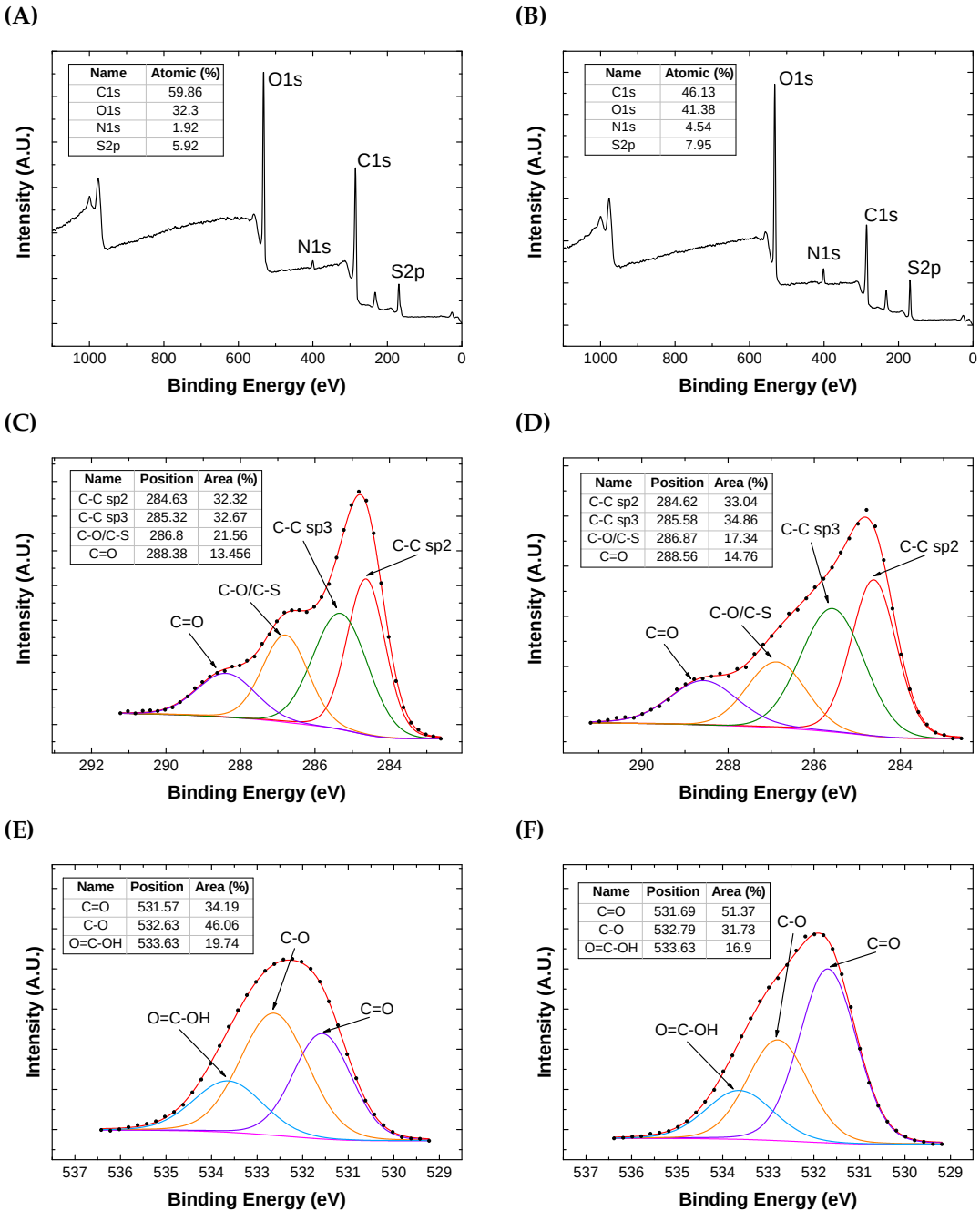

Figure 48 XPS elemental survey and high resolution XPS of C1s and O1s peak of sulphonated GO: **(A)** JW_SGO_T elemental survey, **(B)** JW_SGO_H elemental survey, **(C)** JW_SGO_T C1s, **(D)** JW_SGO_H C1s, **(E)** JW_SGO_T O1s, and **(F)** JW_SGO_H O1s.

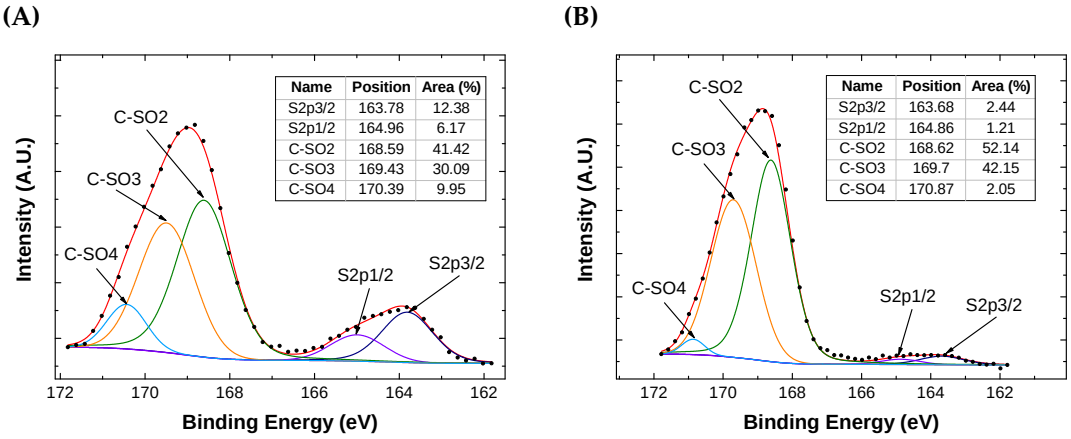

Figure 49 High resolution XPS spectrum of S2p of sulphonated GO: **(A)** JW_SG_T, **(B)** JW_SG_H.

The XPS elemental analysis of **JW_SGO_T_Fe** and **JW_SGO_H_Fe** (Fig. 50A and Fig. 50B) showed carbon, oxygen, sulphur, nitrogen and iron. The amount of sulphur is under 1%. The deconvolution of high resolution XPS spectra of C1s peak (Fig. 51A and Fig. 51B) consist of C-C sp^2 (∼284.5 eV), C-C sp^3 (∼285.2 eV), C-O (∼286.9 eV), and C=O (∼288.4 eV). The ratio between C-C sp^2 and C-C sp^3 carbon is similar to the sulphonated GO, however the relative intensity of C-O bond has increased. The O1s peak of the high resolution XPS spectra (Fig. 51C and Fig. 51D) consists of three peaks at ∼530.2 eV, ∼531.5 eV, and ∼532.7 eV. The first peak at ∼530.2 eV stands for Fe-O bonds within the magnetite crystal lattice. The second peak at ∼531.5 eV can be assigned to Fe-OC or C=O bond. The peak at ∼532.7 eV is identified as C-O bond and has the highest relative intensity among other GO-iron oxide composites presented in this work. The high resolution XPS spectra of Fe2p region (Fig. 51E and Fig. 51F) shows two major peaks at ∼724.5 eV ($Fe2p_{1/2}$) and ∼711 eV ($Fe2p_{3/2}$). The satellite features are not clearly distinguishable for both **JW_SGO_T_Fe** and **JW_SGO_H_Fe**. Fe-C bond was not observed in the expected areas (simultaneous detection in C1s peak at 283.3 eV and in Fe2p peak at 707.5 eV), thus we assume anchoring of magnetite nanoparticles via Fe-O-C bonding.

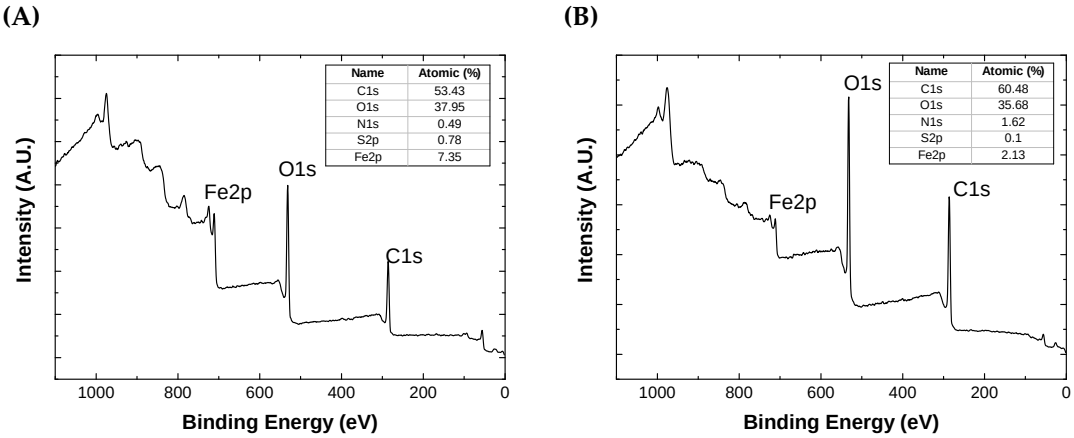

Figure 50 XPS elemental survey of sulphonated GO-magnetite composites: **(A)** JW_SGO_T_Fe and **(B)** JW_SGO_H_Fe.

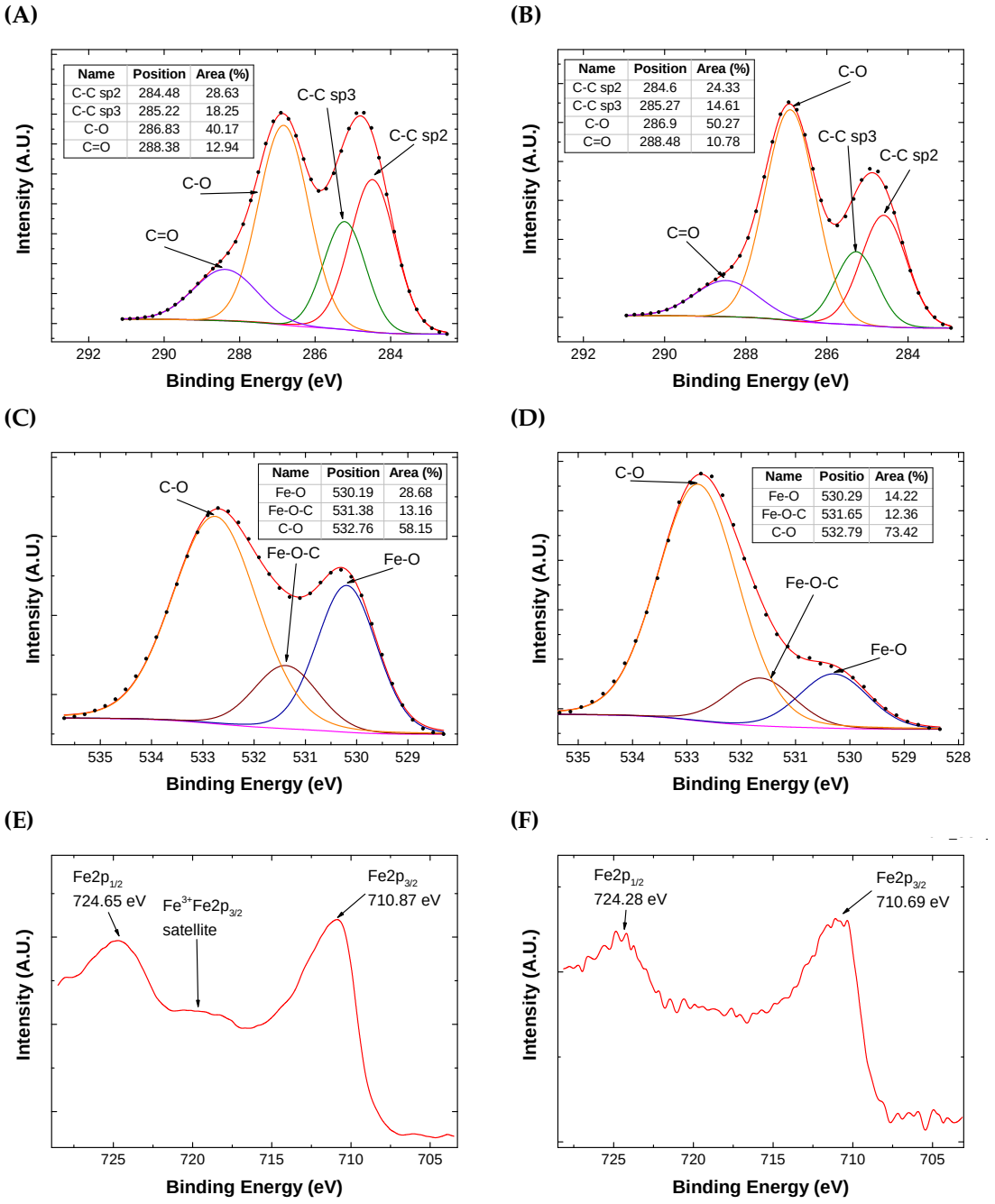

Figure 51 High resolution XPS spectra of sulphonated GO-magnetite composites: **(A)** JW_SGO_T_Fe C1s, **(B)** JW_SGO_H_Fe C1s, **(C)** JW_SGO_T_Fe O1s, **(D)** JW_SGO_H_Fe O1s, **(E)** JW_SGO_T_Fe Fe2p, **(F)** JW_SGO_H_Fe Fe2p.

The STA-MS measurement took place in the temperature range from 40 to 1000 °C with heating rate of 10 K min^{-1} under synthetic air (flow rate 70 mL min^{-1}) and with nitrogen used as a protective gas (flow rate 10 mL min^{-1}). All samples were measured in Al_2O_3 crucible. The MS was set to detect potential m/z ratios of water and gases containing carbon and sulphur, such as 18 (H_2O), 44 (CO_2), 48 (SO), 64 (SO_2), and 80 (SO_3). The DSC chart (Fig. 52A) of **JW_SGO_T** display two major steps, the first with enthalpy of $-636\,\mathrm{J\,g^{-1}}$ (onset 138 °C, end 152 °C) and the second with enthalpy of $-2168\,\mathrm{J\,g^{-1}}$ (onset 560 °C, end 680 °C). One apparently endothermic process from 281 °C to 300 °C is also visible. According to MS measurement (Fig. 52B), the first reaction can be identified as an evaporation of physisorbed water (m/z=18). Then m/z=18, m/z=48, and m/z=64 are detected simultaneously with the endothermic process, attributed to water, SO_2, and SO_3, respectively. The last exothermic step involves combustion of graphitic backbone. The ash content was determined as 0.64%.

The STA-MS chart of **JW_SGO_T_Fe** is shown in Fig. 52C and Fig. 52D. The initial mass loss can be interpreted as an evaporation of physisorbed water (m/z=18 detection in MS) There are two distinguishable exothermic processes on the DSC chart. The first one (onset 194.5 °C, end 241.1 °C, enthalpy $-335\,\mathrm{J\,g^{-1}}$) can be assigned to the evaporation of chemisorbed water and to the partial carbon decomposition (m/z=18 and m/z=44 detection in MS). The combustion of the residual carbon (m/z=44 detection in MS) takes place within the second exothermic reaction (onset 323.6 °C, end 389.8 °C, enthalpy $-2046\,\mathrm{J\,g^{-1}}$). However, the mass gain typical for oxidation of magnetite to Fe_2O_3 was not visible, probably due to the overwhelming mass loss from the early stages. Moreover, the small amount of material indicates for the measurement and the relatively low sulphur content made the detection of sulphur-containing gases unfeasible.

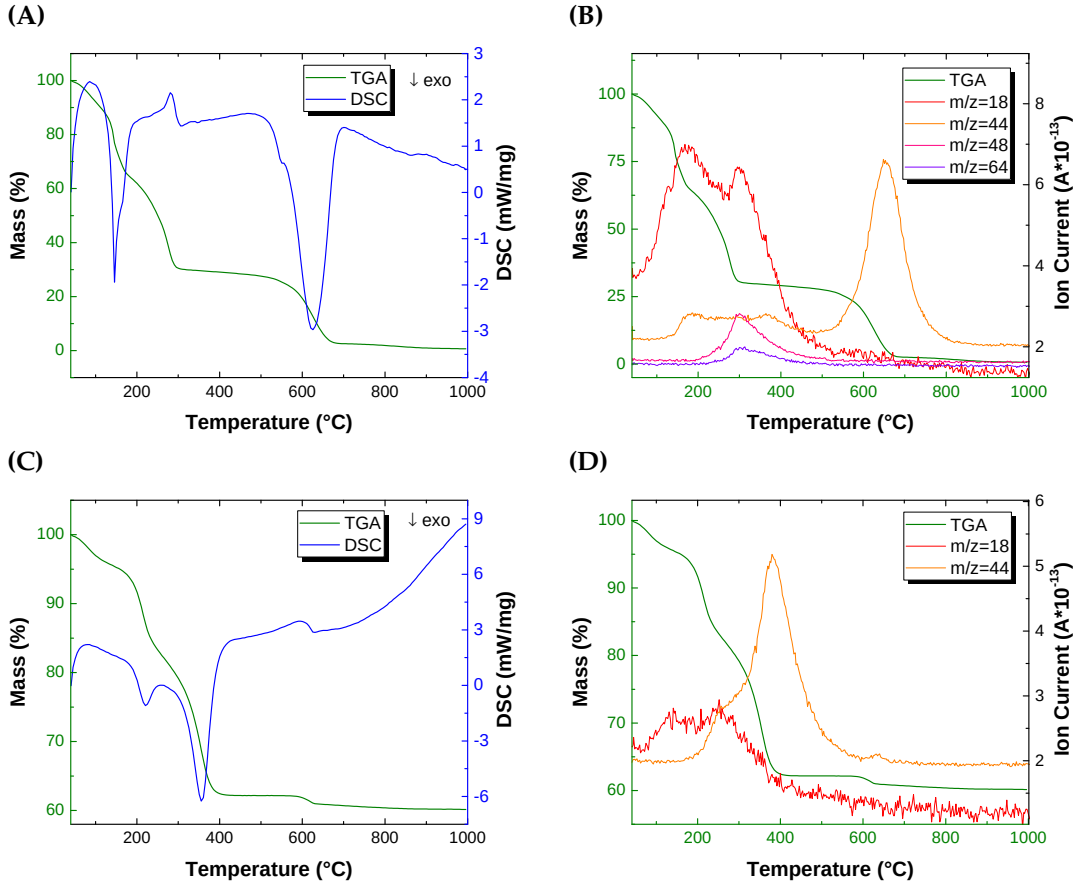

Figure 52 STA-MS measurement in temperature range from 40 to 1000 °C (heating rate 10 K min^{-1}) under synthetic air (flow rate 70 mL min^{-1}) with N_2 used as a protective gas (flow rate 10 mL min^{-1}). **(A)** JW_SGO_T TGA-DSC, **(B)** JW_SGO_T TGA-MS, **(C)** JW_SGO_T_Fe TGA-DSC, and **(D)** JW_SGO_T_Fe TGA-MS.

XRD pattern of **JW_SGO_T_Fe** (Fig. 53A) was analysed by Rietveld method (fit in Appendix B.3). **JW_SGO_T_Fe** possesses 97% of magnetite (a =8.381 Å and MCL=20 nm) and 3% fougerite (MCL=8 nm). The value of lattice parameter and low MCL suggests high non-stoichiometry and possibly oxidated magnetite on the surface. Room temperature ^{57}Fe zero-field Mössbauer spectroscopy was used to investigate the oxidation state of iron involved. The deconvolution of the ^{57}Fe zero-field Mössbauer spectrum (Fig. 53B) with respect to hyperfine parameters (Table 10) revealed the 72.5% of tetrahedral and 27.5% octahedral sites occupancy confirming the presence of highly non-stoichiometric magnetite. Unfortunately, due to poor statistics of the ^{57}Fe Mössbauer spectrum, we were not able to accurately fit the spectrum and hence determine the exact level of non-stoichiometry of magnetite.

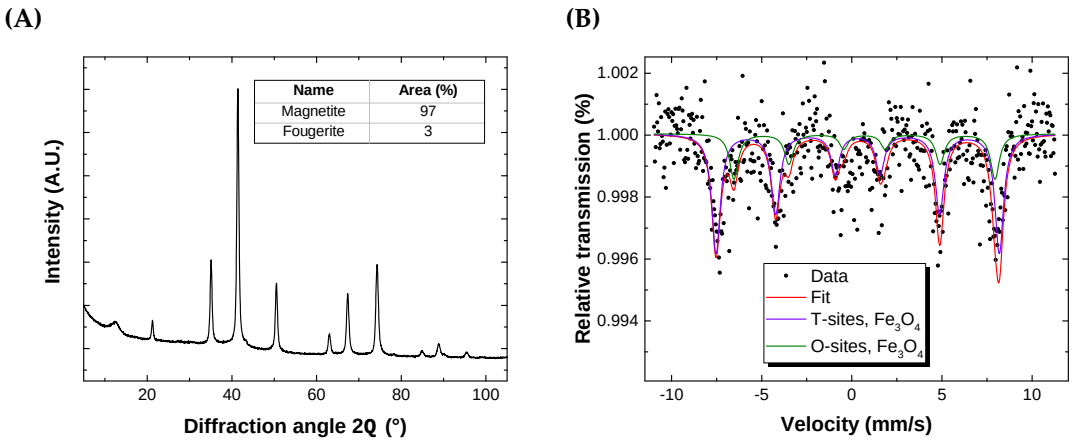

Figure 53 JW_SGO_T_Fe: **(A)** XRD pattern, **(B)** room temperature ^{57}Fe zero-field Mössbauer spectrum.

Sample Component	**Isomer shift** δ (mm s^{-1})	**Quadrupole splitting** δE_Q (mm s^{-1})	**Hyperfine mag. field** B_{hf} (T)	**Spectral area** (%)
JW_SGO_T_Fe				
T-sites, Fe_3O_4	0.32	0.00	48.82	72.5
O-sites, Fe_3O_4	0.70	0.00	45.00	27.5

Table 10 The hyperfine parameters of the room temperature ^{57}Fe zero-field Mössbauer spectrum of JW_SGO_T_Fe.

In conclusion, the sulphonated GO-iron oxide compound was prepared by multi-step method involving sulphonation of GO, solvothermal synthesis of magnetite nanoparticles, and subsequent mixing of sulphonated GO and magnetite nanoparticles in aqueous environment under sonication. The incorporation of sulphur into the GO structure was confirmed by XPS and STA-MS measurements. The XRD pattern analysed by Rietveld method revealed the presence of magnetite and traces of fougerite. Highly non-stoichiometric magnetite was observed in the room temperature ^{57}Fe zero-field Mössbauer spectrum as two sextets. Deconvolution of high resolution XPS spectra suggests the bonding of Fe-OC type, similarly to the other hybrid systems.

4. Conclusion

The physical and chemical properties of graphene, GO, and iron oxide phases together with the concepts of batteries based on Li-ion current were discussed in the theoretical part of this work. The second part served as an introduction to the principles of the characterization techniques used and description of the instrumentation employed.

The GO-iron oxide nanoparticles hybrid materials were prepared with four different methods using GO made by modified Hummers method and Tour method as the starting material. Most of the samples were fully characterized by TEM to get the information about particle size and coverage of GO by iron oxide nanoparticles. FT-IR and Raman spectroscopy were used for investigation of oxygen functional groups and vibration modes of iron oxides phases. The amount and the identity of iron oxide nanoparticles were determined using XRD, STA-MS and room temperature ^{57}Fe zero-field Mössbauer spectroscopy.

The GO-iron oxide composites prepared by iron (II) and iron (III) salt decomposition possess a large coverage of GO. The iron oxide nanoparticles show superparamagnetic behaviour and their size is the smallest among all iron oxide nanoparticles presented in this work. The GO-iron oxide composites synthesised by hydrothermal method show different amount of hematite incorporated within the hybrid structure depending on the ratio between starting iron (III) chloride hexahydrate and GO. The samples which were subsequently thermally treated at 500 °C under nitrogen display hematite to magnetite transformation. The conversion rate of this transformation increases with the amount of carbon present in the hybrid structure and with the size decrease of hematite nanoparticles. The last synthesis of GO-iron oxide hybrid systems consisted of sulphonation of GO, solvothermal preparation of magnetite nanoparticles, and anchoring of GO to magnetite nanoparticles upon sonication. The resulting nanoparticles were identified as containing highly non-stoichiometric magnetite. On the other hand, the hybrid system synthesised by thermal decomposition of ferric acetylacetonate in NMP displays a relatively low amount of iron oxide according to the STA-MS and the characterisation of this hybrid was not fully performed.

This work has provided complete characterisation of synthesised GO-iron oxide hybrid systems with the emphasis on the most critical parameters affecting the performance of devices for energy storage, such as size and shape of iron oxide nanoparticles, coverage of GO, phase of iron oxide involved, and stoichiometry in the case of magnetite. It was shown that both GOs are suitable for the preparation of hybrid systems. All samples provide relatively dense coverage of GO by iron oxide nanoparticles creating porous structure making hybrid materials suitable for active lithium storage application. Among the various materials prepared and characterised, those synthesised by hydrothermal method with subsequent thermal treatment show high potential for future application due to relatively well defined magnetite nanoparticles and presence of thermally reduced GO, which is more conductive than pristine GO. We hope that this work will help to understand the physical and chemical properties of GO-iron oxide hybrid compounds and will lead to further development of similar structures.

References

1. Papageorgiou, D. G., Kinloch, I. A. & Young, R. J. Mechanical properties of graphene and graphene-based nanocomposites. *Progress in Materials Science* **90,** 75–127. ISSN: 00796425 (2017).
2. Geim, A. K. & Novoselov, K. S. The rise of graphene. *Nature Materials* **6,** 183–191. ISSN: 1476-1122 (2007).
3. Bolotin, K. I., Sikes, K. J., Jiang, Z., Klima, M., Fudenberg, G., Hone, J., Kim, P. & Stormer, H. L. Ultrahigh electron mobility in suspended graphene. *Solid State Communications* **146,** 351–355. ISSN: 00381098 (2008).
4. Balandin, A. a., Ghosh, S., Bao, W., Calizo, I., Teweldebrhan, D., Miao, F. & Lau, C. N. Superior Thermal Conductivity of Single-Layer Graphene 2008. *Nano Lett.* **8,** 902–907. ISSN: 1530-6984 (2008).
5. Novoselov, K. S., Geim, A. K., Morozov, S., Jiang, D., Zhang, Y., Dubonos, S. V., Grigorieva, I. V. & Firsov, A. A. Electric Field Effect in Atomically Thin Carbon Films. *Science* **306,** 666–669. ISSN: 0036-8075 (2004).
6. Huss, E. *The Nobel Prize in Physics 2010* https://www.nobelprize.org/nobel_prizes/physics/laureates/2010/press.html.
7. Novoselov, K., Geim, A., Morozov, S.V., Jiang, D., Katsnelson, M., Grigorieva, I., S.V., Dubonos & Firsov, A. Two-Dimensional Gas of Massless Dirac Fermions in Graphene. *Nature* **438,** 197–200. ISSN: 0028-0836 (2005).
8. Geim, A. K. Nobel Lecture: Random walk to graphene. *Reviews of Modern Physics* **83,** 851–862. ISSN: 00346861 (2011).
9. Novoselov, K. S. Nobel Lecture: Graphene: Materials in the Flatland. *Reviews of Modern Physics* **83,** 837–849. ISSN: 00346861 (2011).
10. Castro Neto, A. H., Guinea, F., Peres, N. M. R., Novoselov, K. S. & Geim, A. K. The electronic properties of graphene. *Reviews of Modern Physics* **81,** 109–162. ISSN: 00346861 (2009).
11. Young, A. F. & Kim, P. Quantum interference and Klein tunnelling in graphene heterojunctions. *Nature Physics* **5,** 222–226. ISSN: 1745-2473 (2009).
12. Laughlin, R. B. Quantized Hall conductivity in two dimensions. *Physical Review B* **23,** 5632–5633. ISSN: 01631829 (1981).
13. Novoselov, K. S., Jiang, Z., Zhang, Y., Morozov, S. V., Stormer, H. L., Zeitler, U., Maan, J. C., Boebinger, G. S., Kim, P. & Geim, A. K. Room-Temperature Quantum Hall Effect in Graphene. *Science* **315,** 1379–1379. ISSN: 0036-8075 (2007).
14. Suk, J. W., Kitt, A., Magnuson, C. W., Hao, Y., Ahmed, S., An, J., Swan, A. K., Goldberg, B. B. & Ruoff, R. S. Transfer of CVD-grown monolayer graphene onto arbitrary substrates. *ACS Nano* **5,** 6916–6924. ISSN: 19360851 (2011).
15. Zhang, Y., Zhang, L. & Zhou, C. Review of chemical vapor deposition of graphene and related applications. *Accounts of Chemical Research* **46,** 2329–2339. ISSN: 00014842 (2013).
16. Mishra, N., Boeckl, J., Motta, N. & Iacopi, F. Graphene growth on silicon carbide: A review. *Physica Status Solidi (a)* **213,** 2277–2289. ISSN: 18626300 (2016).
17. Dreyer, D. R., Todd, A. D. & Bielawski, C. W. Harnessing the chemistry of graphene oxide. *Chemical Society reviews* **43,** 5288–5301. ISSN: 1460-4744 (2014).
18. Chua, C. K. & Pumera, M. Chemical reduction of graphene oxide: a synthetic chemistry viewpoint. *Chemical Society reviews* **43,** 291–312. ISSN: 1460-4744 (2014).
19. Dreyer, D. R., Park, S., Bielawski, C. W. & Ruoff, R. S. The chemistry of graphene oxide. *Chemical Society Reviews* **39,** 228–240. ISSN: 0306-0012 (2010).
20. He, H., Riedl, T., Lerf, A. & Klinowski, J. Solid-State NMR Studies of the Structure of Graphite Oxide. *The Journal of Physical Chemistry* **100,** 19954–19958. ISSN: 0022-3654 (1996).
21. Poh, H. L., Šaněk, F., Ambrosi, A., Zhao, G., Sofer, Z. & Pumera, M. Graphenes prepared by Staudenmaier, Hofmann and Hummers methods with consequent thermal exfoliation exhibit very different electrochemical properties. *Nanoscale* **4,** 3515. ISSN: 2040-3364 (2012).

22. Li, J., Zeng, X., Ren, T. & van der Heide, E. The Preparation of Graphene Oxide and Its Derivatives and Their Application in Bio-Tribological Systems. *Lubricants* **2,** 137–161. ISSN: 2075-4442 (2014).

23. Hummers, W. S. & Offeman, R. E. Preparation of Graphitic Oxide. *Journal of the American Chemical Society* **80,** 1339. ISSN: 0002-7863 (1958).

24. Marcano, D. C., Kosynkin, D. V., Berlin, J. M., Sinitskii, A., Sun, Z., Slesarev, A., Alemany, L. B., Lu, W. & Tour, J. M. Improved synthesis of graphene oxide. *ACS Nano* **4,** 4806–4814. ISSN: 19360851 (2010).

25. Hun, S. Thermal Reduction of Graphene Oxide. *Physics and Applications of Graphene - Experiments.* doi:10.5772/14156 (2011).

26. Tian, S., Sun, J., Yang, S., He, P., Ding, S., Ding, G. & Xie, X. Facile thermal annealing of graphite oxide in air for graphene with a higher C/O ratio. *RSC Adv.* **5,** 69854–69860. ISSN: 2046-2069 (2015).

27. Kroto, H. W., Heath, J. R., O'Brien, S. C., Curl, R. F. & Smalley, R. E. C60: Buckminsterfullerene. *Nature* **318,** 162–163. ISSN: 00280836 (1985).

28. Georgakilas, V., Perman, J. A., Tucek, J. & Zboril, R. Broad Family of Carbon Nanoallotropes: Classification, Chemistry, and Applications of Fullerenes, Carbon Dots, Nanotubes, Graphene, Nanodiamonds, and Combined Superstructures. *Chemical Reviews* **115,** 4744–4822. ISSN: 15206890 (2015).

29. Osawa, E. *Perspectives of fullerene nanotechnology* (Kluwer Academic Publishers, 2002).

30. Dong, Y., Shao, J., Chen, C., Li, H., Wang, R., Chi, Y., Lin, X. & Chen, G. Blue luminescent graphene quantum dots and graphene oxide prepared by tuning the carbonization degree of citric acid. *Carbon* **50,** 4738–4743. ISSN: 00086223 (2012).

31. Saito, R., Dresselhaus, G. & Dresselhaus, M. S. *Physical properties of carbon nanotubes* (Imperial College Press, 1998).

32. *Zyvex* http://www.zyvextech.com/.

33. Deluca, M. J., Felker, C. j., Heider, D., Pandey, G., Abuobaid, A., Thostenson, E. T. & Gillespie Jr, J. W. *System and methods for use in monitoring a structure* 2016.

34. Peng, L. M., Zhang, Z. & Wang, S. Carbon nanotube electronics: Recent advances. *Materials Today* **17,** 433–442. ISSN: 13697021 (2014).

35. Chatterjee, J., Haik, Y. & Chen, C.-J. Size dependent magnetic properties of iron oxide nanoparticles. *Journal of Magnetism and Magnetic Materials* **257,** 113–118. ISSN: 03048853 (2003).

36. Tuček, J., Tuček, P., Čuda, J., Filip, J., Pechoušek, J., Machala, L. & Zbořil, R. Iron(III) oxide polymorphs and their manifestations in in-field ^{57}Fe Mössbauer spectra. *AIP Conference Proceedings* **1489,** 56–74. ISSN: 0094243X (2012).

37. Teja, A. S. & Koh, P. Y. Synthesis, properties, and applications of magnetic iron oxide nanoparticles. *Progress in Crystal Growth and Characterization of Materials* **55,** 22–45. ISSN: 09608974 (2009).

38. Cornell, R. & Schwertmann, U. *The iron oxides: structure, properties, reactions, occurrence and uses* (VCH, 2006).

39. Zboril, R., Mashlan, M. & Petridis, D. Iron(III) Oxides from Thermal Processess-Synthesis, Structural and Magnetic Properties, Mössbauer Spectroscopy Characterization, and Applications. *Chemistry of Materials* **14,** 969–982. ISSN: 09317597 (2002).

40. Agarwala, S., Lim, Z. H., Nicholson, E. & Ho, G. W. Probing the morphology-device relation of Fe_2O_3 nanostructures towards photovoltaic and sensing applications. *Nanoscale* **4,** 194–205. ISSN: 2040-3364 (2012).

41. Zhu, W. C., Cui, X. L., Liu, X. F., Zhang, L. Y., Huang, J. Q., Piao, X. L. & Zhang, Q. Hydrothermal evolution, optical and electrochemical properties of hierarchical porous hematite nanoarchitectures. *Nanoscale Research Letters* **8,** 1–14. ISSN: 19317573 (2013).

42. Machala, L., Tuček, J. & Zbořil, R. Polymorphous transformations of nanometric iron(III) oxide: A review. *Chemistry of Materials* **23,** 3255–3272. ISSN: 08974756 (2011).

43. Tuček, J., Zbořil, R., Namai, A. & Ohkoshi, S. I. ϵ-Fe2O3: An advanced nanomaterial exhibiting giant coercive field, millimeter-wave ferromagnetic resonance, and magnetoelectric coupling. *Chemistry of Materials* **22,** 6483–6505. ISSN: 08974756 (2010).

44. Kohout, J., Brázda, P., Závěta, K., Kubániová, D., Kmječ, T., Kubíčková, L., Klementová, M., Šantavá, E. & Lančok, A. The magnetic transition in ϵ-Fe_2O_3 nanoparticles: Magnetic properties and hyperfine interactions from Mössbauer spectroscopy. *Journal of Applied Physics* **117,** 113–117. ISSN: 10897550 (2015).

45. Wu, W., He, Q. & Jiang, C. Magnetic iron oxide nanoparticles: Synthesis and surface functionalization strategies. *Nanoscale Research Letters* **3,** 397–415. ISSN: 19317573 (2008).

46. Ali, A., Zafar, H., Zia, M., ul Haq, I., Phull, A. R., Ali, J. S. & Hussain, A. Synthesis, characterization, applications, and challenges of iron oxide nanoparticles. *Nanotechnology, Science and Applications* **9,** 49–67. ISSN: 11778903 (2016).

47. Ruren, X. & Yan, X. *Modern inorganic synthetic chemistry* (Elsevier, 2017).

48. Nishi, Y. Lithium ion secondary batteries; past 10 years and the future. *Journal of Power Sources* **100,** 101–106. ISSN: 03787753 (2001).

49. Goriparti, S., Miele, E., Francesco, D. A., Fabrizio, D. E., Zaccaria, P. R. & Capiglia, C. Review on recent progress of nanostructured anode materials for Li-ion batteries. *Journal of Power Sources* **257,** 421–443. ISSN: 03787753 (2014).

50. Bergveld, H. J., Kruijt, W. S. & Notten, P. H. L. *Battery management systems: design by modelling* (Springer, 2011).

51. Goodenough, J. B. & Kim, Y. Challenges for rechargeable Li batteries. *Chemistry of Materials* **22,** 587–603. ISSN: 08974756 (2010).

52. Cao, C., Li, Z.-B., Wang, X.-L., Zhao, X.-B. & Han, W.-Q. Recent Advances in Inorganic Solid Electrolytes for Lithium Batteries. *Frontiers in Energy Research* **2,** 1–10. ISSN: 2296-598X (2014).

53. Sun, W. & Wang, Y. Graphene-based nanocomposite anodes for lithium-ion batteries. *Nanoscale* **6,** 11528–11552. ISSN: 2040-3364 (2014).

54. Jana, A., Scheer, E. & Polarz, S. Synthesis of graphene-transition metal oxide hybrid nanoparticles and their application in various fields. *Beilstein Journal of Nanotechnology* **8,** 688–714. ISSN: 21904286 (2017).

55. Tuček, J., Kemp, K. C., Kim, K. S. & Zbořil, R. Iron-Oxide-Supported Nanocarbon in Lithium-Ion Batteries, Medical, Catalytic, and Environmental Applications. *ACS Nano* **8,** 7571–7612 (2014).

56. Zhou, J., Song, H., Ma, L. & Chen, X. Magnetite/graphene nanosheet composites: interfacial interaction and its impact on the durable high-rate performance in lithium-ion batteries. *RSC Advances* **1,** 782. ISSN: 2046-2069 (2011).

57. Liu, J., Xue, Y. & Dai, L. Sulfated graphene oxide as a hole-extraction layer in high-performance polymer solar cells. *Journal of Physical Chemistry Letters* **3,** 1928–1933. ISSN: 19487185 (2012).

58. Jiao, T., Liu, Y., Wu, Y., Zhang, Q., Yan, X., Gao, F., Bauer, A. J., Liu, J., Zeng, T. & Li, B. Facile and Scalable Preparation of Graphene Oxide-Based Magnetic Hybrids for Fast and Highly Efficient Removal of Organic Dyes. *Scientific Reports* **5,** 1–10. ISSN: 20452322 (2015).

59. Raman, C. V. & Krishnan, K. S. A New Type of Secondary Radiation. *Nature* **121,** 501–502 (1928).

60. Ferraro, J. R., Nakamoto, K. & Brown, C. W. *Introductory Raman spectroscopy* (Academic Press, 2009).

61. Colthup, N. B., Daly, L. H. & Wiberley, S. E. *Introduction to infrared and Raman spectroscopy* (Academic Press, 1998).

62. Ferrari, A. C., Meyer, J. C., Scardaci, V., Casiraghi, C., Lazzeri, M., Mauri, F., Piscanec, S., Jiang, D., Novoselov, K. S., Roth, S. & Geim, A. K. Raman spectrum of graphene and graphene layers. *Physical Review Letters* **97,** 1–4. ISSN: 00319007 (2006).

63. Ferrari, A. C. Raman spectroscopy of graphene and graphite: Disorder, electron-phonon coupling, doping and nonadiabatic effects. *Solid State Communications* **143,** 47–57. ISSN: 00381098 (2007).

64. Childres, I., Jauregui, L., Park, W., Cao, H., & Chen, Y. Raman Spectroscopy of Graphene and Related Materials. *New Developments in Photon and Materials Research*, 1–20. ISSN: 1626183392 (2013).

65. Ferrari, A. C. & Basko, D. M. Raman spectroscopy as a versatile tool for studying the properties of graphene. *Nature Nanotechnology* **8,** 235–246. ISSN: 17483395 (2013).

66. Wu, J.-B., Lin, M.-L., Cong, X., Liu, H.-N. & Tan, P.-H. Raman spectroscopy of graphene-based materials and its applications in related devices. *Chemical Society Reviews* **47,** 1822–1873. ISSN: 0306-0012 (2018).

67. Jubb, A. M. & Allen, H. C. Vibrational spectroscopic characterization of hematite, maghemite, and magnetite thin films produced by vapor deposition. *ACS Applied Materials and Interfaces* **2,** 2804–2812. ISSN: 19448244 (2010).

68. Shebanova, O. N. & Lazor, P. Raman spectroscopic study of magnetite ($FeFe_2O_4$): A new assignment for the vibrational spectrum. *Journal of Solid State Chemistry* **174,** 424–430. ISSN: 00224596 (2003).

69. Bergmann CP, P. P. Raman Spectroscopy of Iron Oxide of Nanoparticles (Fe_3O_4). *Journal of Material Science & Engineering* **05,** 4–6. ISSN: 21690022 (2015).

70. Griffiths, P. R. & A., D. H. J. *Fourier transform infrared spectrometry* (John Wiley & Sons, 2007).

71. Acik, M., Lee, G., Mattevi, C., Chhowalla, M., Cho, K. & Chabal, Y. J. Unusual infrared-absorption mechanism in thermally reduced graphene oxide. *Nature Materials* **9,** 840–845. ISSN: 14764660 (2010).

72. Zhang, H., Hines, D. & Akins, D. L. Synthesis of a nanocomposite composed of reduced graphene oxide and gold nanoparticles. *Dalton Trans.* **43,** 2670–2675. ISSN: 1477-9226 (2014).

73. Shahriary, L. & Athawale, A. a. Graphene Oxide Synthesized by using Modified Hummers Approach. *International Journal of Renewable Energy and Environmental Engineering* **02,** 58–63 (2014).

74. *XPS - Carbon* https://xpssimplified.com/elements/carbon.php.

75. *X-ray Photoelectron Spectroscopy (XPS) Reference Pages* http://www.xpsfitting.com/search/label/carbon.

76. *XPS of Carbon Nanomaterials* https://archive.cnx.org/contents/fdddbf98-39ce-4edc-934e-dd1f7477b52b@2/xps-of-carbon-nanomaterials.

77. Zhou, J., Song, H., Ma, L. & Chen, X. Magnetite/graphene nanosheet composites: interfacial interaction and its impact on the durable high-rate performance in lithium-ion batteries. *RSC Advances* **1,** 782. ISSN: 2046-2069 (2011).

78. Mattevi, C., Eda, G., Agnoli, S., Miller, S., Mkhoyan, K. A., Celik, O., Mastrogiovanni, D., Granozzi, G., Carfunkel, E. & Chhowalla, M. Evolution of electrical, chemical, and structural properties of transparent and conducting chemically derived graphene thin films. *Advanced Functional Materials* **19,** 2577–2583. ISSN: 16163028 (2009).

79. Coats, A. W. & Redfern, J. P. Thermogravimetric analysis. *Analyst (London)* **88,** 906–924 (1963).

80. May, L. *An Introduction to Mössbauer Spectroscopy* (Plenum Press, 1971).

81. *Introduction to Mössbauer Spectroscopy* http://www.rsc.org/Membership/Networking/InterestGroups/MossbauerSpect/intro.asp.

82. *Mössbauer Spectroscopy* 2017. https://serc.carleton.edu/research_education/geochemsheets/techniques/mossbauer.html.

83. Klencsár, Z., Kuzmann, E. & Vértes, A. User-friendly software for Mössbauer spectrum analysis. *Journal of Radioanalytical and Nuclear Chemistry* **210,** 105–118. ISSN: 02365731 (1996).

84. Liu, J., Xue, Y. & Dai, L. Sulfated graphene oxide as a hole-extraction layer in high-performance polymer solar cells. *Journal of Physical Chemistry Letters* **3,** 1928–1933. ISSN: 19487185 (2012).

85. Roy Chowdhury, D., Singh, C. & Paul, A. Role of graphite precursor and sodium nitrate in graphite oxide synthesis. *RSC Advances* **4,** 15138. ISSN: 2046-2069 (2014).

86. Et al. Shen, J. One step synthesis of graphene oxide-magnetic nanoparticle composite. *Journal of Physical Chemistry C* **114,** 1498–1503. ISSN: 19327447 (2010).

87. Alizadeh, A., Abdi, G., Khodaei, M. M., Ashokkumar, M. & Amirian, J. Graphene oxide/Fe_3O_4 /SO_3H nanohybrid: a new adsorbent for adsorption and reduction of Cr(VI) from aqueous solutions. *RSC Adv.* **7,** 14876–14887. ISSN: 2046-2069 (2017).

88. Li, S. & Hihara, L. H. A Micro-Raman Spectroscopic Study of Marine Atmospheric Corrosion of Carbon Steel: The Effect of Akaganeite. *Journal of the Electrochemical Society* **162,** C495–C502. ISSN: 0013-4651 (2015).

89. *Iron XPS* https://xpssimplified.com/elements/iron.php.

90. Zubir, N. A., Yacou, C., Motuzas, J., Zhang, X. & Diniz Da Costa, J. C. Structural and functional investigation of graphene oxide-Fe_3O_4 nanocomposites for the heterogeneous Fenton-like reaction. *Scientific Reports* **4,** 1–8. ISSN: 20452322 (2014).

91. Srinivasan, N. S. & Lahiri, a. K. Studies on the Reduction of Hematite by Carbon. *Metallurgical Transactions* **8B,** 175–178. ISSN: 0360-2141 (1977).

92. Yu, J., Han, Y., Li, Y., Gao, P. & Li, W. Mechanism and Kinetics of the Reduction of Hematite to Magnetite with CO–CO_2 in a Micro-Fluidized Bed. *Minerals* **7,** 209. ISSN: 2075-163X (2017).

93. Monazam, E. R., Breault, R. W. & Siriwardane, R. Kinetics of magnetite (Fe_3O_4) oxidation to hematite (Fe_2O_3) in air for chemical looping combustion. *Industrial and Engineering Chemistry Research* **53,** 13320–13328. ISSN: 15205045 (2014).

94. Doriguetto, A. C., Fernandes, N. G., Persiano, A. I. C., Nunes Filho, E, Grenèche, J. M. & Fabris, J. D. Characterization of a natural magnetite. *Phys Chem Minerals* **30,** 249–255. ISSN: 1432-2021 (2003).

95. Poh, H. L., Šimek, P., Sofer, Z. & Pumera, M. Sulfur-doped graphene via thermal exfoliation of graphite oxide in H 2S, SO2, or CS2 gas. *ACS Nano* **7,** 5262–5272. ISSN: 19360851 (2013).

96. Sun, H., Xu, G. L., Xu, Y. F., Sun, S. G., Zhang, X., Qiu, Y. & Yang, S. A composite material of uniformly dispersed sulfur on reduced graphene oxide: Aqueous one-pot synthesis, characterization and excellent performance as the cathode in rechargeable lithium-sulfur batteries. *Nano Research* **5,** 726–738. ISSN: 19980124 (2012).

97. Huang, H., Lu, Y.-C., Wang, A.-J., Liu, J.-H., Chen, J.-R. & Feng, J.-J. A facile, green, and solvent-free route to nitrogen–sulfur-codoped fluorescent carbon nanoparticles for cellular imaging. *RSC Adv.* **4,** 11872–11875. ISSN: 2046-2069 (2014).

98. Qie, L., Chen, W., Xiong, X., Hu, C., Zou, F., Hu, P. & Huang, Y. Sulfur-Doped Carbon with Enlarged Interlayer Distance as a High-Performance Anode Material for Sodium-Ion Batteries. *Advanced Science* **2** (2015).

List of Figures

1. Energy spectrum of graphene. . . . 10
2. Models of GO . . . 11
3. GO reduction . . . 13
4. Carbon allotropes overview . . . 14
5. Types of CNT . . . 15
6. Scheme of iron oxides . . . 16
7. Types of magnetism. . . . 17
8. Crystallographic structure of α-Fe_2O_3 and β-Fe_2O_3 . . . 18
9. Crystallographic structure of γ-Fe_2O_3 and ϵ-Fe_2O_3 . . . 19
10. Battery cycles . . . 21
11. Raman scattering . . . 24
12. Fourier Transformed Infrared Spectroscopy scheme . . . 26
13. Scheme of FT-IR setup . . . 26
14. Braggs law . . . 28
15. XRD Bragg-Brentano geometry . . . 28
16. STA-MS instrument . . . 29
17. Information obtained from Mössbauer spectroscopy . . . 30
18. Samples overview . . . 31
19. JW_GO_H – TEM images . . . 33
20. JW_GO_H – Vibration spectroscopy . . . 33
21. JW_GO_H – XPS elemental survey. . . . 34
22. JW_GO_H – High resolution XPS spectra. . . . 34
23. JW_GO_H – STA-MS . . . 35
24. JW_GO_T – XPS elemental survey. . . . 36
25. JW_GO_T – High resolution XPS of C1s peak. . . . 36
26. JW_GO_T – High resolution XPS of O1s peak. . . . 37
27. JW_GO_T – TEM images . . . 37
28. JW_GO_T – Vibration spectroscopy . . . 38
29. JW_Fe_GO_1S – STA and MS . . . 39
30. JW_Fe_GO – TEM. . . . 40
31. JW_Fe_GO – Vibration spectroscopy. . . . 41
32. JW_Fe_GO – XPS spectra. . . . 42
33. JW_Fe_GO – XRD patterns and ^{57}Fe Mössbauer spectra. . . . 43
34. JW_Fe_GO – STA-MS. . . . 44
35. JW_FeA based on JW_GO_H – TEM images and size histograms . . . 46
36. JW_FeA based on JW_GO_T – TEM images and size histograms . . . 47
37. JW_FeA – Vibration spectroscopy. . . . 48
38. JW_FeA – XPS elemental survey. . . . 49
39. JW_FeA – C1s and Fe2p peaks of high resolution XPS spectra. . . . 50
40. JW_FeA – O1s peak of high resolution XPS spectra. . . . 51
41. JW_FeA – XRD patterns. . . . 52
42. JW_FeA – STA-MS. . . . 53
43. JW_FeA with subsequent thermal treatment – STA-MS. . . . 54
44. JW_FeA_H2_N – STA-MS. . . . 55
45. JW_FeA – ^{57}Fe Mössbauer spectra. . . . 56
46. JW_SGO-magnetite composites – TEM images . . . 58
47. JW_SGO-magnetite composites – vibration spectroscopy . . . 59
48. JW_SGO – XPS elemental survey and high resolution XPS of C1s and O1s peak . . . 60
49. JW_SGO – high resolution XPS spectrum of S2p . . . 61
50. JW_SGO-magnetite composites – XPS elemental survey . . . 61
51. JW_SGO-magnetite composites – high resolution XPS spectra . . . 62
52. JW_SGO-magnetite composites – STA-MS . . . 63
53. JW_SGO_T_Fe – XRD and Mössbauer spectroscopy . . . 64

A.1. JW_Fe_GO – TEM with EDS. . . . 76
A.2. JW_FeA_H and JW_FeA_H_N – TEM with EDS. . . . 76
A.3. JW_FeA_H2 and JW_FeA_H2_N – TEM with EDS. . . . 77
A.4. JW_FeA_T and JW_FeA_T_N – TEM with EDS. . . . 77

A.5. JW_SGO_H_Fe and JW_SGO_T_Fe – TEM with EDS. 78
B.1. JW_Fe_GO – XRD Rietveld analysis. 79
B.2. JW_Fe_GO – XRD Rietveld analysis. 79
B.3. JW_SGT_F2_2 – XRD Rietveld analysis. 80
C.1. JW_FeA – Unprocessed FT-IR. 81

List of Tables

1. Raman active phonon modes of iron oxide phases. 25
2. XPS C1s Peak Deconvolution 27
3. XPS O1s Peak Deconvolution 27
4. JW_Fe_GO – ^{57}Fe Mössbauer spectra hyperfine components 43
5. Hydrothermal method sample labels 45
6. JW_FeA – TEM size and XRD MCL 47
7. JW_FeA – STA parameters 54
8. JW_FeA – ^{57}Fe Mössbauer spectra hyperfine components 55
9. JW_SGO-magnetite composites – TEM size and XRD MCL 58
10. JW_SGO_T_Fe – ^{57}Fe Mössbauer spectra hyperfine components 64

List of Abbreviations

GO	**G**raphene **O**xide
rGO	**r**educed **G**raphene **O**xide
CVD	**C**hemical **V**apour **D**eposition
XRD	**X**-**R**ay **D**iffraction
NMR	**N**uclear **M**agnetic **R**esonance
XPS	**X**ray **P**hotoelectron **S**pectroscopy
FT-IR	**F**ourier **T**ransform **I**fra **R**ed spectroscopy
CNT	**C**arbon **N**ano**t**ube
TEM	**T**ransmission **E**lectron **M**icroscopy
EDS	**E**nergy **D**ispersive X-ray Spectroscopy
ATR	**A**ttenuated **T**otal **R**eflectance
STA	**S**imultaneous **T**hermal **A**nalysis
CCD	**C**harge-**C**oupled **D**evice
FWHM	**F**ull **W**idth at **H**alf **M**aximum
MLC	**M**ean **C**oherence **L**ength
TGA	**T**hermal **G**ravimetric **A**nalysis
DCS	**D**ifferential **S**canning **C**alorimetry
MS	**M**ass **S**pectroscopy

Physical Constants

Speed of Light	$c = 2.997\,924\,58 \times 10^{8}\,\mathrm{m\,s^{-1}}$
Planks constant	$h = 6.626\,070\,04 \times 10^{-34}\,\mathrm{m^{2}\,kg\,s^{-1}}$
Elementary charge	$e = 1.602\,176\,620\,8(98) \times 10^{-19}\,\mathrm{C}$
von Klitzing constant	$R_K = 25\,812.807\,557(18)\,\Omega$
Boltzmann constant	$k = 1.380\,648\,52(79) \times 10^{-23}\,\mathrm{J\,K^{-1}}$

List of Symbols

v_f	Fermi velocity	$\mathrm{m\,s^{-1}}$
m_0	Invariant mass	kg
M	Magnetization	$\mathrm{A\,m^{-1}}$
H	Magnetic Field	$\mathrm{A\,m^{-1}}$
T_N	Neél temperature	K
T_C	Curie temperature	K
T_M	Morin transition temperature	K
T	Absolute temperature	K
$E_{binding}$	Binding energy of an electron	eV
E_{photon}	Energy of a X-ray photon	eV
$E_{kinetic}$	Kinetic energy measured by XPS	eV
d	Interlayer distance	Å
n	Order of diffraction	1
δE_Q	Quadrupole splitting	$\mathrm{mm\,s^{-1}}$
B_hf	Hyperfine mag. field	T
χ_m	Magnetic susceptibility	1
$\tilde{\nu}$	Wavenumber	$\mathrm{cm^{-1}}$
λ_0	Excitation wavelength	nm
λ_m	Raman spectrum wavelength	nm
ϕ	Work function	eV
Θ	Angle of the incident X-Ray radiation	°
λ	Wavelength of X-ray photons	Å
δ	Isomer shift	$\mathrm{mm\,s^{-1}}$

Appendix A – EDS

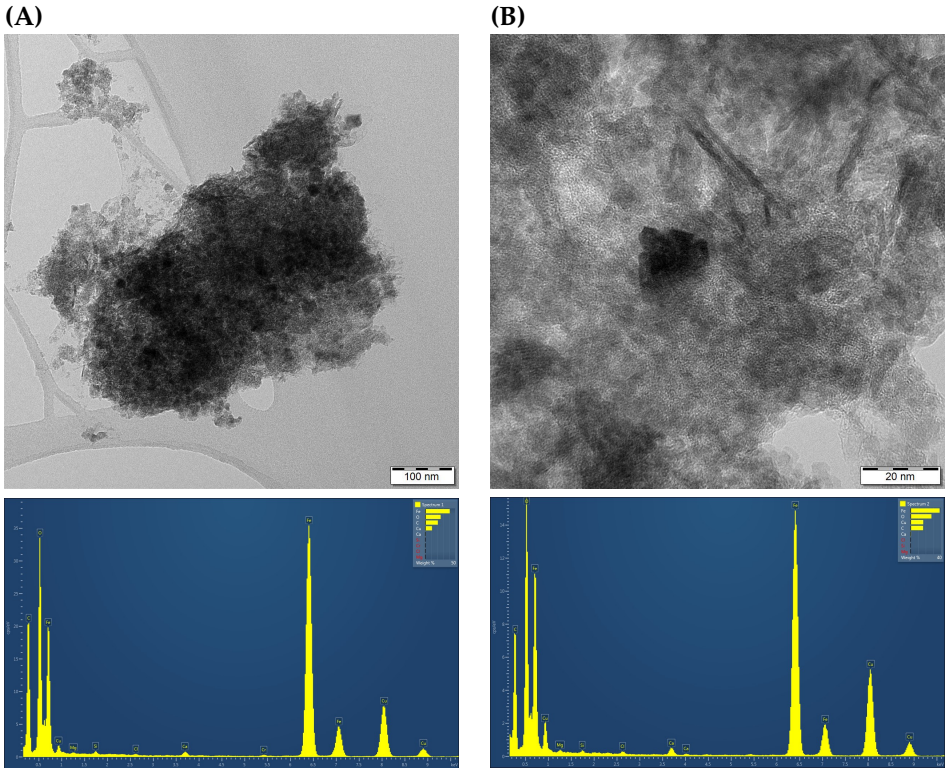

Figure A.1 EDS analysis with corresponding TEM image: **(A)** JW_Fe_GO_T and **(B)** JW_Fe_GO_H.

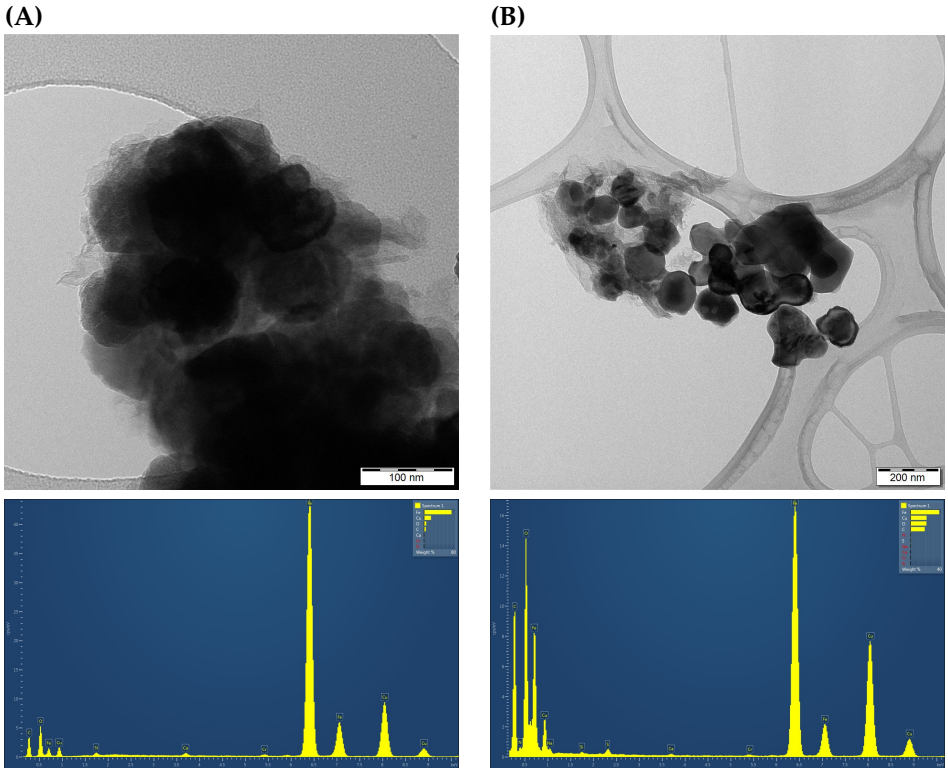

Figure A.2 EDS analysis with corresponding TEM image: **(A)** JW_FeA_H and **(B)** JW_FeA_H_N.

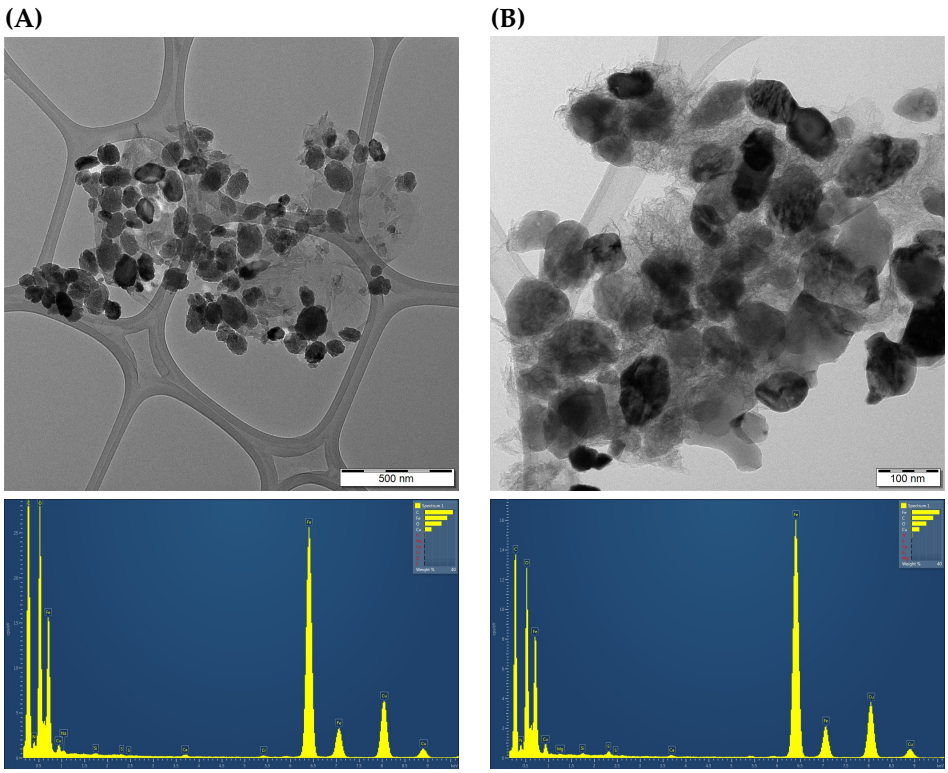

Figure A.3 EDS analysis with corresponding TEM image: **(A)** JW_FeA_H2 and **(B)** JW_FeA_H2_N.

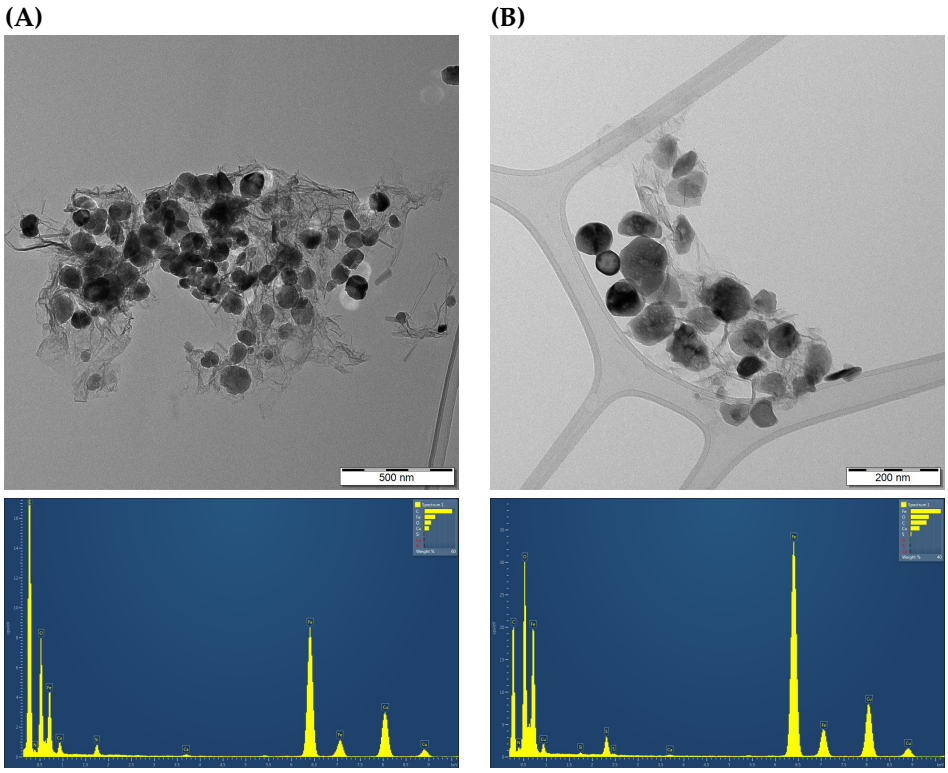

Figure A.4 EDS analysis with corresponding TEM image: **(A)** JW_FeA_T and **(B)** JW_FeA_T_N.

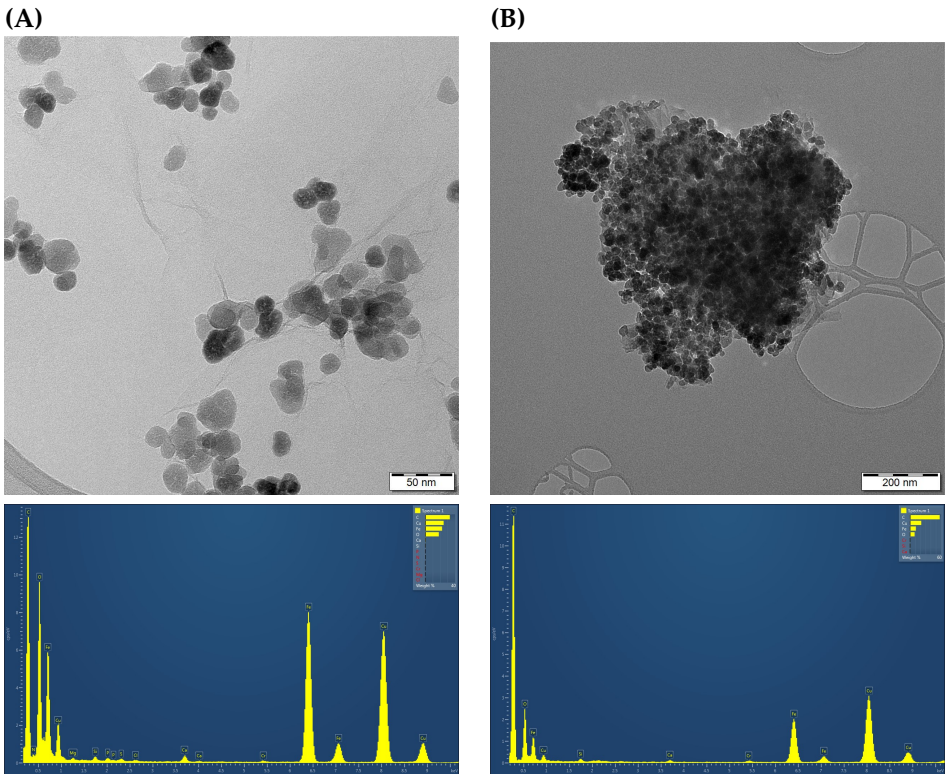

Figure A.5 EDS analysis with corresponding TEM image: **(A)** JW_SGO_H_Fe and **(B)** JW_SGO_T_Fe.

Appendix B – XRD Rietveld analysis

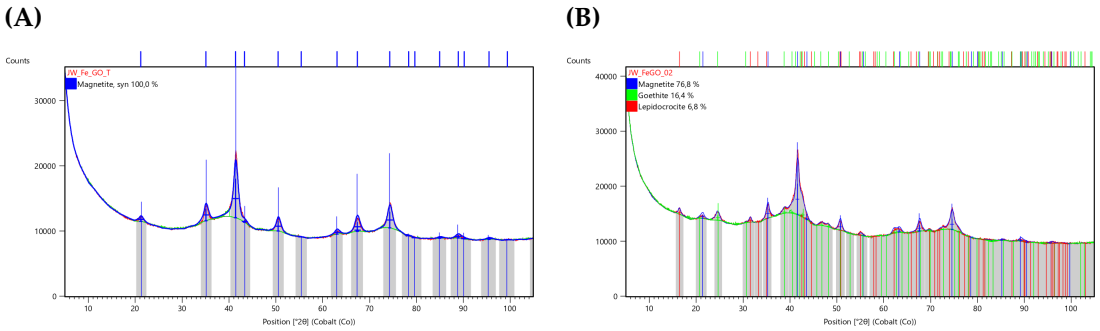

Figure B.1 | Rietveld analysis of XRD patterns of **(A)** JW_Fe_GO_T and **(B)** JW_Fe_GO_H.

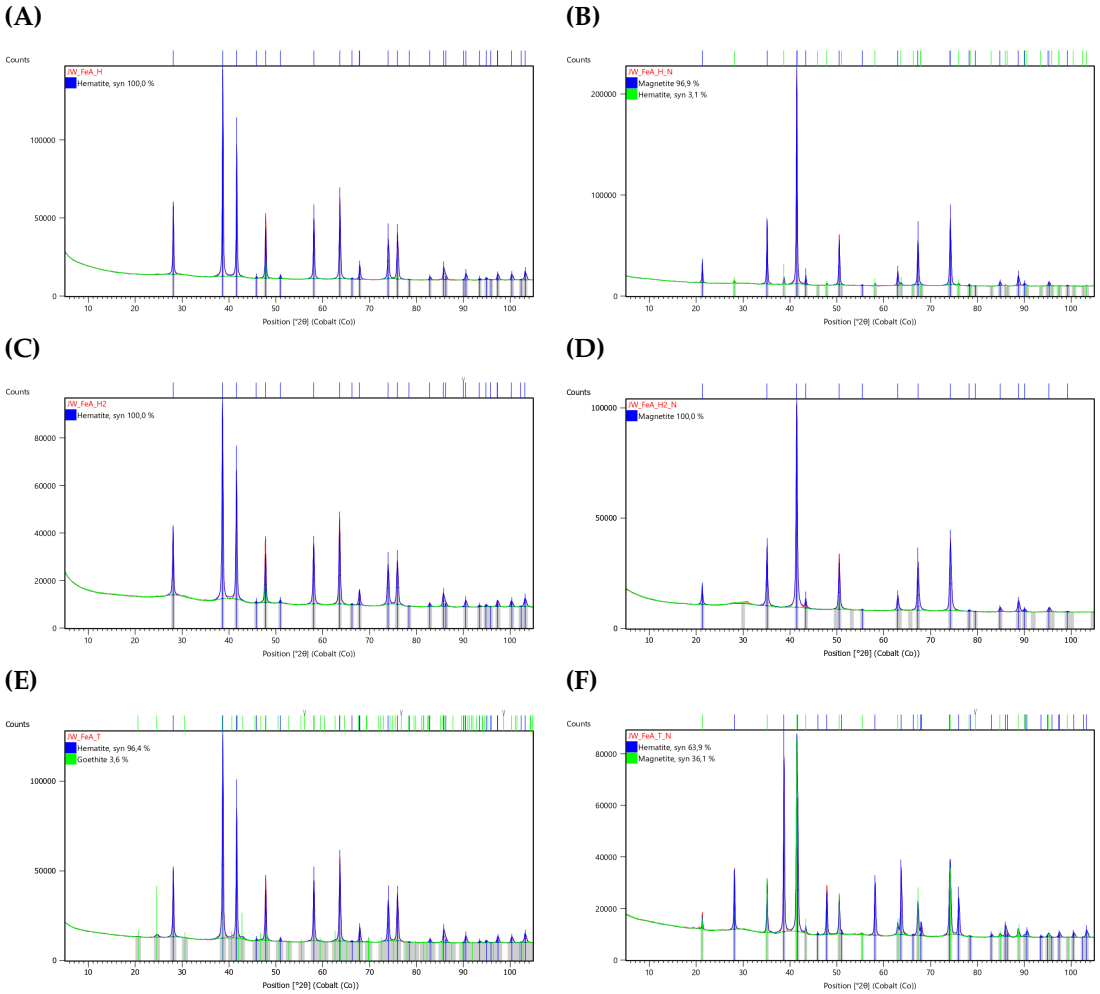

Figure B.2 | Rietveld analysis of XRD patterns of **(A)** JW_FeA_H, **(B)** JW_FeA_H_N, **(C)** JW_FeA_H2, **(D)** JW_FeA_H2_N, **(E)** JW_FeA_T, **(F)** JW_FeA_T_N.

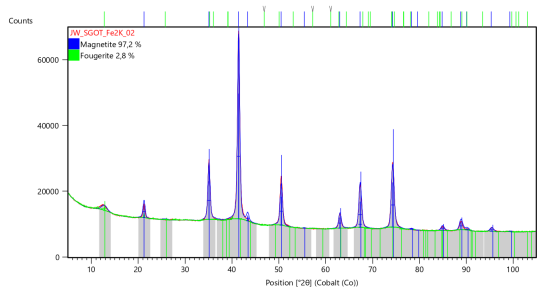

Figure B.3 | Rietveld analysis of XRD patterns of JW_SGO_T_Fe.

Appendix C – Unprocessed FT-IR spectra of GO-iron oxide compounds prepared by hydrothermal method

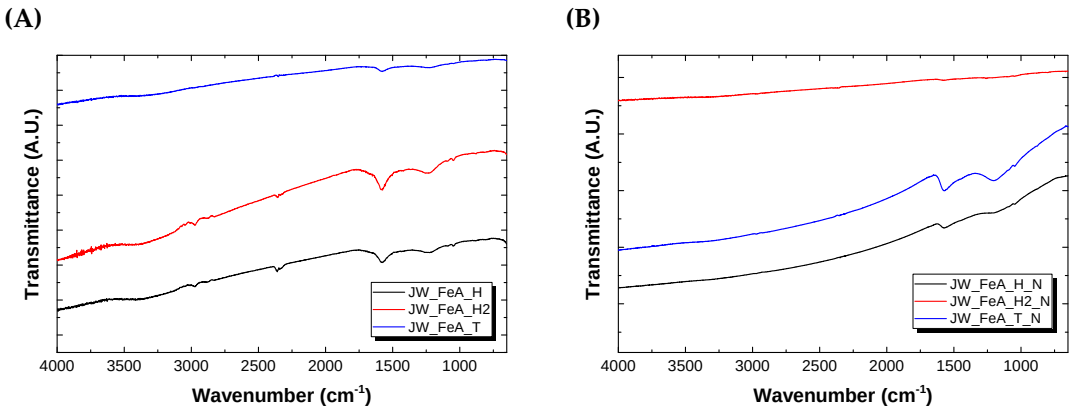

Figure C.1 Unprocessed FT-IR of GO-iron oxide compounds made by hydrothermal method: **(A)** samples before thermal treatment, **(B)** samples after thermal treatment.